6-2022

Identification and Characterization of Point Defects in Nonlinear Optical Crystals: Barium Gallium Selenide and Lithium Triborate

Brian C. Holloway

IDENTIFICATION AND CHARACTERIZATION OF POINT DEFECTS IN NONLINEAR OPTICAL CRYSTALS: BARUIM GALLIUM SELENIDE AND LITHIUM TRIBORATE

DISSERTATION

Brian C. Holloway, Lieutenant Colonel, USA

AFIT-ENP-DS-22-J-084

DEPARTMENT OF THE AIR FORCE
AIR UNIVERSITY

AIR FORCE INSTITUTE OF TECHNOLOGY

Wright-Patterson Air Force Base, Ohio

AFIT-ENP-DS-22-J-084

IDENTIFICATION AND CHARACTERIZATION OF POINT DEFECTS IN NONLINEAR OPTICAL CRYSTALS: BARIUM GALLIUM SELENIDE AND LITHIUM TRIBORATE

DISSERTATION

Presented to the Faculty

Graduate School of Engineering and Management

Air Force Institute of Technology

Air University

Air Education and Training Command

in Partial Fulfillment of the Requirements for the

Degree of Doctor of Philosophy in Nuclear Engineering

Brian C. Holloway, B.S., M.S.

Lieutenant Colonel, USA

16 June 2022

AFIT-ENP-DS-22-J-084

IDENTIFICATION AND CHARACTERIZATION OF POINT DEFECTS IN NONLINEAR OPTICAL CRYSTALS: BARIUM GALLIUM SELENIDE AND LITHIUM TRIBORATE

DISSERTATION

Brian C. Holloway, B.S., M.S.
Lieutenant Colonel, USA

Committee Membership:

Lt Col Christopher A. Lenyk, Ph.D.
Chair

Dr. Nancy C. Giles
Member

Dr. Benjamin F. Akers
Member

ADEDJI B. BADIRU, Ph.D.
Dean, Graduate School of Engineering and Management

AFIT-ENP-DS-22-J-084

Abstract

Increased interest in developing new nonlinear optical (NLO) materials has led to 3rd generation materials, such as barium gallium selenide ($BaGa_4Se_7$) and lithium triborate (LiB_3O_5). $BaGa_4Se_7$, or BGSe, is a recently developed nonlinear optical material used in the production of tunable mid-infrared laser beams via optical parametric oscillation. LiB_3O_5, or LBO, is a NLO material widely used to generate second, third, and fourth harmonics of high-power ultra-fast solid-state lasers in the ultraviolet region. Coherent solid-state based light sources capable of operating across this broad range of wavelengths are used in the development of new and enhanced technologies with commercial and defense-based applications such as: health and environmental monitoring devices, next-generation infrared countermeasures, and ballistic missile booster exhaust plume characterization.

There are only a few nonlinear crystals currently commercially available with the desired properties and capability of frequency conversion in this broad wavelength range. The performance of optical materials in high-powered military applications is largely limited by the presence of defects introduced during the growth process. These defects adversely affect performance through unwanted optical absorption, resulting in the buildup of excess heat, causing material deterioration or complete failure.

Unintentional point defects are present in $BaGa_4Se_7$ crystals and may adversely affect device performance. Electron paramagnetic resonance (EPR) and optical absorption are used to identify and characterize selenium vacancies, cation vacancies, and trace amounts of transition-metal ions present in $BaGa_4Se_7$ crystals. Five distinct EPR spectra, each representing an electron trapped at a selenium vacancy, are observed at low temperature (there are seven crystallographically inequivalent sele-

nium sites in the crystal). One spectrum is stable at room temperature and is present before illumination. The other four are produced at lower temperatures with 532 nm laser light and are thermally unstable at room temperature. Each $S = 1/2$ singly ionized selenium vacancy has a large, nearly isotropic, hyperfine interaction with ^{69}Ga and ^{71}Ga nuclei at one neighboring Ga site. A significant portion of the unpaired spin resides in a 4s orbital on this adjacent Ga ion and gives principal values of the hyperfine matrices in the 3350–6400 MHz range. Broad photoinduced optical absorption bands in the visible and near-infrared are assigned to the selenium vacancies.

Intrinsic point defects such as oxygen vacancies, lithium vacancies and self-trapped holes are present in as-grown LiB_3O_5 crystals. Electron paramagnetic resonance is used to identify and characterize (1) oxygen vacancies (V_O^+) that have trapped an electron on an adjacent boron ion, and (2) lithium vacancies (V_{Li}^0) that have trapped a hole on an adjacent oxygen ion. Self-trapped holes are also observed with EPR. EPR results show that some of the lithium vacancies are stabilized by an adjacent OH^- ion or a nearby Cu^{2+} ion. Transient absorption bands appear, along with thermal degradation of the nonlinear optical wave mixing efficiency, when these intrinsic defects trap "free" electrons and holes created by nonlinear processes (e.g., three- and four-photon absorption). These trapped electrons introduce an optical absorption band peaking near 300 nm and trapped holes produce bands in the 500-700 nm region.

Acknowledgements

I wish to thank my committee members: Lt Col Christopher Lenyk, Dr. Nancy Giles, and Dr. Benjamin Akers for the opportunity to work with and learn from you all. Each of you have challenged and encouraged me during this journey and I am forever grateful for your mentorship.

I owe a debt of gratitude to Dr. Larry Halliburton and Dr. Timothy Gustafson for their mentorship, guidance, and patience over these past few years. Not only have I learned to appreciate the detailed and methodical approach to conducting research, but I have gained an appreciation for the array of challenges faced by my civilian counterparts in the physical sciences field. It has been an honor and a pleasure working with you in lab. Thank you both so much.

Finally, to my family of lattice planes, thank you. This endeavor has taken much of me from you, and at times positioned me as an interstitial in our lattice. To my children, I am so proud of you! What you each have already achieved in life is no small polaron. You all are unbound and limitless. Keep hopping, and you will never become a self-trapped hole. Lastly, to my hyperfine wife, the $\langle bra|$ to my $|ket\rangle$, you complete my p-shell. With you, I can shine like neon. Your g-matrix has always been strictly diagonal. May our love remain s-like and isotropic as we navigate this world's magnetic field together. I love you all.

Brian C. Holloway

Table of Contents

Page

Page

List of Figures

List of Tables

IDENTIFICATION AND CHARACTERIZATION OF POINT DEFECTS IN NONLINEAR OPTICAL CRYSTALS: BARIUM GALLIUM SELENIDE AND LITHIUM TRIBORATE

1. Introduction

1.1 Motivation

There is a sustained interest in the development of continuously tune-able laser-based light sources, operating in the infrared spectral region, using nonlinear optical (NLO) crystals. The spectral upper limit of mature solid state lasers extends to about 3 µm [1]. The production of coherent light from solid state lasers in the mid-wave infrared region from 3 to 8 µm requires frequency down conversion using NLO crystals. NLO crystals are used in frequency conversion devices that convert the frequency of existing lasers into favorable frequencies [2]. Coherent light sources capable of operating across this broad range of wavelengths are used in health and environmental monitoring devices, next-generation infrared countermeasures, and ballistic missile booster exhaust plume characterization [3–6].

Of particular importance to the Department of Defense are materials suitable for employment in a wide range of nuclear-related missions. Active interrogation and monitoring of nuclear facilities from a distance and field-capable systems for determining biological changes after potential radiation exposure in an austere environment are two areas that continue to grow in importance. Systems designed around these mission sets must be capable of both producing a broad range of wavelengths from visible to long-wave infrared and detecting small shifts in wavelengths across this

spectrum. Additionally, the US military is interested in developing advanced techniques for manufacturing of radiation hardened microelectronics. Renewed threats of operating in a post-detonation nuclear environment and nuclear survivable systems have come into focus with the Russian invasion of Ukraine and threat of using small tactical nuclear weapons for achieving limited objectives. Mature materials capable of advancing and scaling the process of rapid microelectronics production and resistant to radiation or large power densities are a key enabling technology. The materials in this dissertation focus on the generation of wavelengths for all of the above nuclear applications.

Solid state tunable light sources make use of the nonlinear optical properties of crystals that allow energy exchange between independent optical fields and the crystal medium [7]. There are few NLO crystals currently available with the desired properties and capability of frequency conversion in the mid-infrared region. Some desired properties of NLO crystals are: high thermal conductivity, high laser damage threshold, high NLO coefficients, and a broad range of transparency [8]. The first two properties improve the efficiency of the energy exchange between the optical fields and the crystal medium. The latter two properties enable a broad tuning range of the laser output. In addition to these four crystal properties, the nonlinear crystal must be easy enough to manufacture to be commercially viable. $BaGa_4Se_7$ is unique among current NLO crystals being that its transparency range extends beyond 5 µm and can be used for longer wavelength mid-infrared applications [5].

Successfully identifying and characterizing isolated point defects allows crystal-growth companies to alter their growth process, thus eliminating unwanted defects and improving crystal performance. Defect identification is of interest to the AFRL/Materials and Manufacturing Directorate (AFRL/RX) as it can be correlated to damage-threshold studies of these materials. The $BaGa_4Se_7$ crystals studied in this

dissertation were provided by BAE Systems (Nashua, NH) [3]. The LiB_3O_5 crystals studied in this dissertation were grown by IPG Photonics.

1.2 Previous Research on $BaGa_4Se_7$

Barium gallium selenide, $BaGa_4Se_7$, is a member of a fairly new class of barium chalcogenides which was first grown in China and Russia. This new class of chalcogenides has demonstrated potential in the development of tunable lasers operating across the mid-wave infrared (MWIR) and long-wave infrared (LWIR) [9]. Two other well known and commercially available NLO crystals are zinc germanium phosphide $ZnGeP_2$ and silver gallium selenide $AgGaSe_2$ [9, 10]. $ZnGeP_2$ has both high NLO coefficients, and a high laser damage threshold, but suffers from two-photon absorption at 1 µm, a common pump wavelength [9, 11]. $AgGaSe_2$ has a low laser damage threshold, which limits the power of an input optical field for frequency conversion, and is prone to thermal lensing [12]. These factors preclude the use of $AgGaSe_2$ in high frequency and high power applications. Compared to $AgGaSe_2$, $BaGa_4Se_7$ has a 2-3 times improvement in second harmonic generation (SHG) and 3.7 times the laser damage threshold [11]. $BaGa_4Se_7$, a monoclinic crystal with space group Pc, is unique in that it possesses the three desired NLO characteristics across the full IR region simultaneously. Shown in figure 1.1, $BaGa_4Se_7$ has a wide range of transparency 465 nm - 17 µm, a NLO coefficient of 24.3 pm/V, and a damage threshold of 557 MW/cm^2 when pumped at 1 µm with a 5 ns pulse width [14]. The sharp dip in the transmission near 15 µm in figure 1.1 is caused by vibrational excitations of the crystal lattice called phonon modes [15]. This phonon mode absorption limits the available tuning range for NLO crystals. This same phonon mode absorption occurs at 12 µm in $AgGaSe_2$ and $ZnGeP_2$ crystals [16, 17]. One of the primary interests in this new class of chalcogenides, and $BaGa_4Se_7$ in particular, is the ability

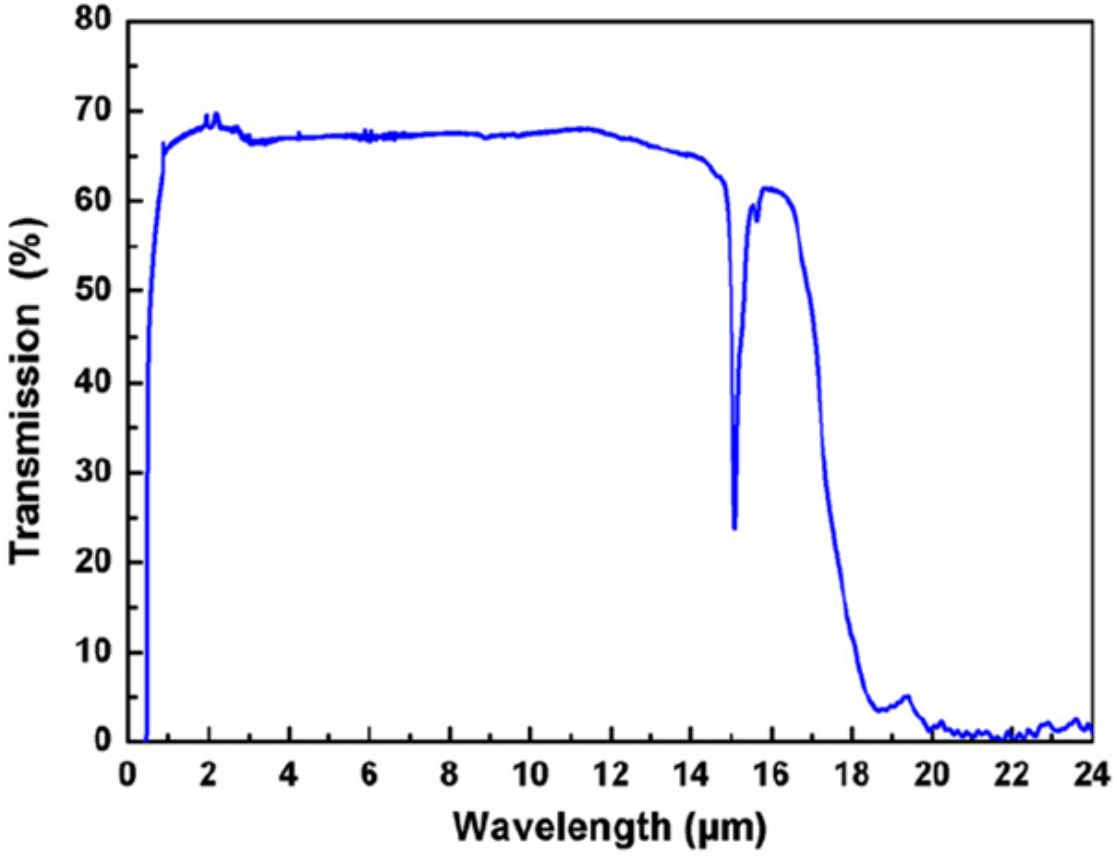

Figure 1.1. Optical transmission of $BaGa_4Se_7$ for a sample of 2 mm thickness. Reprinted with permission from [13].

to bridge the 6 - 8 micron gap that many other materials with lighter constituents, such as $ZnGeP_2$ and $AgGaSe_2$, cannot. When coupled with the ease and simplicity of growth, $BaGa_4Se_7$ has the potential to become the ubiquitous OPO in many commercial, military, or other high-power applications.

Most of the research on $BaGa_4Se_7$ conducted to date has focused on the determining the nonlinear coefficients for the material and damage thresholds for the crystal under various pump conditions. Zhang *et al.* determined the two largest nonlinear tensor elements of $BaGa_4Se_7$ to be 24.3 and 20.4 pm/V [11]. In 2020, Degang *et al.* demonstrated a high-energy, tunable, long-wave mid-infrared optical parametric oscillator based on the $BaGa_4Se_7$ crystal using a 1 µm pump laser [18]. Optical para-

metric oscillation is a second-order nonlinear optical process involving the mixing of two different optical waves to produce a third, and is reviewed in Appendix A. No research has been performed on the fundamental intrinsic defects for BGSe such as cation or anion vacancies and anti-sites. Additionally, while differences in crystal coloration have been observed under different growth conditions, there has been no reporting on the role of defects in optical absorption that is critical for understanding and improving performance in high-power applications [14].

1.3 Previous Research on LiB_3O_5

Lithium triborate, LiB_3O_5, is an orthorhomic crystal with space group $Pna2_1$, a well-established nonlinear optical crystal, and first grown in 1989. It is widely used in a variety of harmonic generation and optical parametric oscillator applications in the ultraviolet, visible, and near infrared [19, 20]. In addition to a large band gap of 7.75 eV and a broad transmission range from 155 nm to 3.2 µm, LiB_3O_5 has a high laser damage threshold (25 GW/cm^2 when pumped at 1 µm with a 0.1 ns pulse width), and a moderate nonlinear coefficient [19, 21]. LiB_3O_5 is commonly employed in second harmonic generation (SHG) devices with a high pulse power Nd:YAG (neodymium-doped yttrium aluminum garnet; Nd:$Y_3Al_5O_12$) laser on input. Other common NLO crystals used in SHG are: potassium dihydrogen phosphate (KDP), β-barium metaborate (BBO) and potassium titanyl phosphate (KTP). In high pulse power applications, LiB_3O_5 bests the other NLO crystals mentioned in terms of having a higher laser damage threshold and frequency conversion efficiency [21]. In comparison with KTP and BBO, LiB_3O_5 has a smaller birefringence which limits the range in which two different optical waves can be phased matched [21, 22]. As in other NLO materials, isolated point defects in LiB_3O_5 crystals degrade the performance causing absorption bands that extend from 200 nm to above 400 nm,

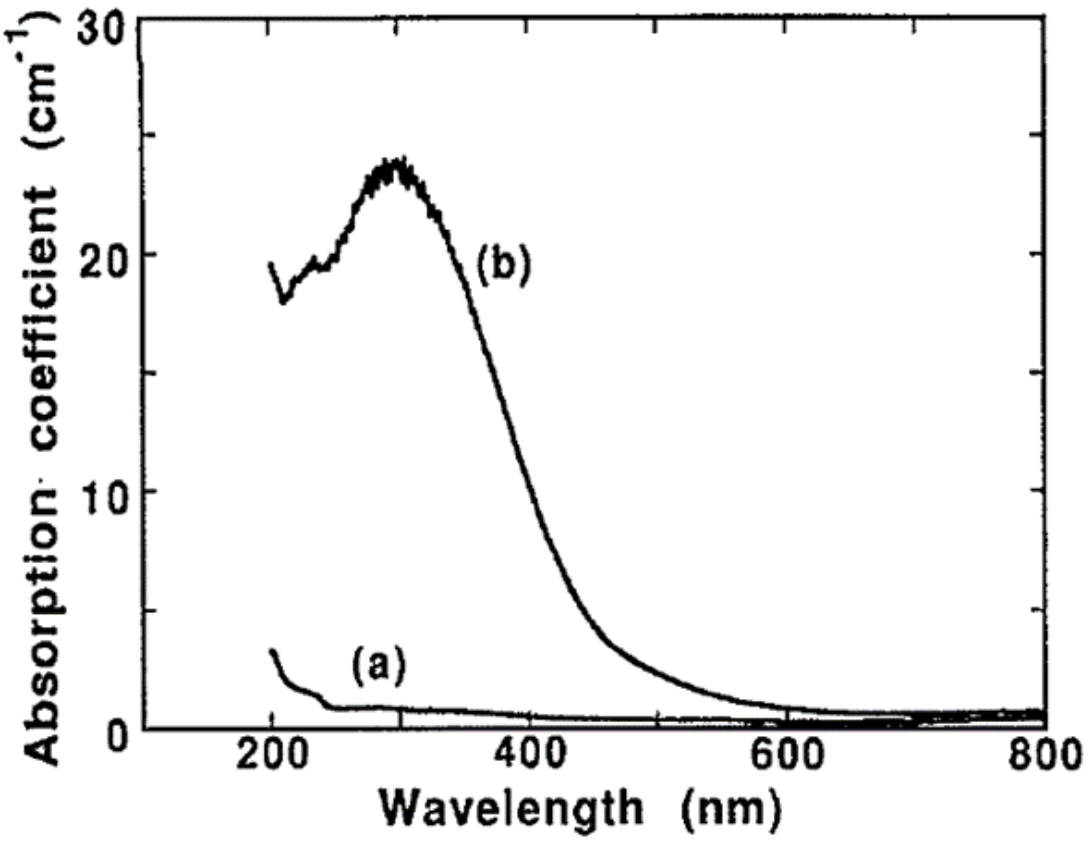

Figure 1.2. Optical absorption spectrum of LiB_3O_5 taken before (a) and after (b) irradiation with x rays at 90 K. Measurement and irradiation were performed at the same temperature. Reprinted with permission from [23] with the permission of AIP Publishing.

as shown in figure 1.2. Early work by Scripsick *et al.* identified trapped electron and hole centers and provided a tentative assignment of an intrinsic defect to the trapped hole center [23]. His work also observed that low temperature irradiation with x rays at 77 K produced a broad optical absorption band that was unstable at room temperature [23]. Hong *et al.* confirmed the observations of Scripsick, shown in figure 1.3, in addition to uncovering a second trapped hole. Hong's findings indicated that the first hole center, center A, was unstable around 130 K and assigned it to the intrinsic defect, a self-trapped hole. The second hole center, not shown in figure 1.3, was determined to be thermally unstable between 150 -200 K and tentatively assigned

to a trapped hole near a lithium vacancy. Shown in figure 1.3, the electron-like

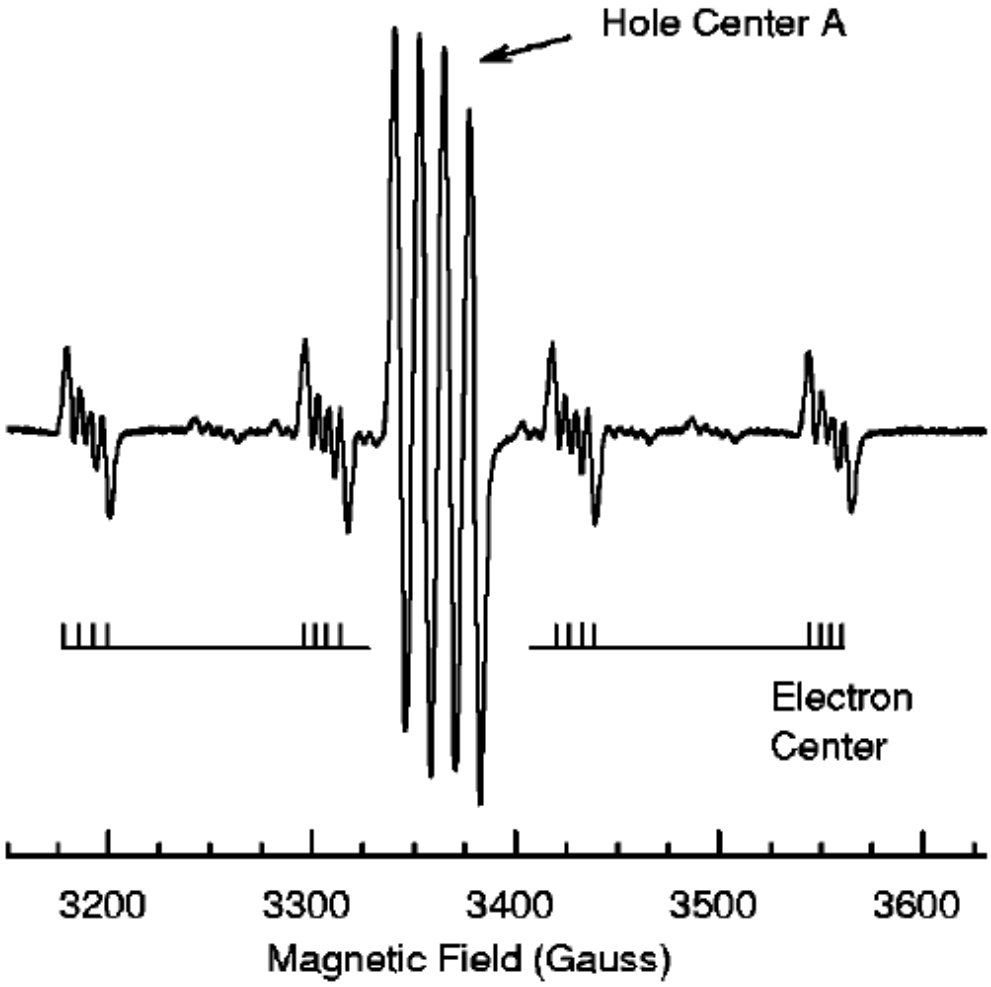

Figure 1.3. EPR spectrum showing hole center A (in the central portion of the scan) and the electron-like center (with the larger 4-line splitting). The data were taken at 60 K with the magnetic field parallel to the (010) direction of the crystal. Reprinted with permission from [20] with the permission of APS Publishing.

center reported by Scripsick and Hong has also been observed by Ogorodnikov *et al.* after illumination under similar conditions; however, differences have arisen in defect assignment [24]. In the initial reporting, Scripsick *et al.* did not provide a defect assignment to the electron center due to an incomplete set of angular dependence data based on the experimental limitations presented by the EPR cavity dimensions and physical sample size [23]. Based on a wider study involving experiment and

calculations, Hong *et al.* provided a tentative assignment of an oxygen vacancy to the defect. Ogorodnikov *et al.* disputed the assignment based on his data and assigned the defect to an electron trapped at an interstitial boron [24]. In each of these three cases, the defect assignment has been based on subsets of available LiB_3O_5 data and leaves open the question of definitive assignment. Determining the assignment of the defect is necessary to improve LiB_3O_5 crystal growth and performance through reducing the incorporation of defects responsible for unwanted optical absorption.

1.4 Point Defects, Identification and Characterization

The electrical and optical properties of solids are largely governed by the presence of defects that perturb the regular ordered array of ions within the crystal lattice. Point defects are localized disturbances within the lattice. The most common roles played by point defects in crystals are electron traps, hole traps, and recombination centers. A trap is a defect that captures an electron (electron trap) or a hole (hole trap), and has a low ionization energy such that the electron (or hole) is released from the trap with little energy. These are often termed "shallow traps" as their energy levels lie close to the conduction or valance bands of the crystal. Recombination centers are similar to traps, however their ionization energies are greater, and the probability of thermal release of the electron (or hole) is much less than the probability of recombination [25]. This release of energy can be radiative through the generation of photons, non-radiative through the release of phonons, or a combination of the two. An optically active defect is a defect that can be photoexcited from the defect to a band (conduction or valence band), from a band to the defect, or between the ground state and excited states of the defect (which is called intra-center absorption). Isolated point defects may serve as sources of unwanted optical absorption and adversely affect a crystal's performance, resulting in decreased device

performance, premature deterioration, or complete failure under intense illumination such as Q-switching applications.

Electron paramagnetic resonance (EPR) is a high sensitivity and high resolution technique used to identify and characterize point defects and impurities in materials that have unpaired spins. The EPR spectrum represents the absorption of microwaves by the paramagnetic spin system and allows for an energy-level model of the spin system and concentrations of defects as low as a few parts per billion to be determined [26].

1.5 Organization of the Dissertation

Chapters 2 and 3 provide an overview of the experimental principles and instrument setup respectively. The fundamentals and electron paramagnetic resonance and optical absorption and their application in identifying and characterizing point defects in single crystals is detailed. Each instrument used in the collection of experimental data and its operation is described in chapter 3.

Chapters 4 and 6 are prepared as publishable work according to the standards of the Journal of Applied Physics in accordance with the style guide for AFIT dissertations, thesis, and graduate research papers. Chapter 4 has already been published in the Journal of Applied Physics. Chapter 4 is the first published work identifying and characterizing intrinsic cation vacancies in $BaGa_4Se_7$, their paramagnetic charge state, method of production, and optical absorption characteristics and reproduced with the permission of AIP Publishing [27]. Chapter 5 is a short extension to Chapter 4 correlating optical absorption spectra to EPR identified defects in $BaGa_4Se_7$. Chapter 6 is written for future publication in the Journal of Applied Physics and proposes a new model for a defect previously characterized as a boron interstitial [28]. The new model proposes that the defect is not a boron interstitial, but indeed an

oxygen vacancy with the unpaired spin localized at a nearby boron atom. Supporting evidence is given to support this new proposed model.

The written document concludes with a summary of research results and suggestions on future experiments for $BaGa_4Se_7$ and LiB_3O_5. The results and the materials investigated are discussed in the broader context of several emerging materials for laser applications at wavelengths greater than 6 microns.

2. Background

This chapter explains the physics principles of EPR and ultra-violet/visible (UV-Vis) spectroscopy, applicable to the identification and characterization of point defects in $BaGa_4Se_7$ and LiB_3O_5. Combined, these methods are used to describe the: paramagnetic ground state, local environment of the defect, its charge state, and the relative concentrations of the defect. A general overview of point defects is presented first to provide context to the physics principles that follow.

2.1 Defect Classification

All crystals have imperfections where the regular array of atoms is disrupted by an irregularity or an impurity. Point defects are broadly classified as native (intrinsic) defects or defects due to an impurity (extrinsic). A native defect consists of host atoms that are present or absent in the native crystal. Impurity defects are composed of impurity atoms foreign to the perfect crystal. The most important point defects investigated in this dissertation are vacancies, interstitial ions, and impurities. A vacancy is a missing atom in the regular array. An interstitial is an atom present, but not at a regular lattice site. An impurity atom can reside on various sites.

A vacancy is denoted V_A where A is a host atom. For example, in $BaGa_4Se_7$, a missing selenium atom is denoted V_{Se}. An interstitial is denoted A_i, again where A is a host atom. For example, a boron interstitial in LiB_3O_5 is denoted B_i. An example of an impurity is a copper atom in LiB_3O_5 that substitutes for a lithium atom and is denoted Cu_{Li}.

The charge state of the defect, with respect to the host atom, is written as a superscript. For example, V_{Se}^{+} means that the selenium vacancy is positively charged (i.e. has one less electron) compared to the charge neutral $BaGa_4Se_7$ crystal where the

selenium ions are in the 2^- state, having acquired two valence electrons to complete its outer p-shell.

In addition to these properties of site location and relative charge state, point defects are also classified by their symmetry. A point defect has symmetry operations such as rotations, reflections, and inversions that leave at least one point fixed. It is through the use of symmetry operations that we are able to present models of point defects that account for the systematic recurrence of a specific defect throughout the bulk crystal.

2.2 Physics Background

The array of physics phenomena, expressions, and equations found in this dissertation can be understood in the overarching contexts of conservation of energy (COE), conservation of momentum (COM), and symmetry operations. This study of defects in NLO materials spans a vast array of discrete physics subjects such as: quantum mechanics, electricity and magnetism in matter, group theory, and linear algebra. This section provides a brief overview of some of the physics principles employed in this study. To facilitate an ease of understanding it is emphasized that each of the discrete physics principles, expressions, and equations are directly related to the three overarching concepts of COE, COM, and symmetry. Specifically, Poynting's theorem, non-linear three-wave mixing, Bloch's theorem and its relationship to the Schrödinger's equation, and the spin Hamiltonian concepts are each briefly discussed and are direct consequences of the conservation of energy. The birefringent property of crystals, the associated phase matching condition employed in frequency conversion devices, and the electron-phonon interaction in optical absorption are all direct consequences of applying the law of conservation of momentum (crystal momentum to be exact). Lastly, when discussing the nonlinear optical coefficients of $BaGa_4Se_7$

and LiB_3O_5 crystals, and the characterization of the point defects therein, symmetry operations are employed to greatly simplify calculations and enable a model of the crystal defect to be developed.

2.2.1 Nonlinear Optical Effects (Three-wave Mixing)

To motivate the study of point defects in $BaGa_4Se_7$ and LiB_3O_5 crystals, this section briefly describes the exchange of energy between electromagnetic radiation and non-linear optical (NLO) crystals, and how the presence of point defects within NLO crystals can adversely affect the desired generation of tunable light in processes such as optical parametric amplification (OPA). The interaction of light with matter can be modeled as a driven oscillator where the light (electromagnetic waves) serves as the energy source and the atomic system of electrons and ion cores represent the oscillating bodies. Generally, the ion cores are treated as fixed within the lattice and the electron probability distribution as an oscillating "electron cloud". It is the electric field portion of the electromagnetic wave that serves as the driving force, oscillating the charged bodies in the material. At low light intensities the response of the electron cloud is linear. At high intensities the oscillations are driven into a nonlinear response. $BaGa_4Se_7$ and LiB_3O_5 crystals are used in frequency conversion devices for high powered lasers and thus the nonlinear optical effects in the crystal become dominant. The most common three-wave mixing nonlinear processes are harmonic generation, sum and difference frequency generation, and optical parametric oscillation. Sum frequency generation (SFG) and second harmonic generation (SHG) involve two input photons that are annihilated in the creation of one photon with higher energy [7]. Difference frequency generation is the reverse of SFG where a high energy photon (pump) is mixed with a lower energy photon (signal) that generate a new photon at the same energy as the original signal photon, and a new photon

(idler) at energy lower than both the pump and signal photons [7]. These processes require both conservation of energy and conservation of momentum, as the efficiency of the conversion is dependent upon phase matching of the three optical waves.

Down conversion, via difference frequency generation (DFG), can be used to amplify a weak beam by parametric amplification. In this process there are two waves at the input, a strong pump (ω_1) and a weak signal (ω_2). There are three waves at the output consisting of two signal photons (ω_2), and one photon at the difference frequency called the idler (ω_3) whereby conservation of energy $\omega_3 = \omega_1 - \omega_2$. The ω_1 photon is annihilated in the production of the ω_2 and ω_3 photons, while the incident ω_2 is unaffected. The newly generated idler photons can be used to generate more signal photons by mixing with the pump field ($\omega_1 - \omega_3 = \omega_2$).

Kato *et al.* demonstrated both SHG and SFG with $BaGa_4Se_7$ [29]. Boursier *et al.* demonstrated both SHG and DFG with $BaGa_4Se_7$ [30]. LiB_3O_5 has been used in SHG of a Nd:YAP pumped at a wavelength of 1.079 µm [21]. Lin Shujie *et al.* have detailed the phase matching and effective SHG coefficients of LiB_3O_5, detailed in reference [21].

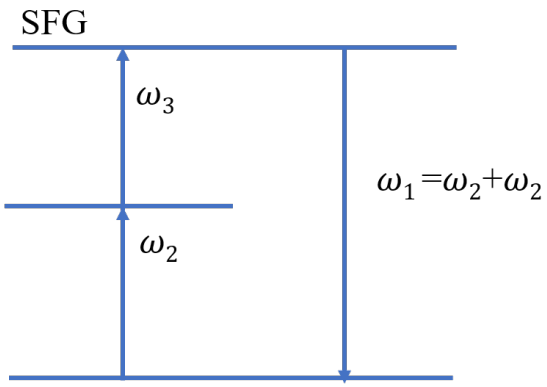

Figure 2.1. Diagram of the three-wave interaction for Sum Frequency Generation (SFG). Two waves of frequency ω_2 and ω_3 are mixed at input and through the sum frequency generation process a wave of frequency ω_1 is produced at the output.

This process results in an amplification of the signal field (ω_2) and is referred to

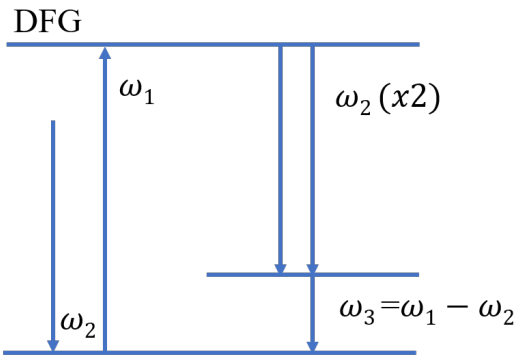

Figure 2.2. Diagram of the three-wave interaction for Difference Frequency Generation (DFG). Two waves of frequency ω_2 and ω_1 are mixed at input and through the difference frequency generation process a wave at frequency ω_3 and two waves at frequency ω_2 are produced at the output. Since two waves at frequency ω_2 are generated at the output this is also an optical parametric amplification (OPA) of the ω_2 wave.

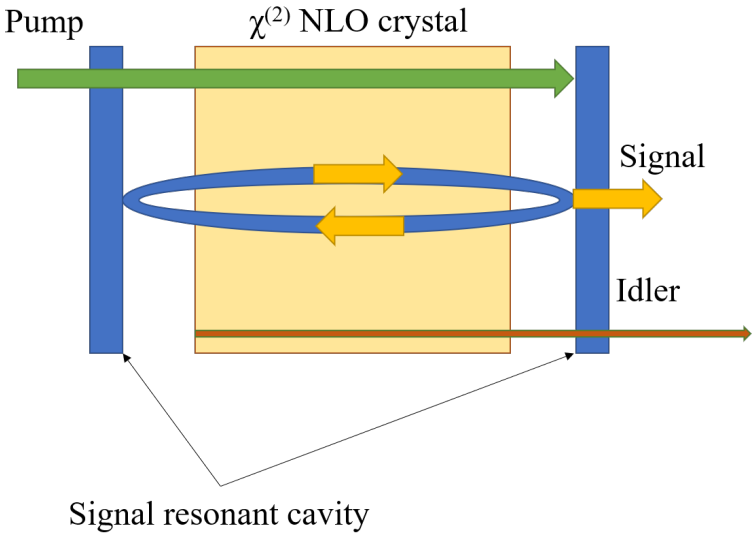

Figure 2.3. Diagram of a singly resonant Optical Parametric Oscillator (OPO). The green, yellow, and brown arrows represent the pump (ω_1), signal (ω_2), and idler (ω_3) waves respectively. This processes is very similar to that of DFG where parametric amplification of the ω_2 wave is generated. The only difference between that optical parametric amplification (OPA) process and optical this parametric oscillation (OPO) process is that the OPA device is placed in a resonant cavity that is tuned to one of the input frequencies (either ω_1 or ω_2) as shown in figure 2.2.

as optical parametric amplification (OPA); in this case, amplification of the signal field (ω_2). With such single pass devices, the only way to increase the intensity of the output is to increase the input power or narrow the spot size [7].

A way to achieve an exponential increase in the output intensity is to place the OPA device inside a resonant cavity, tuned to the frequency of one of the input waves (pump or signal), such that standing waves, or modes, are generated inside the cavity. The nonlinear conversion efficiency increases as the intensity of the standing waves inside the cavity increases. These standing waves are oscillations and this combination of an OPA inside a resonant cavity is so termed an optical parametric oscillator (OPO).

All the processes described are all dependent upon efficient propagation of light through the medium at the relevant frequencies. If losses are kept low enough, a cavity tuned to resonance with the ω_2 (signal) generates a self-sustaining oscillation where only the input ω_1 (pump) is required. With most second-order nonlinear processes, $\chi^{(2)}$, it is assumed that the photon energies ($\hbar\omega_i$) are not resonant with any real electronic states of the material, and that the excited states are transient [7]. If a defect has an electronic state that is resonant with one of the photon energies, then it can serve as an absorption source, and thus degrade the efficiency of the nonlinear $\chi^{(2)}$ processes. Losses in the gain medium can occur from absorption and/ or scattering. This can result in joule-heating of the medium and degrade the laser efficiency causing the oscillations to dampen. Local heating also disrupts the necessary population inversion needed to sustain stimulated emission. Thermal lensing causes changes in the index of refraction which alters the phase velocity of the traveling waves and thus degrades the phase matching condition.

2.2.2 Electron Paramagnetic Resonance (EPR)

An optically active point defect is a localized lattice imperfection (native to the host crystal or an impurity atom) where the electronic states are energetically coupled to the vibrational modes of the crystal [31]. Paramagnetic defects are systems with at

least one unpaired electron and thus, possess a total angular momentum and magnetic moment greater than zero. The electron is a fermion, which means it has half-integer spin (a quantum property with no classical analogue) and obeys the Pauli exclusion principle. It is a fundamental particle that possesses charge, orbital and intrinsic angular momenta, and thus a magnetic moment. The relationship between the total angular momentum and the magnetic dipole moment of an electron is detailed in section 2.2.2.1.

2.2.2.1 Classical Magnetic Moment

The calculation of the magnetic moment μ, of a particle with mass m, charge q, and current i, undergoing uniform circular motion defined by an area A and radius r, lying in the xy plane, and its relation to its orbital angular momentum, l, that points in the z direction is instructive mathematically. The magnetic moment of the circularly rotating charge is

$$\mu_z = iA = \pm\frac{qv\pi r^2}{2\pi r} = \pm\frac{q}{2m}mvr = \frac{q}{2m}l_z \tag{2.1}$$

where for time t, and velocity v

$$\frac{1}{t} = \frac{v}{2\pi r}$$

and the sign choice depends on the direction of rotation. The ratio of the magnetic moment and angular momentum is called the gyromagnetic ratio γ.

$$\gamma = \frac{\mu}{l_z} = \frac{q}{2m}$$

2.2.2.2 Quantum Magnetic Moment

Quantum mechanically, angular momentum is an operator, $\hat{\mathbf{J}}$, with an associated quantum number M_j. $\hat{\mathbf{J}}$ represents a generalized angular momentum operator which could be for example: orbital angular momentum operator ($\hat{\mathbf{L}}$), electron intrinsic spin angular momentum operator ($\hat{\mathbf{S}}$), nuclear spin operator ($\hat{\mathbf{I}}$), or a vector sum of any of them [32, 33]. In addition to orbital angular momentum fermions possess an intrinsic quantized property called "spin", that behaves mathematically like $\hat{\mathbf{L}}$, but has no classical analogue. The eigenvalue equations for angular momentum operators that commute with the Hamiltonian are

$$\hat{J}_z \left|\psi\right\rangle = \hbar M_J \left|\psi\right\rangle \tag{2.2}$$

$$\hat{\mathbf{J}}^2 \left|\psi\right\rangle = \hbar^2 J(J+1) \left|\psi\right\rangle \tag{2.3}$$

where the magnetic quantum number, M_J, spans from $+J$ to $-J$ in integer increments. For example if $S{=}\frac{3}{2}$, then the subspace M_s spans $(\frac{3}{2}, \frac{1}{2}, -\frac{1}{2}, -\frac{3}{2})$. There are $2S+1$ eigenvalues for a given S. The $S{=}\frac{1}{2}$ state is commonly called a "doublet" state as there are two corresponding eigenvalues; $S = 1$ state a "triplet" state and so on. The $2S + 1$ electron states define the ground state of the free electron in a magnetic field with the energy level determined by the projection M_s eigenvalue. Thus in terms of spin

$$\mu_z = \gamma \hat{S} = \gamma M_s \hbar \tag{2.4}$$

where

$$\gamma = \frac{gq}{2m} \tag{2.5}$$

and the Zeeman correction factor g is included. This correction factor is required for all cases other than those involving pure angular momentum. For the free electron case $g_e = 2.00232$ and q in (2.5) is negative and thus

$$\mu_z = \gamma_e M_s \hbar = -g_e \beta_e M_s \tag{2.6}$$

where

$$\beta_e = \frac{|q|\hbar}{2m} = \left|\frac{\gamma\hbar}{g_e}\right| \tag{2.7}$$

is the called electron Bohr magneton. Equation (2.7) states that each quantum of angular momentum, $\hbar$, is associated with a magnetic moment β_e. When the electron is acted on by additional external fields it is no longer free, and g_e in equation (2.7) must be generalized with g-values that reflect the local symmetry of the system and its spatial orientation with respect to the externally applied field. In practice the generalized g-values take the form of a symmetric 3×3 matrix.

The potential energy of a magnetic dipole moment in the presence of a magnetic field is given by

$$U = -\vec{\mu} \cdot \vec{B} \tag{2.8}$$

where $\vec{B}$ is the magnetic field. In terms of the scalar product equation, (2.8) can be expressed in terms of the product of a row vector -$\langle\mu|$ and a column vector $|B\rangle$

$$U = -\mu^T \cdot \mathbf{B} \tag{2.9}$$

$$= -\mathbf{B}^T \cdot \mu \tag{2.10}$$

which shows that energy is maximized (minimized) when the magnetic field points in the opposite (same) direction as the magnetic moment.

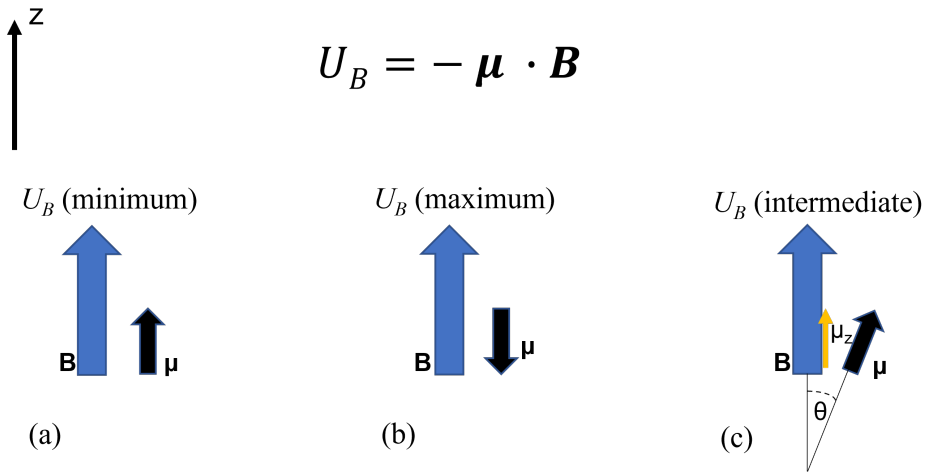

Figure 2.4. Diagram of three possible orientations of a magnetic moment in an external magnetic field directed along the z axis. At (a) the magnetic moment is aligned with the magnetic field which yields a minimum in magnetic potential energy. At (b) the magnetic moment is anti-aligned with the external magnetic field and yields a maximum in magnetic potential energy. At (c) the magnetic moment is randomly oriented with respect to the external magnetic field and it is the projection of the magnetic moment vector along the z axis (shown in yellow) that is proportional to the magnetic potential energy.

When B is chosen to be along the z direction, and in the same direction as μ_z, then equation (2.8) reduces to

$$U = -\mu_z B_z \tag{2.11}$$

Substituting equation (2.6) into equation (2.11) yields

$$U = g_e \beta_e B_z M_s \tag{2.12}$$

Expressing equation (2.9) in operator form yields the electron Zeeman spin energy term

$$\hat{H}_{EZ} = -\mathbf{B}^T \cdot \hat{\mu} \tag{2.13}$$

$$= g_e \beta_e \mathbf{B}^T \cdot \hat{\mathbf{S}} \tag{2.14}$$

Equation (2.12) describes how the application of an external magnetic field causes

a splitting of the energy levels, each labeled by the eigenvalues of the spin operator. EPR is the process by which an external oscillating magnetic field drives a transition between energy levels (or states) of the electron. The resonance condition is achieved in either of two ways: hold the magnetic field B constant and vary the frequency ν, or hold ν constant and vary B [34]. Most spectrometers achieve the resonance condition in the latter way and are discussed in more detail in Chapter 3. The equation below can be solved for either the frequency ν or the magnetic field B depending upon which quantity (ν or B) is varied.

$$h\nu = \Delta U = [\frac{1}{2} g_e \beta_e B_z] - [-\frac{1}{2} g_e \beta_e B_z] = g_e \beta_e B_z \tag{2.15}$$

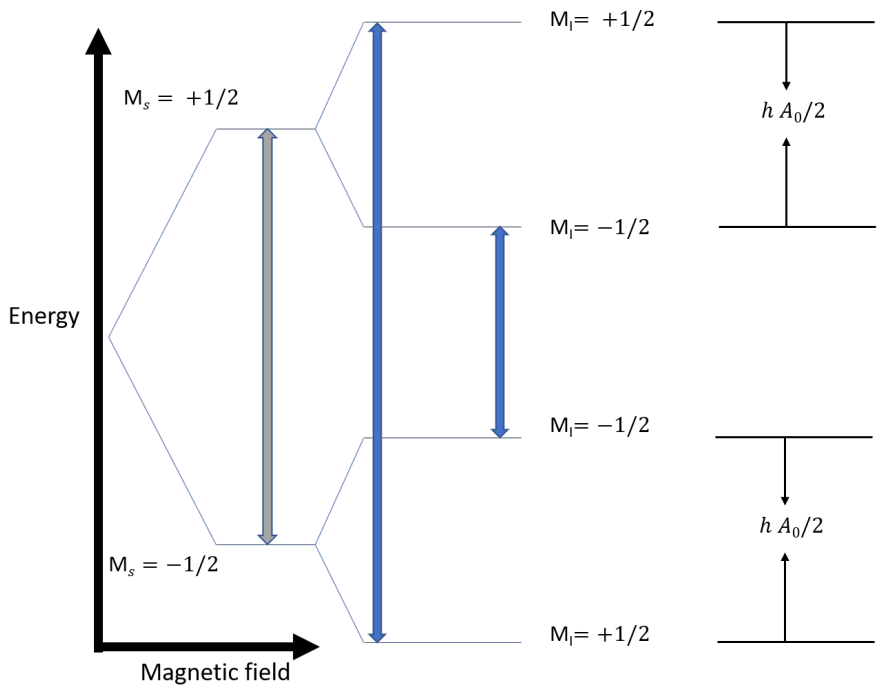

Figure 2.5. Energy levels of the hydrogen atom at constant magnetic field. Here the grey arrow represents the transition corresponding to the free electron. The two blue arrows correspond to the allowed transitions with hyperfine coupling. Reproduced after [32].

The analysis presented in this section is applicable to a "free" electron in an

externally applied magnetic field. The spin Hamiltonian which describes the energy of the ground state of a paramagnetic center in the context of the surrounding crystal lattice is explained in the next subsection.

2.2.2.3 The Spin Hamiltonian

The spin Hamiltonian is an energy balance equation represented as a sum of five terms, two of which are dependent of the applied magnetic field and three which are not. The spin Hamiltonian describes the behavior of the ground state of the spin system. Here the energy levels of the ground state subspace depend on the angle between the crystalline axis and the magnetic field [33].

$$\hat{H}_{spin} = \hat{H}_{EZ} + \hat{H}_{NZ} + \hat{H}_{HF} + \hat{H}_{ZF} + \hat{H}_{NQ} \tag{2.16}$$

The five terms of the spin Hamiltonian (2.16) correspond to the following energy interactions: electron Zeeman, nuclear Zeeman, hyperfine coupling, fine structure coupling, and nuclear quadrupole coupling. The first two terms are field dependent and the last three are not. An overview of these terms is given below and will be explained in that order.

2.2.2.4 Field Dependent Terms

Within a crystal, the magnetic field at the paramagnetic center may consist of both the externally applied magnetic field and local magnetic fields. The fields add as vectors to produce an effective magnetic field $\mathbf{B}_{eff} = \mathbf{B}_{ext} + \mathbf{B}_{local}$. There are two sources of the local field: those that are induced by the external field and thus have a magnitude that is dependent on $\mathbf{B}_{ext}$, and those that are permanent and independent of $\mathbf{B}_{ext}$ except in their orientation [32]. Contributions of the first type are due to the orbital motion of the unpaired spin and the local field can be expressed as a function

of the externally applied field such that $\mathbf{B}_{local} = -\sigma\mathbf{B}_{ext}$, where σ is a tensor-like quantity that depends on the relative orientation of the spin center with respect to the applied external magnetic field and the minus sign due to application of Lenz' law.

$$\mathbf{B}_{eff} = \mathbf{B}_{ext} + \mathbf{B}_{local} \tag{2.17}$$

$$\mathbf{B}_{eff} = \mathbf{B}_{ext} - \sigma\mathbf{B}_{ext} \tag{2.18}$$

$$\mathbf{B}_{eff} = (1 - \sigma)\mathbf{B}_{ext} \tag{2.19}$$

$$\mathbf{g} = g_e(1 - \sigma) \tag{2.20}$$

To account for this field orientation dependent spin-orbit coupling the free spin value g_e from (2.15) is replaced with a 3×3 matrix, $\mathbf{g}$. This yields

$$\hat{H}_{EZ} = \beta_e \mathbf{B}^T \cdot \mathbf{g} \cdot \hat{\mathbf{S}} \tag{2.21}$$

where

$$\mathbf{g} = \begin{bmatrix} g_{xx} & g_{xy} & g_{xz} \\ g_{yx} & g_{yy} & g_{yz} \\ g_{zx} & g_{zy} & g_{zz} \end{bmatrix}, \tag{2.22}$$

$\mathbf{B}^T$ is a row vector, and $\hat{\mathbf{S}}$ is a column vector of spin operators. Contributions to the local field of the second type, permanent and independent of $\mathbf{B}_{ext}$, will be addressed in the field independent subsection. Quantum mechanically, the square of the momentum operator is the quantity that is measured, as shown in equation (2.3). Analogously, the g-tensor that is measured is $\mathbf{g}\mathbf{g}^T$. Typically the $\mathbf{g}$ matrix is reported in literature. A complete treatment is given by Weil and Bolton [32]. An isotropic $\mathbf{g}$ matrix will have one entry repeated along the diagonal of the matrix.

For an anisotropic spin system the value of $\mathbf{g}$ varies with orientation of the crystal relative to the applied magnetic field $\mathbf{B}$. The matrix element g_{xy} can be interpreted as the contribution to $\mathbf{g}$ along the x-axis when the magnetic field is along the y-axis. Off-diagonal elements of the $\mathbf{g}$ matrix reflect the anisotropy of the external magnetic field interaction with the paramagnetic center, due to spin-orbit coupling. In the literature the $\mathbf{g}$ matrix is usually presented in its principle axis system where the off-diagonal elements vanish. Experimentally this is achieved through a coordinate transformation by applying successive rotation matrices to rotate coordinates from the lab frame (x, y, z) to the crystal frame (a, b, c), then from the crystal frame (a, b, c) to the principle axes of the defect frame (x', y', z'). The full derivation of equation (2.21) involves second order (or higher) corrections to the energy eigenvalues and is detailed in chapter 4.8 and appendix A.6 of [32].

The nuclear Zeeman term ($\hat{H}_{NZ}$), is due to the interaction between magnetic moment of magnetic nuclei and the external field and takes the same form of (2.15) with g_e and β_e replaced by their nuclear counterpart g_n (a positive property) and β_n respectively. Accordingly the nuclear Zeeman eigenvalue equation is given by

$$\hat{\mathbf{I}} \left|\psi\right\rangle = M_I \left|\psi\right\rangle \tag{2.23}$$

where $\hat{\mathbf{I}}$ is the nuclear spin operator and M_I is is corresponding eigenvalue. The mathematics of the nuclear spin operator are the same as electron spin with the only difference being that the sign of the nuclear Zeeman g-factor is positive. The nuclear Zeeman term of the spin Hamiltonian thus given

$$\hat{H}_{NZ} = -g_n \beta_n \mathbf{B}^T \cdot \hat{\mathbf{I}} \tag{2.24}$$

The selection rules for allowed EPR transitions are $\Delta M_s = 1$ and $\Delta M_I = 0$. The nu-

clear Zeeman term is required when calculating the energy levels, but when interested in transitions between levels the nuclear Zeeman terms cancel since allowed transitions occur between states labeled with the same $|M_I\rangle$, and thus this term nuclear Zeeman plays no role in spectroscopic analysis.

2.2.2.5 Field Independent Terms

The hyperfine term ($\hat{H}_{HF}$), is due to the coupling of the nuclear spin from neighboring nuclei and the unpaired electron spin of the paramagnetic center. The magnetic moment of a neighboring nuclei has a effect on the shape of wave function probability density [32]. Fermi proved that for systems with one electron the magnetic energy for isotropic interaction is given by

$$U_{iso} = -\frac{2\mu_0}{3}|\Psi_0|^2 \mu_{EZ}\mu_{NZ} \tag{2.25}$$

where Ψ_0 represents the electron wavefunction evaluated at the point nucleus and μ_{EZ} and μ_{NZ} are the electron and nuclear magnetic moments respectively (reference equation 2.4) [32]. The isotropic hyperfine magnetic energy is derived by substituting the quantum operator (denoted with a circumflex) for the respective electron and nuclear magnetic moments given by

$$\hat{\mu}_{EZ} = \gamma_e \hat{\mathbf{S}}\hbar = -g\beta_e \hat{S}_z \tag{2.26}$$

$$\hat{\mu}_{NZ} = \gamma_n \hat{\mathbf{I}}\hbar = g_n\beta_n \hat{I}_z \tag{2.27}$$

in to (2.25) yields

$$\hat{H}_{iso} = \frac{2\mu_0}{3}|\Psi_0|^2 g g_n \hat{S}_z \hat{I}_z \tag{2.28}$$

In equation (2.26) the g value is not the free-electron value g_e, but is generalized, as

the electron spin is coupled to the neighboring nuclei spin. Equation (2.28) can be simplified by combining the terms that precede the two spin operators as

$$\hat{H}_{iso} = A_0 \hat{S}_z \hat{I}_z \tag{2.29}$$

where A_0 is the hyperfine coupling constant, which measures the interaction energy between the electron and the paramagnetic nucleus. [32] As in equation (2.13), when B is along an arbitrary direction, $\hat{H}_{iso}$ should be expressed in its most general form

$$\hat{H}_{iso} = A_0 \hat{\mathbf{S}}^T \cdot \hat{\mathbf{I}} \tag{2.30}$$

Akin to equation (2.21), when the hyperfine coupling is anisotropic due to the dipole-dipole interaction of the electron and the magnetic nucleus, the hyperfine spin Hamiltonian term becomes

$$\hat{H}_{HF} = \hat{\mathbf{S}}^T \cdot \mathbf{A} \cdot \hat{\mathbf{I}} \tag{2.31}$$

where the hyperfine parameter ($\mathbf{A}$) also takes the form of a 3×3 matrix. The hyperfine parameter matrix $\mathbf{A}$ can be thought of as composed of isotropic and anisotropic elements such that

$$\mathbf{A} = A_0 \hat{\mathbf{1}} + \hat{\mathbf{T}}$$

where $\hat{\mathbf{1}}$ the unit operator and $\hat{\mathbf{T}}$ is a traceless (meaning the diagonal elements sum to zero) symmetric matrix called the hyperfine dipolar interaction matrix.

The electron and nuclear Zeeman terms, and the hyperfine term, are the only terms used to model the point defects in $BaGa_4Se_7$ and LiB_3O_5 in this dissertation. A full treatment of all spin Hamiltonian terms can be found in references [32] and [34].

For systems with more than one unpaired electron, $S > \frac{1}{2}$, there is a contribution to the spin Hamiltonian from the interactions between electrons; a spin-spin inter-

action. For such a system ($S > \frac{1}{2}$) there is both an electron-electron exchange (aka crystal field) interaction, and an electron-electron dipole interaction. This phenomena, commonly referred to as "zero field" splitting, as the energy levels are split by the crystal field and dipole interactions in the absence of an external applied magnetic field. Zero field splitting is of primary concern in the transition metal ions. The spin Hamiltonian term that describes the zero field interaction is

$$\hat{H}_{ZF} = \hat{\mathbf{S}}^T \cdot \mathbf{D} \cdot \hat{\mathbf{S}} \tag{2.32}$$

where the electronic quadrupole factor ($\mathbf{D}$) takes the form of a traceless 3×3 matrix. The derivation of (2.32) is also included in the full derivation of equation (2.21) detailed in chapter 4.8 and appendix A.6 of [32].

Akin to the zero-field splitting, when a nucleus has a spin $I > \frac{1}{2}$ there is a contribution to the energy of the spin state due to the nuclear quadrupole interaction. The quadrupole interaction, represented by the quadrupole coupling matrix Q, encompasses both the quadrupole moment , which reflects the charge distribution or shape of the nucleus, and the electric field gradient at the nucleus due to the surrounding electrons. The spin hamiltonian term that describes the quadrupole interaction is

$$\hat{H}_{NQ} = \hat{\mathbf{I}}^T \cdot \mathbf{Q} \cdot \hat{\mathbf{I}} \tag{2.33}$$

where ($\mathbf{Q}$) takes the form of a traceless 3×3 matrix. In EPR measurements the nuclear quadrupole effects are not routinely observed.

2.2.3 Optical Spectroscopy

When impurities are added into a semiconductor, additional energy levels are introduced into the bandgap. Dopant impurities that donate excess electrons (relative

to the host atoms they replace) are called donors, while dopant impurities which have a deficit of electrons (relative to the host atoms they replace) are called acceptors. Accordingly, the intermediate bands are commonly called donor levels (below the conduction band minimum) and acceptor levels (above the valence band maximum). Transitions can occur between these intermediate bands and the conduction and valence bands, and also between the intermediate bands themselves called intraband transitions.

There are two general categories of luminescence centers of interest in this dissertation: color centers and paramagnetic ion impurities. One example of a color center is called an "F-center" where an electron is trapped by an anion vacancy. The missing anion has a positive effective charge, and attracts an electron, which couples energetically with the phonon modes of the host. This hole-center is not attributed to cation vacancies, but rather a hole binding two neighboring anions [35]. The absorption frequency of the F-center is approximately proportional to a^2 where a is the cation-anion separation distance in the crystal.

Impurity paramagnetic ions, particularly those from the transition-metals, exhibit coupling of the electronic states to the vibrational modes of the crystal though the crystal field effect. The crystal-field energy coupling consists of both a static effect, from the presence of the host ions and their contribution to the electric field at the site of the defect; and a dynamic effect due to the vibrations of the ions in the crystal that subsequently alter the electric field at the defect site. The phonon modes that describe the vibrational motion of the ions within the crystal lattice, act as a source of amplitude modulation of the static crystal field [15]. The relative magnitudes of the crystal field effect compared to the spin-orbit coupling effect vary greatly between the transition metals and rare-earth elements, thus care must be taken in the ordering of the spin Hamiltonian terms such that the order of energy perturbation terms proceed

in order of precedence.

Optical spectroscopy (absorption and photo-emission), combined with EPR spectroscopy, are useful in measuring the concentration of point defects in crystals. Beer's law describes the change in light intensity as it propagates through the medium. Given the initial and final intensities and the sample thickness the concentration of the absorption ion can be calculated using Beer's law:

$$I(z) = I_0 e^{(-N\sigma_s z)} \tag{2.34}$$

where I_z represents the light intensity as a function of distance, I_0 is the initial intensity of the light, z is the thickness of the sample (measured along the direction of light propagation), N is the number of scattering centers per unit volume and σ_s is the scattering cross-section of the scattering center.

Photoluminescence is the re-emission of light from a substance after absorbing a photon of higher energy. These transitions can occur between the valence and conduction bands, called interband luminescence which is a radiative process during which an electron and a hole recombine and light is emitted as a result. This transition between bands may be of two types: direct transition and indirect transition. Conservation of energy dictates the relationship between the incoming light and the energy gap between the conduction and valence bands. Photons, light quanta, carry little to no momentum as opposed to phonons, vibrational quanta, which do carry momentum. Conservation of momentum determines the type of transition between bands. A direct gap transition, where $\Delta\vec{k}$ is near zero (i.e. the Brillouin zone center), is a purely radiative process. For indirect gap transitions the conduction band minimum and the valence band maximum are not co-located at the same point in k-space (i.e. within the Brillouin zone). Indirect transitions require an additional non-radiative process involving the creation or absorption of phonons, to accompany

the radiative process. The conservation of energy equation describing the excitation of an electron from the valence (initial state) to the conduction band (final state) in an indirect process is given below.

$$E_f = E_i + \hbar\omega \pm n\hbar\Omega \tag{2.35}$$

where $\hbar\omega$ is the photon energy, n is a positive integer, and $\hbar\Omega$ is the quantized (by integer n) phonon energy. The conservation of momentum equation describing this same process is given as

$$\hbar k_f = \hbar k_i \pm \hbar q \tag{2.36}$$

where k represents the electron wave vector and q the phonon wave vector. The $\pm$ sign accounts for phonon absorption or emission respectively [15]. During photon absorption the electron is excited from the ground state to an excited state and then relaxes through non-radiative emission (phonon emission) to the bottom edge of the excitation band. Solving equation (2.35) for the absorbed and emitted photon energy yields

$$\hbar\omega_a = (E_f - E_i) + n\hbar\omega \tag{2.37}$$

$$\hbar\omega_e = (E_f - E_i) - n'\hbar\omega' \tag{2.38}$$

The quantum number n and angular frequency ω for the absorption and emission process are not necessarily the same for both processes and are differentiated with a prime superscript. By comparing (2.37) and (2.38) it is clear that the emission in a vibronic system generally occurs at a lower energy. This is termed "Stokes shift". These equations show that electronic state of an impurity atom, localized near specific lattice sites in a crystal, couples with the host crystal's vibrational phonon modes.

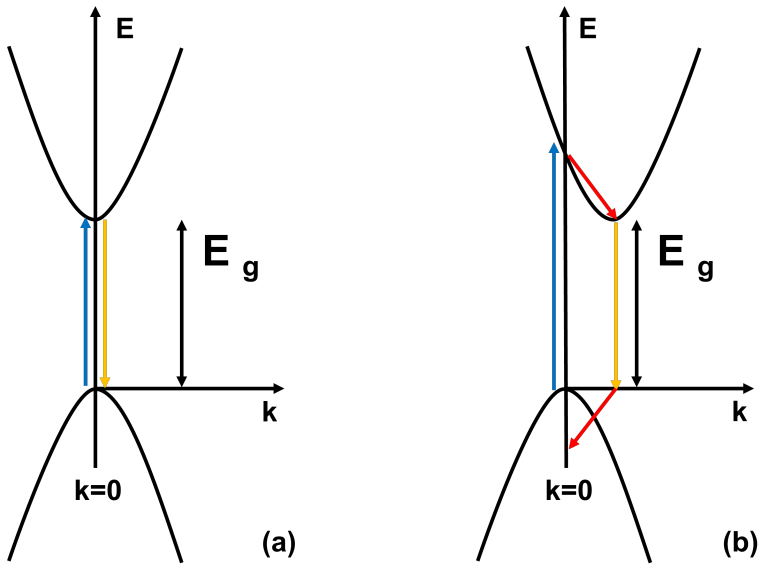

Figure 2.6. Configuration coordinate diagrams of the direct (a) and indirect (b) inter-band luminescence processes. The blue and yellow arrows represent the light energy input and output respectively. The red arrows in the indirect process represent the non-radiative phonon assisted relaxation processes. The band gap is represented by the difference in energy between the minimum of the conduction band and the maximum of the valence band. The phonons carry both energy and momentum and thus the locations of the energy minimum of the conduction band and the energy maximum of the valence band are shifted in k-space.

Both EPR and optical spectroscopy techniques will be used in this dissertation to identify and characterize the nature of point defects in crystals. Specifically, these two methods can identify the defect and its local atomic environment, charge state, orientation, relative concentration, and environmental conditions for generation, which may either help or hinder in the material's application.

3. Experimental Setup

3.1 Electron Paramagnetic Resonance Spectrometer

EPR spectroscopy is the measurement and interpretation of the interaction between electromagnetic radiation and the spin magnetic moments of unpaired electrons when placed in a magnetic field. The AFIT EPR laboratory is equipped with an X-band Bruker EMX spectrometer. The main functional components of the EPR spectrometer are: the microwave bridge, the magnet system, and the resonant cavity. This section provides a brief explanation of these main components, and their primary sub components. A complete explanation of all the components and spectrometer operation are available in other resources [32, 36].

3.1.1 Microwave Bridge

A diagram of the functional sub-components of the microwave bridge is shown in Figure 3.1. These sub-components are: the microwave source, the variable microwave attenuator, the circulator, the reference arm, and the detector. Microwaves are transmitted throughout the spectrometer via waveguides in two distinct paths. The main path is from point A in figure 3.1 through points C and D, and end at the detector located at point G. A parallel reference path in figure 3.1 carries microwaves from point A through point F, which are then also passed to the detector at point G.

3.1.1.1 The Microwave Source and Variable Attenuator

The microwave radiation source is a Gunn diode (an n-type semiconductor) biased so that it functions as an oscillator, operating in the X-band, corresponding to a frequency range of 8 -12 GHz. To control the power of the microwaves seen by the sample, the source is followed by a variable attenuator.

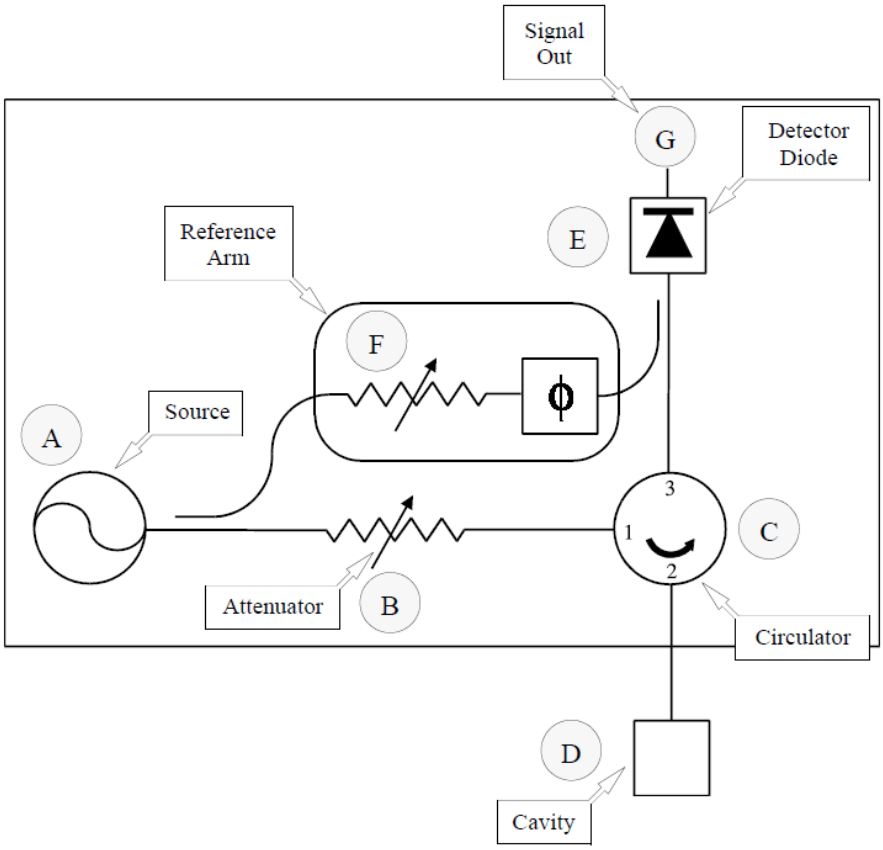

Figure 3.1. Block diagram of the functional sub-components of the microwave bridge used for EPR measurements. Reprinted with permission from [36].

3.1.1.2 The Circulator

A circulator is used to ensure that the microwaves directed to the resonant cavity are not reflected back towards the source, and that only the reflected microwaves from the cavity arrive at the detector. Shown as "C" in figure 3.1, the microwaves entering port 1 of the circulator only go to the resonant cavity through port 2 and not directly to the detector through port 3.

3.1.1.3 The Detector and Reference Arm

The detector consists of a Schottky barrier diode. The reflected microwaves from the resonant cavity cause an impedance mismatch, and thus a voltage, and this volt-

age is converted to an electrical current by the Schottky diode. The diode is forward-biased, via microwaves in the reference arm, to keep it operating in the linear region of the current-voltage curve (approximately 200 microamperes), where the diode current is proportional to the square root of the microwave power. The bias voltage is adjustable, and the microwaves pass through a phase shifter to ensure that the reference arm microwaves are in phase with the reflected signal microwaves from the resonant cavity. At the detector, a reference signal of the same frequency and phase as the source is provided to eliminate extraneous signals. The phase sensitive detector produces a DC current that is proportional to the amplitude of the modulated EPR signal. A comparison of the frequency and phase of the modulated field and the modulated EPR signal allows for reduction of signals that do not match in terms of frequency and phase. The EPR signal is modulated and described in section 3.1.3.

3.1.2 Magnet System

The magnet system consists of a pair of water-cooled electromagnets, a regulating power supply, and a Hall probe field sensor. The magnets produce a uniform magnetic field over the sample region and provide the magnetic field that causes the splitting of the spin energy levels. The pair of iron-core magnets are positioned such that the resonant cavity lies in the center of the two coils. The Hall field sensor is a probe placed in the gap between the two coils, and produces a voltage that is dependent on the magnetic field directed perpendicular to the probe. A microprocessor compares the voltage reading from the Hall sensor with a reference voltage as the field is swept, and any differences between the probe value and the reference value triggers a correction voltage in the power supply. This feedback system adjusts the current through the electromagnet winding such that the Hall-probe voltage remains fixed. In a typical EPR experiment the microwave frequency is held constant, while

the magnetic field is slowly swept between 50 - 1400 Gauss. To account for the small difference in distance between the location of the Hall-probe and the center of the resonant cavity a small correction is applied to the magnetic field values. This field correction procedure is detailed by Dr. Scherrer [37].

3.1.3 Resonant Cavity

The resonant cavity is a metal box, rectangular or cylindrical in shape, constructed in a way that standing electromagnetic waves are formed between the cavity walls at a narrow range of frequencies, $\Delta\nu$, with a resonance peak at ν_{res}. Microwaves at a frequency within this narrow range resonate inside the cavity such that the magnetic field intensity builds up in the center of the cavity where the sample is located, and so no microwaves are reflected back outside of the cavity. The coupling of the microwaves to the inside of the resonant cavity is aided by an adjustable iris screw. The iris is a small hole at the back of the resonant cavity with a Teflon screw that adjusts the aperture through which the microwaves enter the cavity. Raising or lowering the Teflon screw in the cavity allows the cavity to be tuned once a sample is inserted. When the iris screw is adjusted such that no microwave reflections are emitted from the resonator, the cavity is "critically coupled". Each microwave cavity is designed with its own resonant frequency, such that the driving magnetic field is oriented perpendicular to the slowly varying magnetic field from the electromagnets, and is quantified by a quality factor, Q. The quality factor describes how effectively the cavity stores energy and is calculated by $Q = \nu_{res}/\Delta\nu$. Energy can be lost to the side walls of the cavity due to the electric currents generated by the microwaves. The electric field (from the microwaves) is minimum at the cavity center while the magnetic field (again from the microwaves) is maximum at the center because the two fields are exactly out of phase with each other. This spatial distribution of the

electric and magnetic fields is taken advantage of by placing the sample in the center of the cavity where the electric field is minimum and the magnetic field is maximum, as it is the magnetic field that drives the spin state transition.

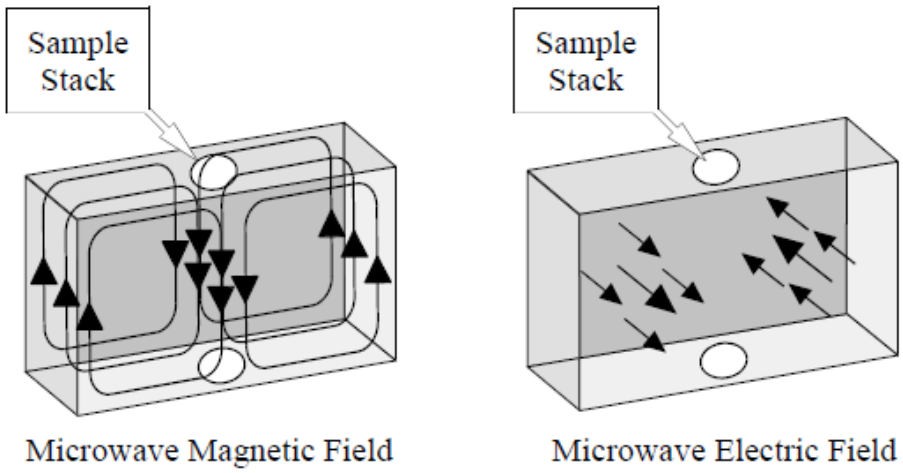

Figure 3.2. Electric and magnetic fields generated by the microwaves inside the resonant cavity. Reprinted with permission from [36].

The resonant cavity is also designed such that it supports a 100 kHz sinusoidal modulation of the magnetic field from the electromagnet provided by a pair of Helmholtz coils located on each side of the magnet cavity along the axis of the slowly varying field [32]. This oscillating magnetic field is superimposed on the slowly-varying magnetic field of the electromagnet. This modulation of the magnetic field in turn modulates the resonance condition; thus the EPR absorption response is also modulated [38]. Due to this field modulation, it is the slope of the EPR absorption spectrum that is measured and the absorption shape is transformed into a detected sine wave and displayed as a first derivative signal from the detector. The comparison of this modulated field with the frequency and phase of the microwaves in the reference arm is called phase-sensitive amplitude detection. The amplitude of this sine wave is proportional to the slope of the absorption curve and yields information about the relative concentration of the paramagnetic defect responsible for the absorption.

This technique allows for amplification of the EPR signal, elimination of most noise-producing components, and enhanced spectral resolution through a phase locking detection system. Excessive modulation of the amplitude can lead to adverse affects such as line broadening. The modulation amplitude, measured in Gauss, should be kept at a fraction of the hyperfine width measured between successive peaks. When the modulation amplitude is greater than the resonance peak the EPR signal becomes distorted and the hyperfine pattern is unresolved. Lastly, the resonant cavity used in this dissertation was constructed with optical slits that allow external light sources to interact with the sample during EPR data collection. Various coherent light sources were used to manipulate the charge state, and thus the paramagnetic state, for some of the defects investigated for this work.

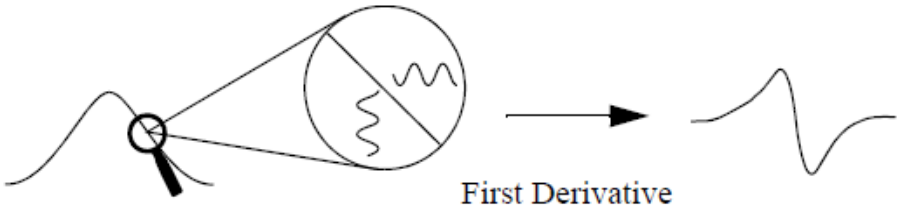

Figure 3.3. Field modulation and phase sensitive detection. The modulated field amplitude is a fraction of the linear portion of the absorption line. Reprinted with permission from [36].

The Bruker EPR spectrometer at AFIT is also fitted for use with an Oxford helium-gas flow system that allows for low-temperature EPR data collection, as low as five Kelvin. Often, low temperatures are required to slightly slow the spin-lattice relaxation so that the EPR transition is captured by the spectrometer. The spin-lattice relaxation is determined by the energy coupling between the paramagnetic species and the local environment of the crystal lattice. This coupling allows energy to flow from the spin system (electronic) to the thermal reservoir (vibrational) of the crystal lattice [39]. This energy coupling is commonly termed "vibronic", being it is an energy coupling between electronic and vibrational energy levels. This is most

readily understood through a simple analysis of the Heisenberg uncertainty principle, expressed in terms of the uncertainty in energy and lifetime of the excited spin state, combined with the Maxwell-Boltzmann statistical distribution of energy levels. The uncertainty in energy and lifetime of the spin state is expressed as

$$\Delta E \cdot \Delta t \sim \hbar. \tag{3.1}$$

Assuming that the electronic Zeeman term is dominant, using equation (2.15) of Chapter 2 to express the change in energy of the spin state yields

$$\Delta E = h\Delta\nu = g_e\beta_e\Delta B_z. \tag{3.2}$$

Inserting this expression for E into the uncertainty expression yields a relationship between the change in energy and the lifetime of the excited spin state,

$$\Delta\nu = g_e\beta_e\Delta B_z/\hbar \sim 1/2\pi\Delta t. \tag{3.3}$$

By lowering the temperature the lifetime of the excited spin state, Δt, is slightly increased, and the uncertainty in energy ΔE is decreased. If the lifetime of the excited spin state is too long then the EPR signal approaches zero width and becomes undetectable. The relationship between ΔE and the temperature of the excited spin state, T_s, for a two-level system is given by the Maxwell-Boltzmann distribution of energy levels, where the ratio of the populations of the upper and lower levels are given by

$$\frac{N_2}{N_1} = e^{\frac{-\Delta E}{k_b T_s}}. \tag{3.4}$$

Here N_2 and N_1 are the populations of the upper and lower spin energy levels respectively, k_b is the Boltzmann constant, and T_s is the spin temperature. When T_s

becomes large the ratio of populations approaches unity and the spin-state is saturated such that no more spins can be excited to the upper energy state. Thermodynamic equilibrium occurs when T_s decreases to the surrounding lattice temperature, T_l. For the defects studied in this dissertation warmer temperatures resulted in a broadening of the EPR signal. In practice, both the temperature and the microwave power are adjusted to avoid saturation and achieve the best EPR signal-to-noise ratio.

A picture of the AFIT EPR spectrometer and helium gas-flow system is shown in Figure 3.5.

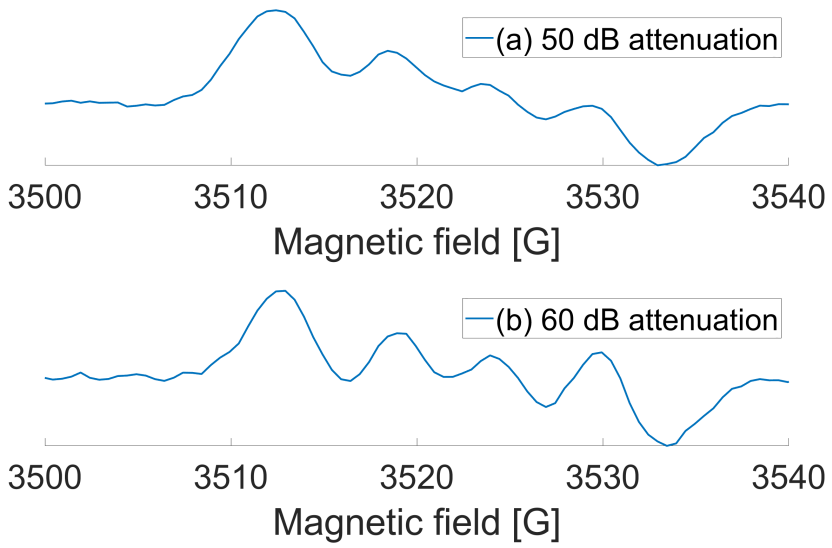

Figure 3.4. An example of EPR signal saturation from an LiB_3O_5 crystal taken at 55K after 2 min x-ray irradiation. By reducing the power by 10 db from 50 db attenuation in (a) to an attenuation of 60 dB in (b) the resolution of the additional hyperfine is improved.

Figure 3.5. Experimental configuration of the EPR Bruker EMX spectrometer for operation with liquid helium at AFIT.

3.2 Cary 5000 Spectrophotometer

The crystals studied in this dissertation are used in devices to generate tunable light, and within that community, the attenuation of the light is what is of interest

as both scattering and absorption effects negatively affect device performance. The Cary 5000 is an optical spectrophotometer operating in the ultraviolet (UV), visible (VIS), and near infrared (NIR), capable of measuring the transmission and reflection properties of a material as a function of the wavelength of light incident on the sample. The spectrophotometer was set to operate in double-beam transmission mode in the visible spectrum for all absorption data in this dissertation. For optical absorption measurements at liquid nitrogen temperatures, the Cary 5000 was configured such that the sample was placed in a variable temperature cryostat, manufactured by Cryo Industries. This liquid nitrogen dewar has two sapphire optical windows aligned along the sample beam path. A double-beam spectrophotometer compares the light intensity between two light paths, namely the sample path and the reference path, and computes the transmittance defined as the ratio of the transmitted ($I(z)$) and incident (I_0) light intensities.

$$T = I(z)/I_0 \tag{3.5}$$

Absorbance measures the ability of a material to absorb light. The mathematical relationship between absorbance and transmittance is

$$\text{Abs} = \log_{10}(1/T) \tag{3.6}$$

where Abs is the absorbance and T is the transmittance. In contrast to absorbance, optical density (abbreviated OD) incorporates scattering and absorption and is a measure of attenuation, and is related to the transmission percent by the expression $OD = \log_{10} \frac{100}{T}$, where transmission T is expressed as a percentage. Optical absorption graphs in this dissertation are presented in terms of the optical density of the material as a function of the wavelength to which the crystal is being exposed. The main functional components of the Cary 5000 spectrophotometer are: the light source,

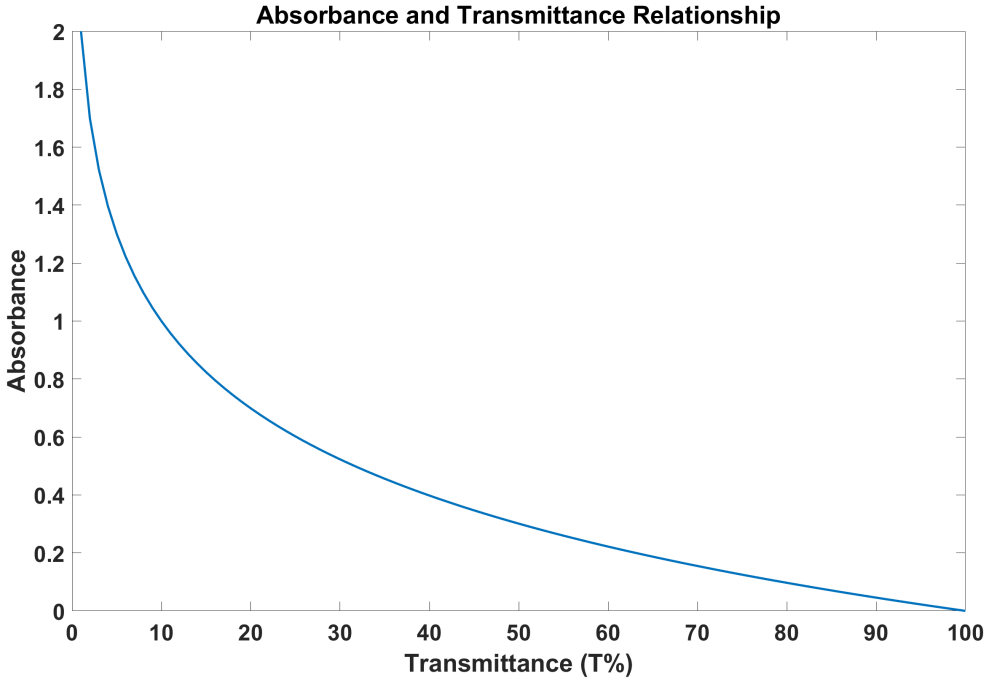

Figure 3.6. The logarithmic relationship between absorbance and transmittance. A transmittance of 100% equates to an absorbance of zero. A transmittance of 10% equates to an absorbance of unity.

the monochromator, the light chopper, and the detector. This section provides a brief explanation of these main components and their primary subcomponents.

3.2.1 Spectrophotometer Source

The Cary 5000 has two light sources; a deuterium arc lamp for the UV, and a quartz-halogen lamp for the Vis through NIR spectrum. The intensity of the deuterium arc lamp declines dramatically above 400 nm. The quartz-halogen lamp is useable down to approximately 250 nm. Only the quartz-halogen lamp was used for data collection in this dissertation. A diagram showing the optimal choices for source and detector as a function of the scanning wavelength range is shown in figure 3.8.

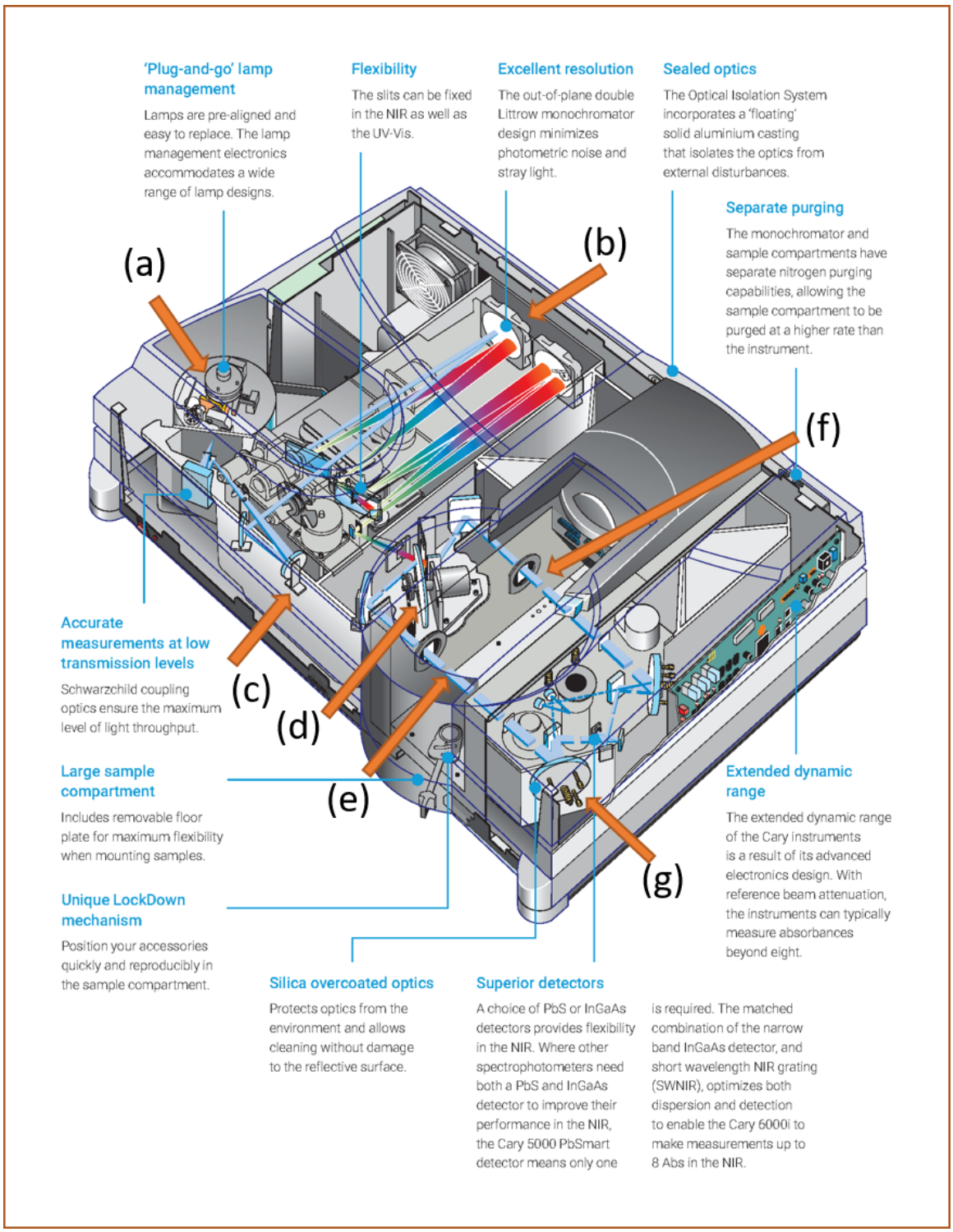

Figure 3.7. A diagram of the main components of the Cary 5000 spectrophotometer operating in double-beam mode including the: (a) light source, (b) monochromator, (c) spectral band width (SBW) aperture, (d) light chopper, (e) sample path, (f) reference path, and (g) detector. Reprinted with permission from [40]

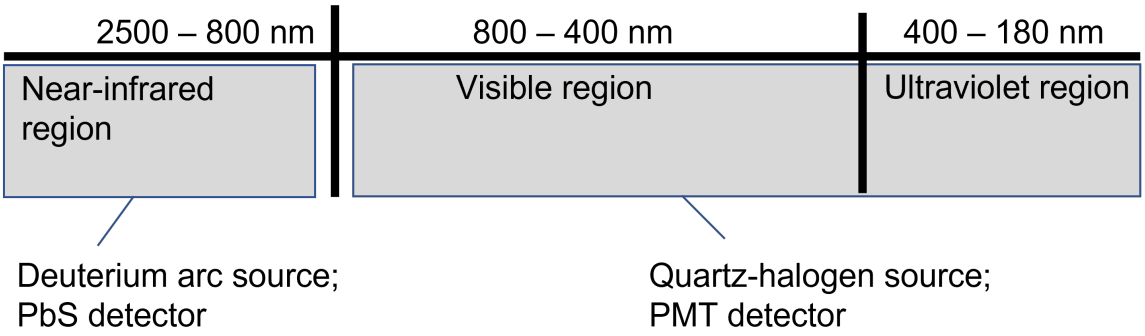

Figure 3.8. A diagram of the spectral dependence determining the optimal Cary 5000 source and detector choices.

3.2.2 Spectrophotometer Monochromator

The source lamp light is columnated into a beam that is then incident upon a diffraction monochromator which disperses the light into discrete wavelengths. The monochromator uses a rotating grating to disperse the light in a range of wavelengths [31]. A dedicated stepper motor is used to turn the grating and reduce the vibration and mechanical backlash. This motor is capable of turning the grating at 16,000 nanometers per minute (nm/min) when scanning in the UV/Vis region, and 64,000 nm/min when scanning in the NIR region. The mathematical formula that determines the wavelength of light dispersed from the grating is

$$a \sin \theta = m\lambda \tag{3.7}$$

where a is the line spacing between the gratings, m is the order of the reflection (unity is most cases), and λ is the wavelength of the emitted light [31]. This allows the spectrophotometer to scan through a wide range of wavelengths. At the exit port of the monochromator there is an adjustable aperture that controls the spectral band width (SBW) of the light. When transmission through the sample is high, increasing the SBW lowers the energy setting and detector resolution to avoid saturation. Reducing the SBW increases the the resolution of the detector. All absorption measurements

in this dissertation were taken with fixed SBW set to 2 nm, such that the energy at the detector is changed to maintain a constant signal and constant resolution level through the entire wavelength scan.

3.2.3 Spectrophotometer Light Chopper

After the light passes through the adjustable aperture, it is incident on a three-way light chopper. As depicted in figure 3.9, the light chopper is a rotating disc, with a rotational frequency of 30 Hz, and is divided into three equal sections. One section of the light chopper is transparent and passes light from the monochromator to the sample (sample path). The second section of the light chopper is a mirrored surface which reflects the light and through series of mirrors (reference path). The third section of the light chopper is a matte black surface that absorbs the light, which provides a temporal window for grating changes in the monochromator. The intensity at the detector from both the sample and reference paths is averaged during this time period. This method of changing the diffraction grating during the non-measurement phase minimizes the "dark current" in the detector and improves the resolution at the detector when comparing the intensities between the sample and reference paths.

3.2.4 Spectrophotometer Detectors

The Cary 5000 is equipped with two detectors; one photomultiplier tube (PMT) optimized for detection in the UV/Vis region and a lead sulphide (PbS) detector optimized for detection in the NIR. The PbS detector response decreases dramatically below 700 nm. To ensure the detector readings remain in their optimum range two methods are used, one for each detector. The PMT allows large changes in gain with applied voltage, whereas with the PbS detector this is not traditionally possible [41].

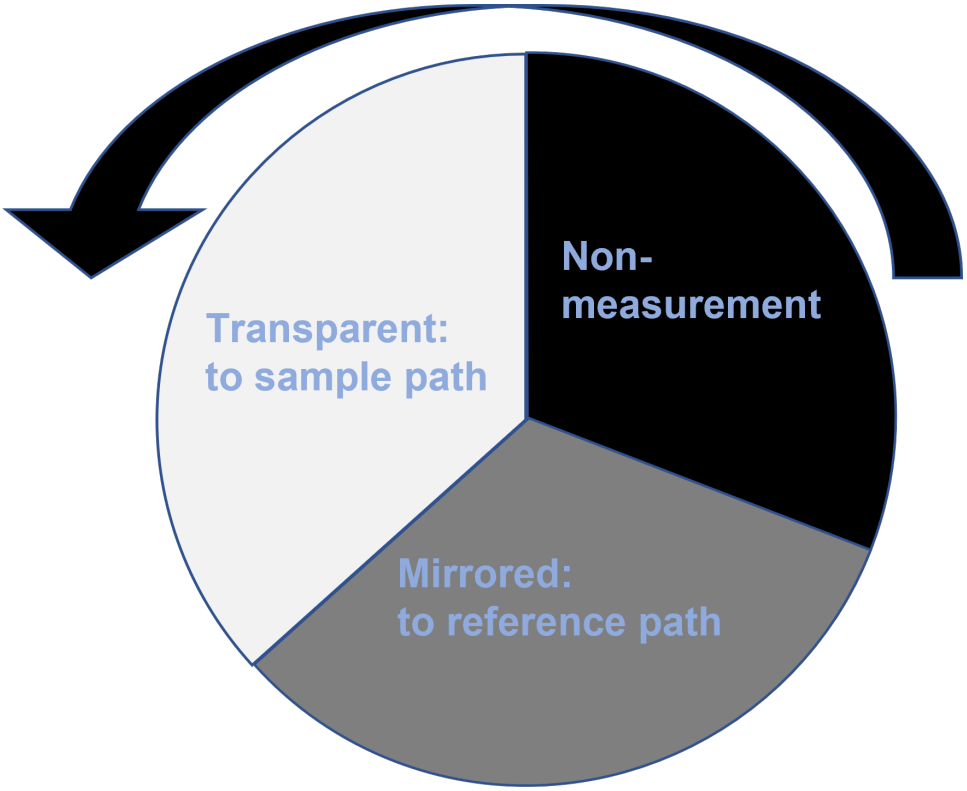

Figure 3.9. Diagram of the three-phase light chopper used to generate the sample path, reference path, and a non-measurement phase for grating changes. Light from the monochromator incident on the transparent portion passes through and is incident on the sample. Light from the monochromator incident on the mirrored portion is reflected into the reference path. Light from the monochromator incident on the matte black surface is absorbed and allows time for changes to the grating and selection of the next wavelength.

When using the PMT detector, the SBW is held fixed and the gain at the detector is adjusted to obtain the best signal-to-noise ratio [41]. When using the PbS detector, the spectral band width is adjusted by varying the amount of light that reaches the detector to obtain the best signal-to-noise ratio [41]. The sample and reference beams are recombined before reaching a detector. If no light is absorbed, then the recombined beams will be exactly out-of-phase. If any absorption occurs, then the recombined beams will induce a signal in the detector.

4. Optically Active Selenium Vacancies in $BaGa_4Se_7$ Crystals

4.1 Abstract

Barium gallium selenide ($BaGa_4Se_7$) is a recently developed nonlinear optical material with a transmission window extending from 470 nm to 17 µm. A primary application of these crystals is the production of tunable mid-infrared laser beams via optical parametric oscillation. Unintentional point defects, such as selenium vacancies, cation vacancies (barium and/or gallium), and trace amounts of transition-metal ions, are present in $BaGa_4Se_7$ crystals and may adversely affect device performance. Electron paramagnetic resonance (EPR) and optical absorption are used to identify and characterize these defects. Five distinct EPR spectra, each representing an electron trapped at a selenium vacancy, are observed at low temperature (there are seven crystallographically inequivalent selenium sites in the crystal). One spectrum is stable at room temperature and is present before illumination. The other four are produced at lower temperatures with 532 nm laser light and are thermally unstable at room temperature. Each S = 1/2 singly ionized selenium vacancy has a large, nearly isotropic, hyperfine interaction with ^{69}Ga and ^{71}Ga nuclei at one neighboring Ga site. A significant portion of the unpaired spin resides in a 4s orbital on this adjacent Ga ion and gives principal values of the hyperfine matrices in the 3350–6400 MHz range. Broad photoinduced optical absorption bands in the visible and near-infrared are assigned to the selenium vacancies.

4.2 Introduction

Growth of new, and often more complex, NLO crystals is a key enabling technology that allows increasingly versatile laser-based devices to be developed for use from

the ultraviolet to the mid-infrared and beyond [1, 12, 42, 43]. Present NLO applications include second harmonic generation, tunable optical parametric oscillation, and terahertz generation. NLO crystals are also expected to play important roles in the emerging fields of quantum information processing [44, 45]. A recent success has been the "discovery" of $BaGa_4Se_7$ crystals, with a room temperature transmission window from 470 nm to 17 µm. Yao et al [46] and Badikov et al [47] reported the growth of these crystals in 2010. Since then, the use of this material as an optical parametric oscillator (OPO) has been widely explored [5, 29, 30, 48–54]. Its potential for use in terahertz generation has also received attention [55–58]. Biaxial $BaGa_4Se_7$ crystals have large nonlinear optical coefficients, suitable birefringence, and a high threshold for laser damage [13, 59–61]. In an early demonstration of the material's capabilities, Kostyukova *et al.* [49] pumped a $BaGa_4Se_7$ OPO at 1064 µm and produced output over a broad range (2.7 -17 µm). Because of the wide bandgap of these crystals, intrinsic two-photon absorption loss is small when the pump wavelength is 1064 µm.

Unwanted optical absorption from point defects can be a significant problem for many nonlinear optical materials, including $BaGa_4Se_7$. For example, to realize maximum output power from an OPO, absorption bands located near the pump wavelength must be minimized. The defects do not need to be thermally stable at room temperature since the photoinduced production of short-lived charge states may introduce transient absorption features that affect device performance in steady-state applications or applications with high repetition rates. If a NLO crystal is to perform optimally in devices, the identities and properties of the more common defects in the material must be established and the processes by which the defects are created and eliminated must be determined. The defect-identification goal is best achieved by using electron paramagnetic resonance (EPR) [32, 62, 63], an experimental technique that has both the sensitivity and resolution needed to construct detailed

atomic-scale models of defects at the wavefunction level. Typical unintentional point defects encountered in NLO crystals are anion and cation vacancies, antisites, and transition-metal impurities. Anion vacancies are especially important as they are often a dominant defect in optical materials. When present, these vacancies produce optical absorption bands with large oscillator strengths, and they introduce changes in electrical and thermal conductivity.

In the present paper, we describe the production and characterization of singly ionized selenium vacancies (i.e., donors) in $BaGa_4Se_7$ crystals. Holes trapped by cation vacancies, most likely barium vacancies, are also investigated. Selenium vacancies are formed during growth, with most initially in the nonparamagnetic doubly ionized charge state (V_{Se}^{2+}). Since the crystals are electrically neutral, the selenium vacancies are compensated by acceptors such as cation vacancies and impurities on cation sites. For example, one Ba^{2+} vacancy will compensate one missing Se^{2-} ion and two Ga^{3+} vacancies will compensate three missing Se^{2-} ions. During illumination, the selenium vacancies trap electrons. Singly ionized, and thus EPR-active, selenium vacancies (V_{Se}^{+}) with one unpaired electron are produced when the $BaGa_4Se_7$ crystal is exposed to 532 nm laser light while being held at low temperature. Of the five V_{Se}^{+} spectra we observe, only one was present before exposure to laser light. The other four V_{Se}^{+} spectra are photoinduced. We provide a detailed analysis of the EPR spectra from these five V_{Se}^{+} vacancies. Each paramagnetic vacancy has a large interaction with a neighboring ^{69}Ga or ^{71}Ga nucleus. The resulting hyperfine patterns are complex because the energies of these interactions are comparable to the energy of the microwave photons used in the EPR spectrometer. This gives highly asymmetric sets of hyperfine lines around $g \approx 2.0$. We also report photoinduced optical absorption bands peaking between 430 and 750 nm at 80 K (these bands accompany the formation of the singly ionized selenium vacancy EPR spectra). A luminescence and optical

absorption study by Yelisseyev *et al.* [64] is the only previously published report that investigates point defects in $BaGa_4Se_7$ crystals.

4.3 Experimental Details

Two boules (different growth runs) of undoped $BaGa_4Se_7$ crystals were grown by the horizontal gradient freeze method at BAE Systems (Nashua, NH) [65]. Growth occurred in a transparent furnace using starting materials synthesized from high-purity elements by a two-temperature vapor transport process. The melting point of $BaGa_4Se_7$ is 1029 °C. After orienting with x rays, six small crystals (three from each growth run) suitable for optical and EPR experiments were cut from the larger boule. Approximate dimensions of these crystals were 2.5 × 3.2 × 3.3 mm^3. The samples used in our study were from the later growth run, and not subjected to a post-growth thermal anneal in a Se-containing atmosphere.

The EPR spectra were acquired with a Bruker EMX spectrometer operating near 9.38 GHz. An Oxford Instruments ESR-900 helium-gas flow system was used to control the sample temperature and a Bruker NMR gaussmeter provided corrections for the small difference in the magnetic field at the sample and the spectrometer's Hall sensor located on a magnet pole cap. A 532 nm laser from Laserglow Technologies (Model LCS-0532-TSD) was used to convert point defects to their paramagnetic charge states. Optical absorption spectra were taken with a Cary 5000 spectrophotometer and an ultrabroadband (250 nm to 4 µm) fused-silica wire-grid polarizer from Thorlabs (Model WP25M-UB). A Cryo Industries optical cryostat with sapphire windows (Model 110-637-DND) and a Lakeshore temperature controller (Model 335) were used when taking optical absorption data below room temperature. Reflection losses were not removed from the absorption spectra.

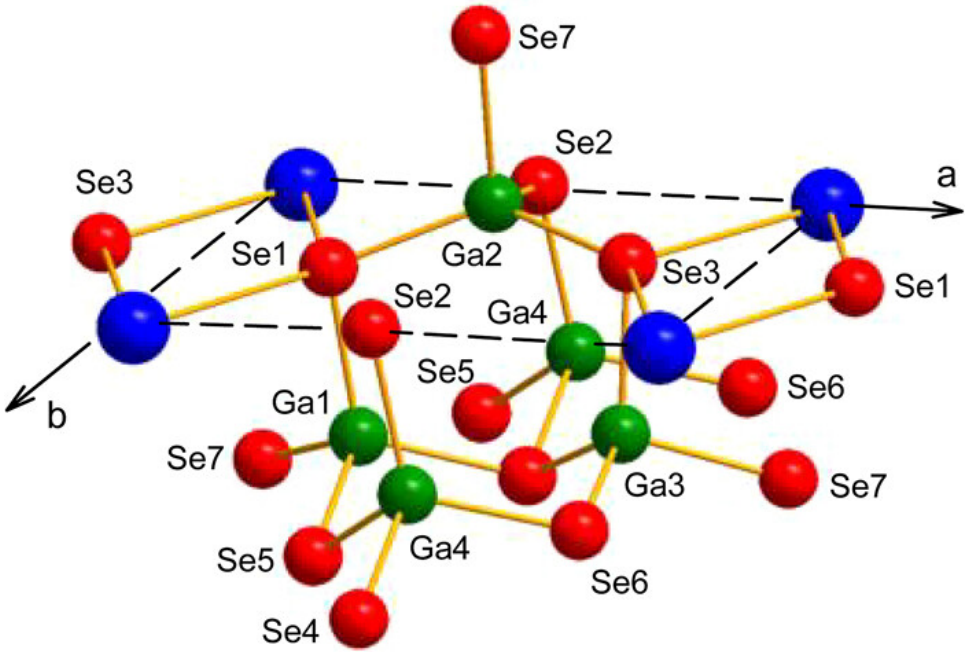

Figure 4.1. A ball-and-stick representation of a portion of the monoclinic $BaGa_4Se_7$ crystal. The barium ions are blue, the gallium ions are green, and the selenium ions are red. The four Ba^{2+} ions (connected by the dashed lines) lie in the a–b plane and form a rectangle with sides equal to the lattice constants a and b. Reproduced from [27] with the permission of AIP Publishing.

Ion	Ga neighbors	Distance from Se to Ga
Se1	Ga(1), Ga(2)	2.378, 2.401
Se2	Ga(4), Ga(2)	2.368, 2.383
Se3	Ga(3), Ga(2)	2.363, 2.373
Se4	Ga(3), Ga(3), Ga(4)	2.421, 2.431, 2.488
Se5	Ga(1), Ga(4)	2.364, 2.389
Se6	Ga(3), Ga(4)	2.362, 2.387
Se7	Ga(1), Ga(3), Ga(2)	2.451, 2.451, 2.478

Table 4.1. The Se^{2-} ions in a $BaGa_4Se_7$ crystal have either two or three close Ga neighbors. Specific ions are identified using the labeling scheme in Reference [46]. Distances are given in Å. Reproduced from [27] with the permission of AIP Publishing.

The $BaGa_4Se_7$ crystals have a monoclinic structure (space group Pc) with lattice constants a = 7.6252 Å, b = 6.5114 Å, c = 14.702 Å, and β = 121.24° at 93 K. The b direction is perpendicular to the mirror plane of the crystal, β is the angle

between the a and c axes, and the c* direction is defined to be perpendicular to the a–b plane. The Ba^{2+} ions and Se^{2-} ions are much larger in size than the Ga^{3+} ions. Effective ionic radii are 1.36 Å for Ba^{2+} ions, 0.47 Å for Ga^{3+} ions, and 1.98 Å for Se^{2-} ions [66]. A portion of the $BaGa_4Se_7$ structure is shown in Figure 4.1. The four Ba^{2+} ions in this figure are in the a–b plane (perpendicular to the c* direction). They define a rectangle, indicated by the dashed lines, with sides equal to the lattice constants a and b. One Ga^{3+} ion lies above the set of four Ba^{2+} ions, and four Ga^{3+} ions lie below. In the $BaGa_4Se_7$ lattice, all the Ba sites are equivalent (each Ba^{2+} ion has 12 Se^{2-} neighbors with Ba–Se distances ranging from 3.430 to 4.199 Å). The Ga ions occupy four crystallographically inequivalent sites. As expected for a Group III ion, each Ga^{3+} forms a distorted tetrahedron by bonding to four Se^{2-} ions. The Ga–Se distances in these tetrahedra range from 2.362 to 2.488 Å. There are seven crystallographically inequivalent Se sites in the crystal. These Se^{2-} ions have either two or three close Ga neighbors (specific neighbors and separation distances are listed in Table 4.1).

4.4 EPR Results

4.4.1 Electrons trapped at selenium vacancies

The EPR spectrum in Figure 4.2(a) was taken from an as-grown $BaGa_4Se_7$ crystal. The same crystal was then exposed to 532 nm laser light and the EPR spectrum in Figure 4.2(b) was taken. These spectra were obtained at 35 K with the magnetic field aligned along the b direction. The spectrum in Figure 4.2(a) is complex and we wait until Section 4.4.2 for its analysis. We first focus on the simpler photoinduced EPR spectrum that emerges when we subtract the "before light" spectrum in Figure 4.2(a) from the "during light" spectrum in Figure 4.2(b). This "difference" spectrum is shown in Figure 4.3(a). The 532 nm light produced two types of defects (neither

was present before the illumination). There is an intense single line at 329.33 mT in Figure 3(a) due to a hole trapped on a selenium ion adjacent to a cation vacancy. This defect is described in more detail in Section 4.4.3. The remaining EPR lines in Figure 4.3(a) are from two distinct singly ionized selenium vacancies, labeled V_{Se}^{+}(A) and V_{Se}^{+}(B). Linewidths for the two photoinduced vacancies are different: broad for V_{Se}^{+}(A) and narrow for V_{Se}^{+}(B). Since the energy of the 532 nm photons is less than the optical gap of the $BaGa_4Se_7$ crystal, we suggest that the singly ionized selenium vacancies are formed by the light when electrons are optically excited from the valence band to doubly ionized selenium vacancies V_{Se}^{2+}. This excitation process converts nonparamagnetic V_{Se}^{2+} vacancies to paramagnetic V_{Se}^{+} vacancies. Holes left in the valence band are localized at selenium ions adjacent to cation vacancies or at impurity ions. If the crystal remains near or below 70 K, these trapped electrons and trapped holes are thermally stable after the 532 nm light is removed.

In Figure 4.3(a), the concentration of defects represented by the trapped-hole spectrum is approximately 3.4×10^{18} cm^{-3} and the concentrations represented by the V_{Se}^{+}(A) and V_{Se}^{+}(B) selenium vacancy spectra are approximately 11.6×10^{18} cm^{-3} and 0.9×10^{18} cm^{-3}, respectively. These defect concentrations were obtained by comparing signal intensities to a Bruker weak-pitch EPR standard containing a known number of spins. Since the combined number of electrons trapped at selenium vacancies is more than three times greater than the number of holes trapped at cation vacancies, unseen defects must be present that serve as traps for holes. Among the candidates for these unseen defects are transition-metal ions with partially filled 3d shells or rare-earth ions with partially filled 4f shells. It is also possible that there are unseen impurities serving as electron traps.

The six lines assigned to V_{Se}^{+}(A) in Figure 4.3(a) are caused by a large hyperfine interaction with ^{69}Ga and ^{71}Ga nuclei located at one Ga site adjacent to the selenium

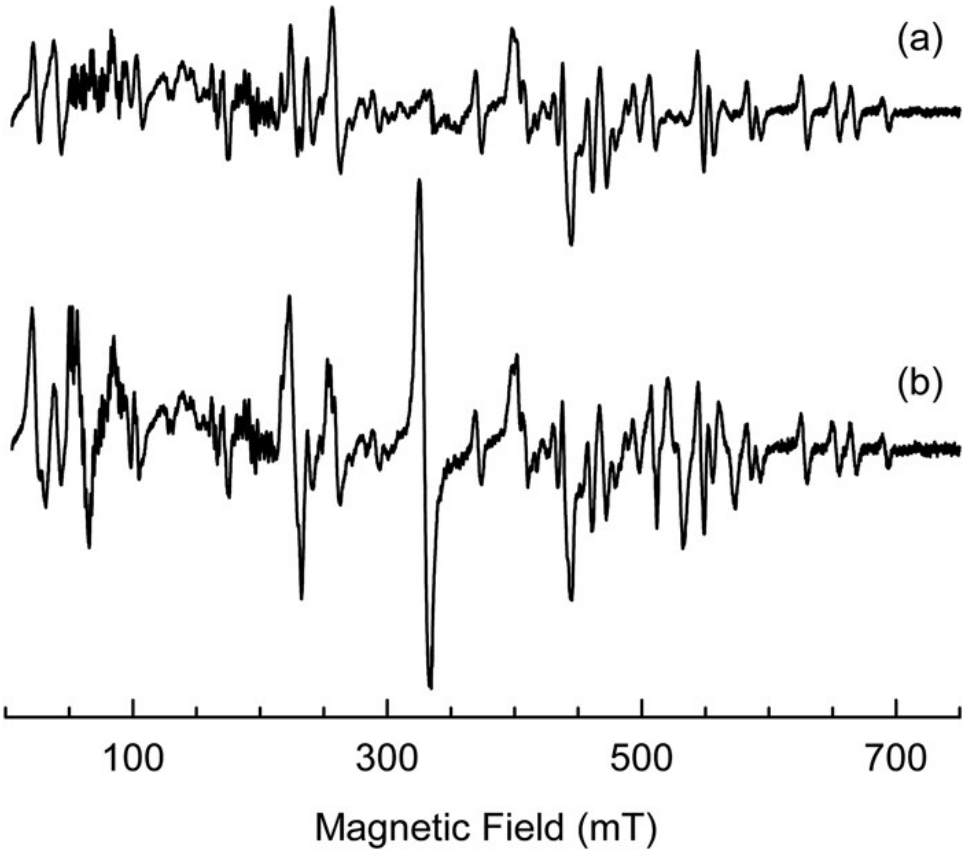

Figure 4.2. EPR spectra taken from $BaGa_4Se_7$ crystal sample 5Y1 (a) before exposure to light and (b) during exposure to 532 nm laser light. The temperature was 35 K and the magnetic field was along the b direction. Reproduced from [27] with the permission of AIP Publishing.

vacancy. Stick diagrams above the spectrum identify the four lines from the ^{69}Ga nuclei and the two lines from the ^{71}Ga nuclei. A slight splitting of these primary lines (i.e., the step at their centers) is caused by a much smaller unresolved hyperfine interaction with ^{69}Ga and ^{71}Ga nuclei at a second Ga site near the vacancy. The V_{Se}^{+}(A) EPR spectrum has very little angular dependence, with the highest-field lines shifting by less than 5 mT when the magnetic field direction is rotated from b to a. This establishes that a significant portion of the electron trapped by the selenium vacancy occupies a 4s orbital on the adjacent Ga ion. V_{Se}^{+}(A) can be viewed, to a first approximation, as a Ga^{3+} ($3d^{10}4s^{1}$) ion next to a selenium vacancy. The ^{69}Ga isotope has a natural abundance of 60.1% and the ^{71}Ga isotope has a natural abundance of

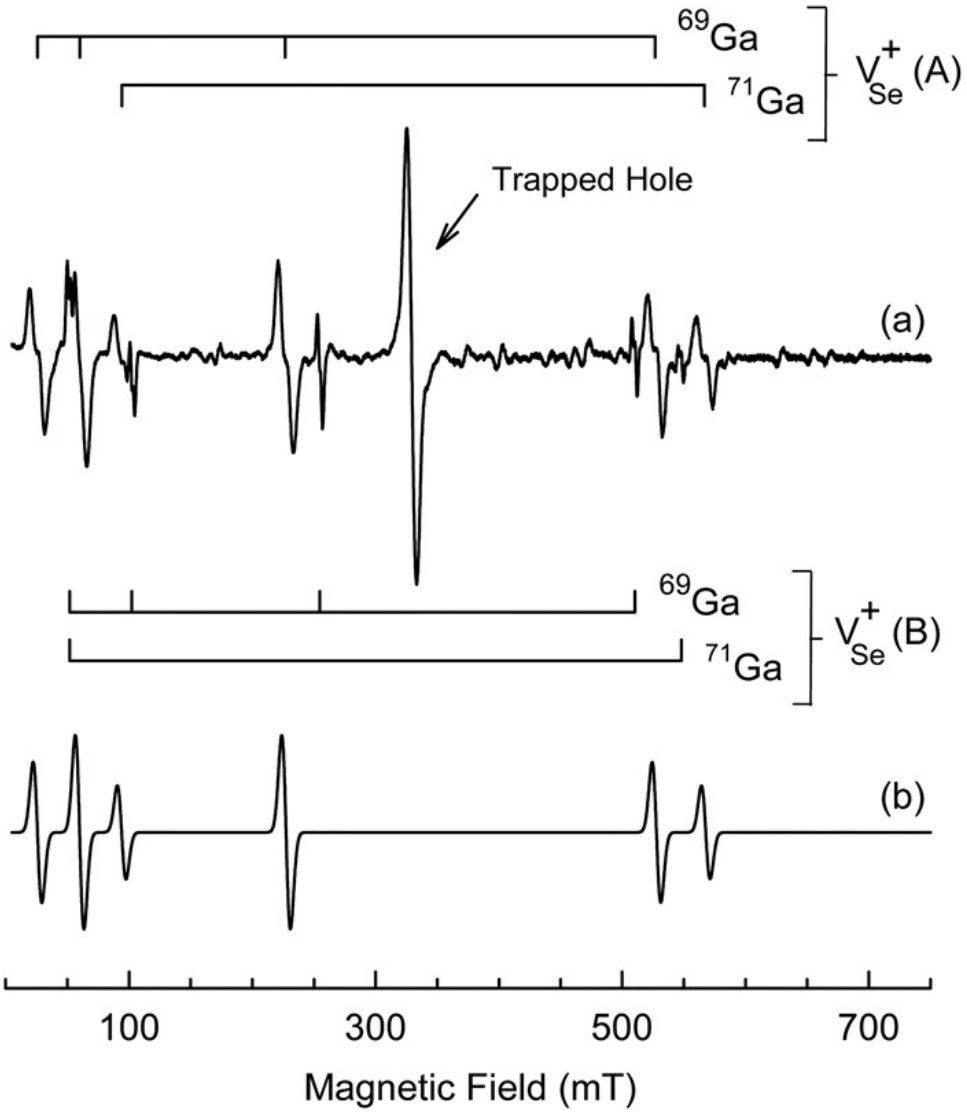

Figure 4.3. (a) Photoinduced EPR spectrum from $BaGa_4Se_7$ crystal sample 5Y1, taken at 35 K during exposure to 532 nm laser light. The "before light" spectrum in Figure 4.2(a) has been subtracted from the "during light" spectrum in Figure 4.2(b). One trapped-hole center and two singly ionized selenium vacancies, V_{Se}^{+}(A) and V_{Se}^{+}(B), have been produced by the light. The magnetic field is along the b direction and the microwave frequency is 9.3845 GHz. (b) Simulated EPR spectrum for V_{Se}^{+}(A). Reproduced from [27] with the permission of AIP Publishing.

39.9%. They both have I = 3/2 nuclear spins and their magnetic moments are $^{69}\mu = +2.0166\ \beta_n$ and $^{71}\mu = +2.5623\ \beta_n$ (where β_n is the nuclear Bohr magneton) [67].

A g value and the hyperfine values for the participating ^{69}Ga and ^{71}Ga nuclei are extracted from the V_{Se}^{+}(A) spectrum in Figure 4.3(a). The two isotopes are treated

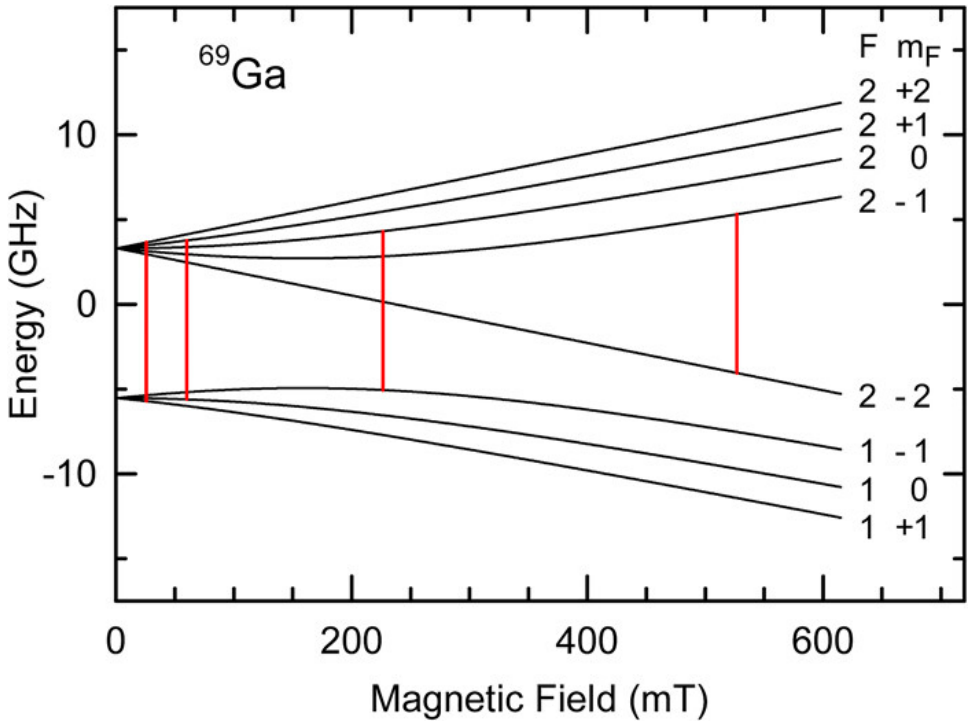

Figure 4.4. Energy levels plotted as a function of magnetic field for the singly ionized V_{Se}^{+}(A) vacancy adjacent to a ^{69}Ga nuclei. The (F, m_F) labeling scheme is used for the spin states and the hyperfine parameter A is assumed to be positive. The red vertical lines represent the four ^{69}Ga transitions observed in the EPR spectrum in Figure 4.3(a). Reproduced from [27] with the permission of AIP Publishing.

separately by using the following spin Hamiltonian with an S = 1/2 electron Zeeman interaction, a large isotropic I = 3/2 hyperfine interaction, and a nuclear Zeeman interaction:

$$H = g\beta \mathbf{S} \cdot \mathbf{B} + A\mathbf{I} \cdot \mathbf{S} - g_n\beta_n \mathbf{I} \cdot \mathbf{B} \tag{4.8}$$

For the V_{Se}^{+}(A) spectrum, the magnitudes of $g\beta B$ and $2A$ are similar. Introducing the raising and lowering operators allows the spin Hamiltonian in Equation 1 to be rewritten as

$$H = g\beta \mathbf{B}\mathbf{S_z} + A\mathbf{I_z}\mathbf{S_z}\frac{1}{2}A(\mathbf{I}_+\mathbf{S}_- + \mathbf{I}_-\mathbf{S}_+) - g_n\beta_n \mathbf{B}\mathbf{I_z} \tag{4.9}$$

The basis states $|M_s, m_I\rangle$, where $M_S = +1/2$ or $-1/2$ and m_I =+3/2, +1/2, 1/2, or 3/2 for each M_S value, are then used to express the spin Hamiltonian as an 8×8 matrix. Diagonalization of this matrix gives the energies of the spin states (i.e., the eigenvalues). The four lines in Figure 4.3(a) from the ^{69}Ga nuclei (at 25.7, 60.2, 226.6, and 526.8 mT) and the microwave frequency of 9.3845 GHz are input data for a least squares fitting program. Positions of these V_{Se}^{+}(A) lines are listed in Table 4.2, along with the experimental positions of lines from the other selenium vacancies. In the fitting routine, the g and A parameters are systematically varied until the predicted line positions match the measured line positions. Table 4.3 contains the resulting "best-fit" values of these ^{69}Ga parameters. For the ^{71}Ga portion of the V_{Se}^{+}(A) spectrum, the two lines in Figure 4.3(a) at 94.2 and 566.8 mT and the 9.3845 GHz microwave frequency are similarly used as input data for the fitting routine, and the results are included in Table 4.3. The same g value is obtained from this second fitting, but the hyperfine value is larger because of the increased nuclear magnetic moment of the ^{71}Ga isotope. In Table 4.3, the ^{71}Ga/^{69}Ga ratio of the hyperfine values for V_{Se}^{+}(A) is 1.2715. This is very close to the known value of 1.2706 for the $^{71}\mu/^{69}\mu$ ratio of the magnetic moments of the two Ga isotopes [67]. To further demonstrate that the correct spin Hamiltonian parameters were determined, the simulated spectrum shown in Figure 4.3(b) was generated with EasySpin [68] using the V_{Se}^{+}(A) parameters in Table 4.3.

The large hyperfine values needed to explain the nearly isotropic V_{Se}^{+}(A) spectrum in Figure 4.3(a) cause a significant mixing of the $|M_s, m_I\rangle$ states at lower magnetic fields. A more appropriate set of quantum numbers are F and m_F and the well-known Breit–Rabi analysis [69–73] of spin states is applicable. Nistor *et al.* [74] have provided a useful description of this approach in their comprehensive review of defects with very large isotropic hyperfine interactions. For $I = 3/2$ nuclei such as ^{69}Ga and ^{71}Ga,

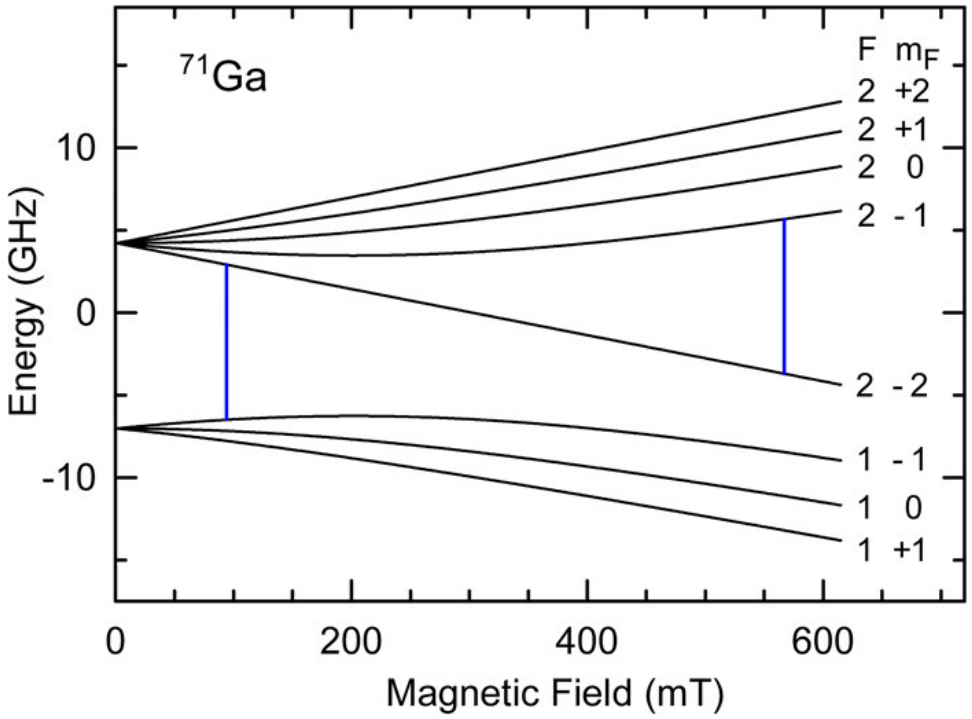

Figure 4.5. Energy levels plotted as a function of magnetic field for the singly ionized V_{Se}^{+}(A) vacancy adjacent to a ^{71}Ga nuclei. The (F, m_F) labeling scheme is used for the spin states and the hyperfine parameter A is assumed to be positive. The blue vertical lines represent the four ^{71}Ga transitions observed in the EPR spectrum in Figure 4.3(a). Reproduced from [27] with the permission of AIP Publishing.

F has values of 1 or 2 ($F = I \pm 1/2$) and m_F has values of F, $F-1$, ..., $-F$ for each value of F. Figure 4.4 shows the eight energy levels (in units of GHz) as a function of magnetic field for the ^{69}Ga portion of V_{Se}^{+}(A). These curves were generated using the parameters in Table 4.3. The (F,m_F) labeling scheme for the spin states is used and the four transitions observed in the EPR spectrum are shown as vertical lines (the lengths of these lines correspond to the microwave frequency). For each transition, the selection rule is $\Delta m_F = \pm 1$. Figure 4.5 shows the eight energy levels as a function of magnetic field for the ^{71}Ga nuclei (generated using parameters from Table 4.3). The two vertical lines in this latter figure illustrate the transitions observed for the ^{71}Ga isotope. Again, the selection rule is $\Delta m_F = \pm 1$. Note that the zero-field splitting in Figures 4.4 and 4.5, while different, are both equal to $2A$ (i.e., two times the hyperfine

parameter for the respective isotope).

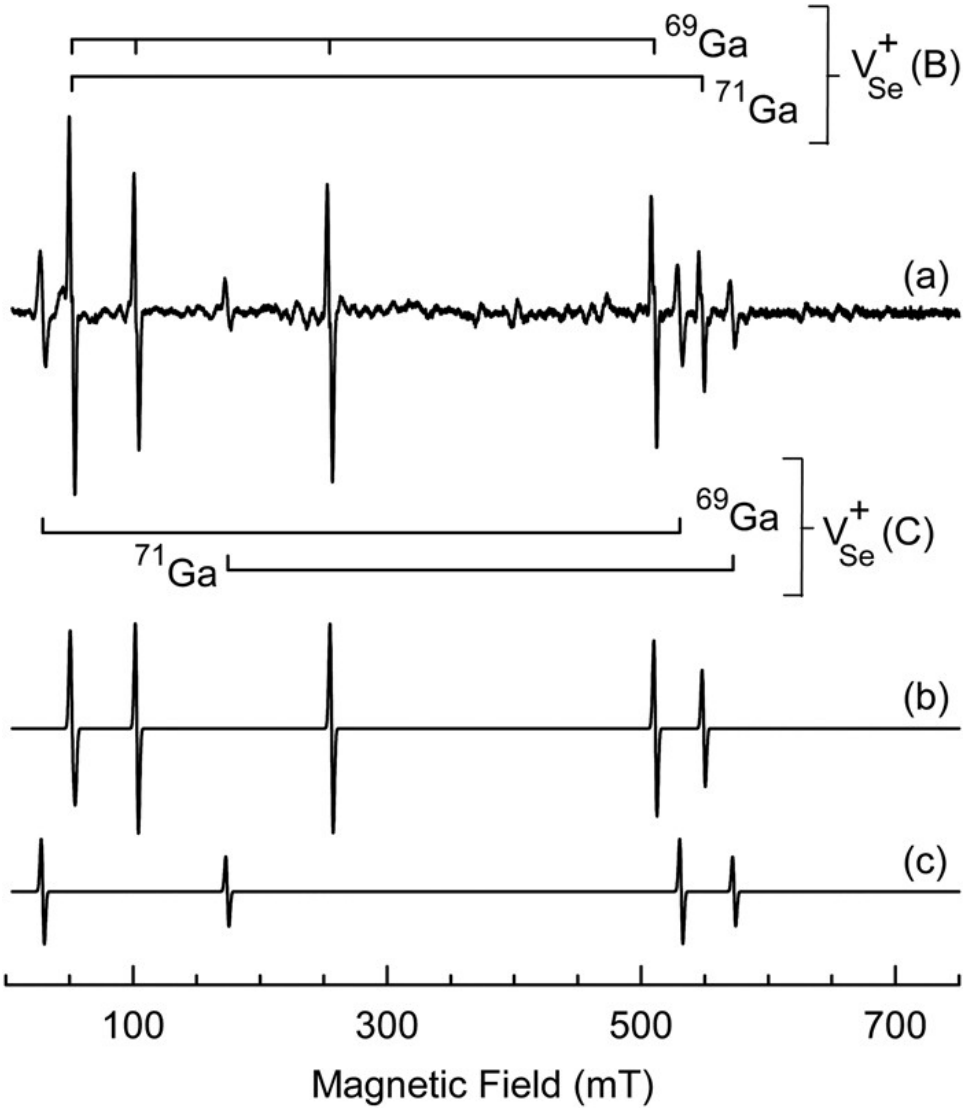

Figure 4.6. (a) Photoinduced EPR spectrum taken at 35 K from $BaGa_4Se_7$ crystal sample 5Y1. The crystal was initially exposed at 35 K to 532 nm laser light. After removing the light, the crystal was warmed to 90 K for 1 min and then returned to 35 K for measurement. The "before light" spectrum in Figure 4.2(a) has been subtracted. Two singly ionized selenium vacancies, V_{Se}^{+}(B) and V_{Se}^{+}(C), are present. The magnetic field is along the b direction and the microwave frequency is 9.3845 GHz. (b) Simulated EPR spectrum for V_{Se}^{+}(B). (c) Simulated EPR spectrum for V_{Se}^{+}(C). Reproduced from [27] with the permission of AIP Publishing.

Although the ^{69}Ga and ^{71}Ga nuclei have similar properties (both are $I = 3/2$ nuclei and their nuclear magnetic moments are similar), the contributions of the two isotopes to the V_{Se}^{+}(A) spectrum in Figure 4.3(a) are quite different. There are four

	V_{Se}^{+}(A)		V_{Se}^{+}(B)		V_{Se}^{+}(C)		V_{Se}^{+}(D)	
Transition	^{69}Ga	^{71}Ga	^{69}Ga	^{71}Ga	^{69}Ga	^{71}Ga	^{69}Ga	^{71}Ga
(2,-2) to (2,-1)	526.8	566.8	510.3	548.0	530.5	572.2	497.8	533.4
(1,-1) to (2,0)	226.6	...	255.1	...	...	...	317.8	264.8
(1,0) to (2,+1)	60.2	...	102.3	...	...	...	198.7	36.1
(1,+1) to (2,+2)	25.7	...	52.1	...	...	...	112.9	...
(1,-1) to (2,-2)	...	94.2	...	52.1	28.9	174.5	...	...

Table 4.2. Magnetic field positions of lines in the EPR spectra of selenium vacancies. These data were obtained from the experimental spectra shown in Figures 4.3, 4.6, and 4.7. The (F,mF) labeling scheme is used to describe the transitions. Units are mT. Reproduced from [27] with the permission of AIP Publishing.

	Spin Hamiltonian parameters		
Defect	g value	A(^{69}Ga)	A(^{71}Ga)
V_{Se}^{+}(A)	2.000	4417 Mhz	5616 Mhz
V_{Se}^{+}(B)	2.024	4123 Mhz	5224 Mhz
V_{Se}^{+}(C)	2.061	4998 Mhz	6356 Mhz
V_{Se}^{+}(D)	1.951	3330 Mhz	4250 Mhz

Table 4.3. "Best-fit" spin Hamiltonian parameters for singly ionized selenium vacancies in $BaGa_4Se_7$ crystals. Line positions used in the fittings are listed in Table II (they were obtained from the EPR spectra shown in Figures 4.3, 4.6, and 4.7). Units for the hyperfine values are MHz. Estimates of uncertainties are ± 0.005 for the g values and ±40 MHz for the A values. Reproduced from [27] with the permission of AIP Publishing.

lines from the ^{69}Ga nuclei and only two lines from the ^{71}Ga nuclei. The reason for this difference becomes obvious when the microwave frequency (9.3845 GHz) is compared to the $2A$ hyperfine values for ^{69}Ga and ^{71}Ga in Table 4.3 (8.834 and 11.232 GHz, respectively). The microwave frequency is greater than $2A$ for the ^{69}Ga nuclei and less than $2A$ for the ^{71}Ga nuclei. Using the (F, m_F) labels and referring to Figures 4.4 and 4.5, the (1,-1) to (2,-2) transition is only seen when the microwave frequency is less than the zero-field splitting value of $2A$. In contrast, the (1,+1) to (2,+2), the (1,0) to (2,+1), and the (1,-1) to (2,0) transitions are only seen when the microwave frequency is greater than the zero-field splitting value of $2A$. The (2,-2) to (2,-1) transition is seen under all conditions.

After the EPR data in Figure 4.3(a) were taken, the 532 nm laser light was removed, and the crystal was briefly warmed to 90 K (for 1 min) while remaining in the microwave cavity with the magnetic field along the b direction. The temperature was quickly returned to 35 K and the EPR data shown in Figure 4.6(a) were obtained with no further exposure to laser light. Figure 4.6(a) is the "difference" spectrum obtained by subtracting the "before light" spectrum in Figure 4.2(a) from the spectrum taken after heating to 90 K. Comparing the spectra in Figures 4.3(a) and 4.6(a) shows that the heating to 90 K caused significant changes in the selenium vacancies. The trapped hole and V_{Se}^{+}(A) spectra are no longer present, the concentration of V_{Se}^{+}(B) increased by a factor of two (to 1.9×10^{18} cm^{-3}), and a new selenium vacancy, labeled V_{Se}^{+}(C), appeared with a concentration of 0.8×10^{18} cm^{-3}. Magnetic field positions for the V_{Se}^{+}(B) and V_{Se}^{+}(C) EPR lines in Figure 4.6(a) are included in Table 4.2. Using these magnetic field values and the 9.3845 GHz microwave frequency, the g and hyperfine parameters for V_{Se}^{+}(B) and V_{Se}^{+}(C) were determined by the same fitting procedure used for V_{Se}^{+}(A). The results are presented in Table 4.3. The simulated spectra for V_{Se}^{+}(B) and V_{Se}^{+}(C) shown in Figures 4.6(b) and 4.6(c), respectively, were generated with EasySpin [68] using the parameters in Table 4.3. Next, the $BaGa_4Se_7$ crystal was warmed to 120 K without illumination, held at this temperature for 1 min, and then returned to 35 K for measurement. Figure 4.7(a) shows EPR data taken with the magnetic field along the b direction. The "difference" spectrum in Figure 4.7(a) was obtained by subtracting the initial "before light" spectrum in Figure 4.2(a) from the spectrum taken after heating to 120 K. This second heating step introduced further changes in the selenium vacancies. The V_{Se}^{+}(C) spectrum disappeared and the concentration of V_{Se}^{+}(B) increased to 2.3×10^{18} cm^{-3}. A fourth selenium vacancy, labeled V_{Se}^{+}(D), appeared with a concentration of 1.4×10^{18} cm^{-3}. The combined increase in the number of V_{Se}^{+}(B) and V_{Se}^{+}(D) vacancies at 120 K is more than the

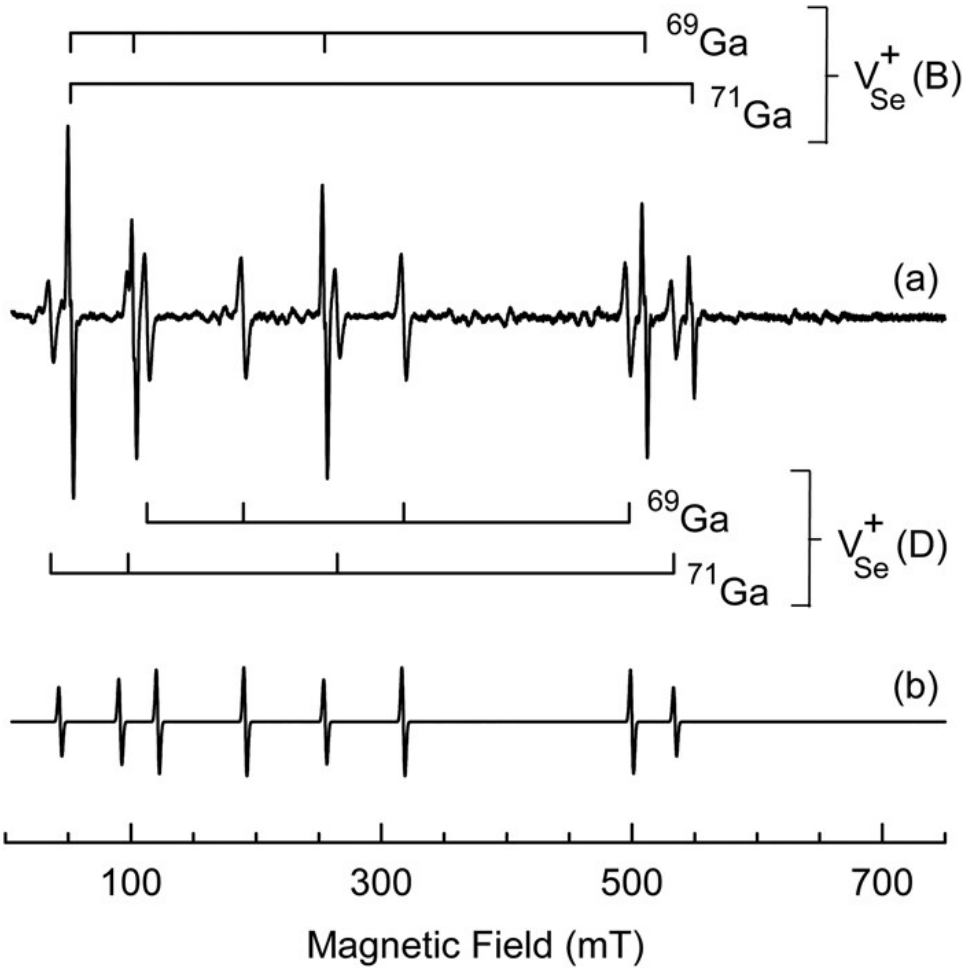

Figure 4.7. (a) Photoinduced EPR spectrum taken at 35 K from $BaGa_4Se_7$ crystal sample 5Y1. The crystal was initially exposed at 35 K to 532 nm laser light. After taking the spectrum in Figure 4.6(a), the crystal was warmed to 120 K for 1 min and then returned to 35 K for measurement. The "before light" spectrum in Figure 4.2(a) has been subtracted. Two singly ionized selenium vacancies, V_{Se}^{+}(B) and V_{Se}^{+}(D), are present. The magnetic field is along the b direction and the microwave frequency is 9.3845 GHz. (b) Simulated EPR spectrum for V_{Se}^{+}(D). Reproduced from [27] with the permission of AIP Publishing.

decrease in the number of V_{Se}^{+}(C) vacancies. This suggests that unseen defects release electrons at this temperature, which then become trapped at selenium vacancies. Table 4.2 contains the magnetic field positions for the V_{Se}^{+}(D) EPR lines in Figure 4.7(a). Using these field values and a microwave frequency of 9.3845 GHz, the g and hyperfine parameters for V_{Se}^{+}(D) were determined in the same manner as for the other three selenium vacancies, and the results are included in Table 4.3. The simulated

spectrum for V_{Se}^{+}(D), shown in Figure 4.7(b), was generated with EasySpin [68] using the parameters in Table 4.3.

Information about the thermal stability of the observed singly ionized selenium vacancies is provided by the data in Figures 4.3, 4.6, and 4.7. The dominant selenium vacancy, V_{Se}^{+}(A), thermally decays below 90 K, V_{Se}^{+}(C) thermally decays between 90 and 120 K, and V_{Se}^{+}(B) and V_{Se}^{+}(D) are stable above 120 K, but not at room temperature. As the V_{Se}^{+}(A) vacancies thermally decay during the warming step to 90 K, the V_{Se}^{+}(B) and V_{Se}^{+}(C) vacancies grow, thus indicating that a portion of the electrons released from the less stable V_{Se}^{+}(A) vacancies move within the crystal and form the more stable singly ionized vacancies. In separate experiments, we found that the V_{Se}^{+}(A) vacancies produced at 35 K by the 532 nm laser light can be destroyed at this temperature with 633 nm laser light. The other three photoinduced selenium vacancies observed at low temperature can also be destroyed with the 633 nm light. In contrast, 1064 nm laser light has little effect on the singly ionized selenium vacancies. After the photoinduced singly ionized charge states are eliminated either by warming or optical bleaching, the selenium vacancies remain in the crystal but are no longer seen with EPR (i.e., they have reverted to a nonparamagnetic charge state).

Additional support for selenium vacancies being a primary defect in $BaGa_4Se_7$ crystals is found in the literature. Our results are consistent with several reports that suggest post-growth annealing in a Se-containing atmosphere improves crystal quality and reduces point defects. Guo *et al.* [59]. significantly improved the transmittance of crystals at longer wavelengths by thermal annealing under an atmosphere of $BaGa_4Se_7$ powder vapor. Yelisseyev *et al.* [64] showed that annealing $BaGa_4Se_7$ crystals in a BaSe atmosphere greatly reduced the dominant photoluminescence (PL) band at 694 nm (1.785 eV). This latter result, when combined with our present EPR results, leads us to suggest that the 694 nm PL band, observed at 80 K, may be associated with

singly ionized selenium vacancies. Yelisseyev *et al.* [64] tentatively attributed this PL band to a barium vacancy (V_{Ba}) or a gallium-on-barium antisite (Ga_{Ba}) defect.

4.4.2 EPR spectra present in as-grown $BaGa_4Se_7$ crystals

The EPR spectrum obtained from the $BaGa_4Se_7$ crystal prior to exposure to laser light is shown in Figure 4.8(a) (this is the "before light" spectrum shown earlier in Figure 4.2). This spectrum was recorded at 35 K, with the magnetic field aligned along the b direction and a microwave frequency of 9.3845 GHz. Two sets of closely spaced lines near 75 and 200 mT are present in Figure 4.8(a) and are tentatively assigned to Mn^{3+} (3d4) ions [75–77]. The set of lines near 75 mT shows an approximate 7 mT hyperfine splitting from the ^{55}Mn nucleus (I = 5/2, 100% abundant) and an additional smaller 2 mT superhyperfine splitting due to ^{69,71}Ga nuclei located at one adjacent Ga site. Although not shown, an additional set of lines from the Mn^{3+} ions is present at high field, near 890 mT, when the magnetic field is along the b direction. The Mn^{3+} ions in $BaGa_4Se_7$ occupy a Ga^{3+} site and are not affected by the 532 nm laser light.

Nearly all the EPR lines in Figure 4.8(a), except those due to Mn^{3+}, are associated with one intrinsic defect. These lines, extending from 20 to 700 mT, are caused by large and unequal, nearly isotropic, hyperfine interactions of an unpaired electron with ^{69}Ga and ^{71}Ga nuclei at two regular lattice sites. The responsible defect is a singly ionized selenium vacancy and is labeled V_{Se}^{+}(E). This defect is stable at room temperature and is observed in the as-grown $BaGa_4Se_7$ crystals before exposure to 532 nm laser light. Unlike the selenium vacancies in Section 4A that interact primarily with one Ga neighbor, V_{Se}^{+}(E) shares its unpaired spin unequally with two Ga neighbors (approximately 65.6% of the spin is on one neighbor and 34.4% is on the other neighbor). This explains the larger number of lines in the spectrum. A

lack of angular dependence for V_{Se}^{+}(E) indicates that the unpaired spin occupies $4s^1$ orbitals on the two adjacent Ga ions. The V_{Se}^{+}(E) EPR spectrum is described by the following spin Hamiltonian with $S = 1/2$, $I_1 = 3/2$, and $I_2 = 3/2$:

$$H = g\beta \mathbf{S} \cdot \mathbf{B} + A_1 \mathbf{I_1} \cdot \mathbf{S} + A_2 \mathbf{I_2} \cdot \mathbf{S} - g_n \beta_n \mathbf{I_1} \cdot \mathbf{B} - g_n \beta_n \mathbf{I_2} \cdot \mathbf{B} \tag{4.10}$$

Electron Zeeman, hyperfine, and nuclear Zeeman terms are included. Subscripts 1 and 2 refer to the neighboring Ga sites with the larger and the smaller hyperfine interactions, respectively.

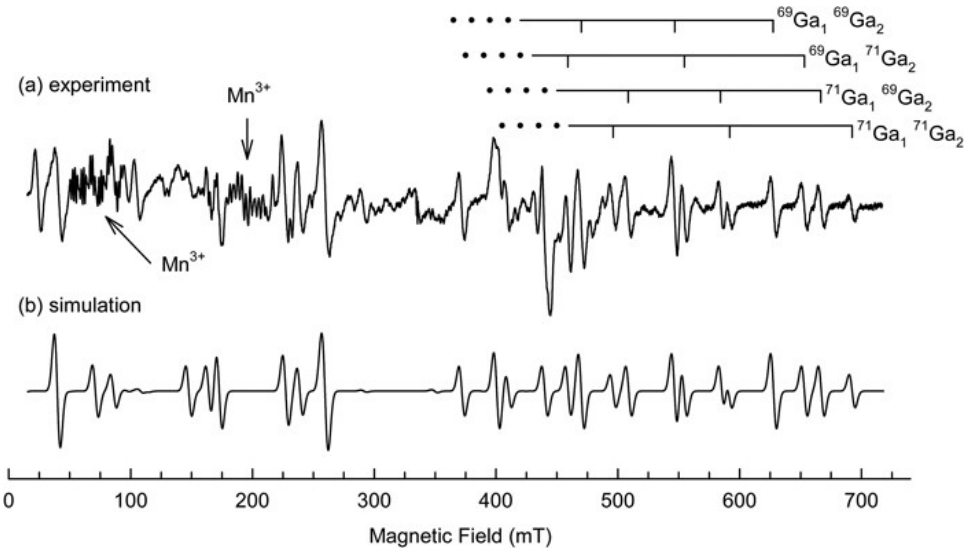

Figure 4.8. EPR spectrum taken at 35 K before exposing $BaGa_4Se_7$ crystal sample 5Y1 to laser light. The magnetic field is along the b direction. (a) Experimental spectrum. (b) Simulated spectrum generated using EasySpin. Stick diagrams above the experimental spectrum identify hyperfine lines associated with the different combinations of ^{69}Ga and ^{71}Ga nuclei. Reproduced from [27] with the permission of AIP Publishing.

The V_{Se}^{+}(E) spectrum in Figure 4.8(a) consists of four superimposed groups of lines, each representing a different distribution of the ^{69}Ga and ^{71}Ga nuclei among the two participating Ga sites. Relative line intensities are determined by the natural abundances of the two isotopes. For 36.1% of the V_{Se}^{+}(E) vacancies, both Ga sites

have a ^{69}Ga nucleus. For 24% of the vacancies, site 1 has a ^{69}Ga nucleus and site 2 has a ^{71}Ga nucleus. Similarly, for another 24%, site 1 has a ^{71}Ga nucleus and site 2 has a ^{69}Ga nucleus. For the remaining 15.9%, both sites have a ^{71}Ga nucleus. Stick diagrams above the high field lines in Figure 4.8(a) illustrate the contributions from the different combinations of isotopes. The numerical fitting capability in the EasySpin simulation program [68] was used to extract values for g, A1, and A2 from the nearly isotropic experimental spectrum. These results are listed in Table 4.4. Figure 4.8(b) shows the simulated spectrum generated with these parameters. There is good agreement between the experimental and the simulated spectra.

		Hyperfine Parameters (MHz)			
		A_1(Ga site 1)		A_2(Ga site 2)	
Selenium vacancy	g value	^{69}Ga	^{71}Ga	^{69}Ga	^{71}Ga
V_{Se}^{+}(E)	2.013	4326	5496	2269	2883

Table 4.4. Spin Hamiltonian hyperfine parameters forV_{Se}^{+}(E) in $BaGa_4Se_7$. Values for these parameters were obtained by using EasySpin to fit the experimental spectrum in Figure 4.8(a). Estimates of uncertainties are ±0.005 for the g values and ±40 MHz for the hyperfine values. Reproduced from [27] with the permission of AIP Publishing.

4.4.3 Holes trapped by cation vacancies

As shown in Figure 4.3(a), a broad EPR line near 329 mT is formed when the $BaGa_4Se_7$ crystal is exposed to 532 nm laser light while being held at 35 K. With the magnetic field along the b direction, the width of the line is approximately 7.0 mT and its g value is 2.037. The g value of this $S = 1/2$ defect varies from 2.030 to 2.065 for other directions of the magnetic field. These small positive g shifts suggest that the responsible defect is a cation vacancy with an unpaired spin localized on one of the adjacent selenium ions. A Se^{2-} ion loses an electron and becomes a Se^{-} ion with a $4p^5$ valence shell. The effective negative charge of the cation vacancy stabilizes the

hole (i.e., the missing electron) on the selenium ion, thus forming a stable defect at a sufficiently low temperature. Similar defects, referred to as acceptor-bound small polarons, have been widely studied in oxide crystals [78–82]. Trapped-hole centers of this type usually have broad optical absorption bands peaking in the near-infrared with small oscillator strengths [78].

The large 7 mT width of the trapped hole's EPR signal is a result of unresolved hyperfine interactions with ^{69}Ga and ^{71}Ga nuclei adjacent to the Se ion with the hole. Because of the lack of hyperfine information, we cannot say with certainty which vacancy, Ba^{2+} or Ga^{3+}, is responsible for stabilizing the hole on the selenium ion. However, a plausible argument can be made that we are seeing holes trapped by Ba^{2+} vacancies. The low thermal decay temperature (near 70 K) of the trapped hole is the critical information. The electrostatic binding energy, which is reflective of the activation energy for release of the hole, is expected to be smaller for the Ba^{2+} vacancy than for the Ga^{3+} vacancy. This expectation is based on the smaller effective negative charge (2) of the doubly ionized Ba vacancy (V_{Ba}^{2-}) and the greater separation distance between the Se and Ba ions. For perspective, a hole trapped on an oxygen ion adjacent to a Ga vacancy in $LiGaO_2$ crystals is thermally stable at room temperature for more than one year [79]. A hole localized on one oxygen ion next to a Ga vacancy in β-Ga_2O_3 crystals is also stable at room temperature [80].

4.4.4 Optical absorption results

Polarized optical absorption spectra were taken from the as-grown $BaGa_4Se_7$ crystal. The light propagated along the a direction and the optical path length was 2.45 mm. The shift of the band edge with temperature is shown in Figure 4.9. At room temperature (296 K), the absorption edge occurs near 470 nm with a small shift to longer wavelength when the light is polarized E$\|$b rather than E$\|$c*. Cooling the

crystal to 80 K shifts the band edge to near 430 nm and reduces the energy separation between the absorption edges for E||b and E||c*. A defect-related absorption feature near 450 nm in the 80 K data shows a polarization preference for E||c*.

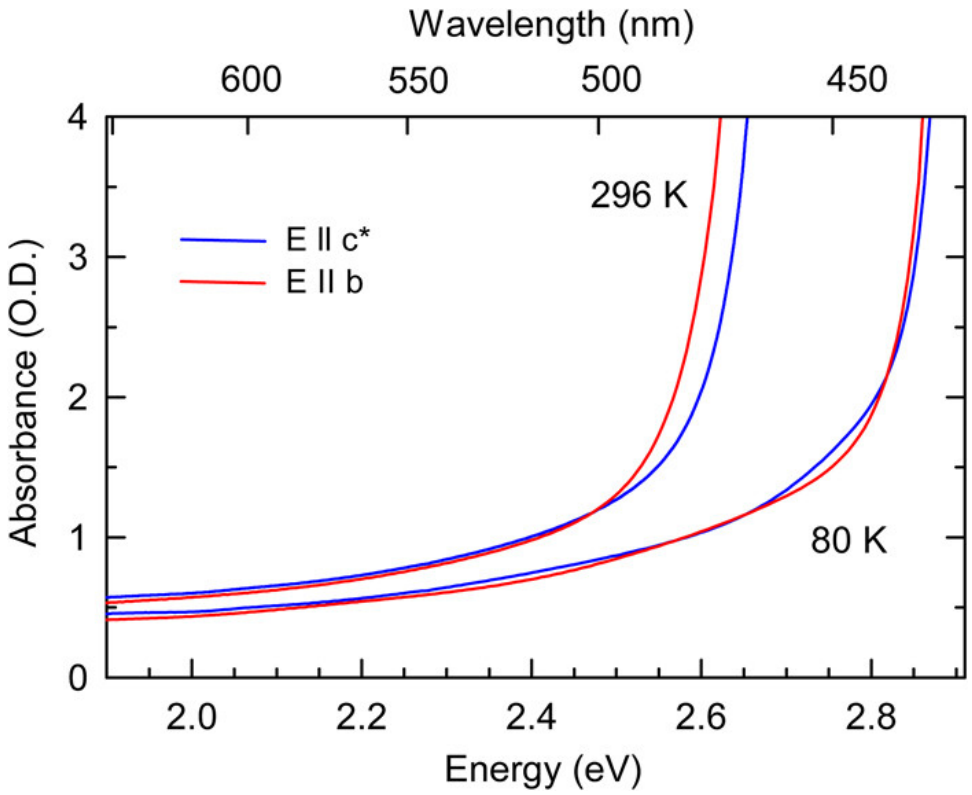

Figure 4.9. Optical absorption spectra taken at 296 and 80 K from the as-grown $BaGa_4Se_7$ crystal sample 5Y1. The light propagates along the a direction with E||b (red) and E||c* (blue). The optical path length is 2.45 mm. Reproduced from [27] with the permission of AIP Publishing.

Exposing the $BaGa_4Se_7$ crystal to 532 nm laser light while at 80 K introduced broad optical absorption bands covering the visible region and extending slightly into the near-infrared. Figure 4.10 shows the polarized absorption spectra obtained before the 532 nm illumination and immediately after removing the 532 nm light. Figures 4.10(a) and 4.10(b) are the spectra taken with E||b and with E||c*, respectively. These photoinduced absorption features thermally decayed within an hour when the crystal was left in the dark at 80 K. In contrast, applying 633 nm laser light at 80 K quickly destroyed (in a few seconds) nearly all the absorption that had been produced by the

532 nm light. The spectra taken after the exposure to the 633 nm light are also shown in Figure 4.10. Figure 4.11 shows absorption bands induced at 80 K by the 532 nm

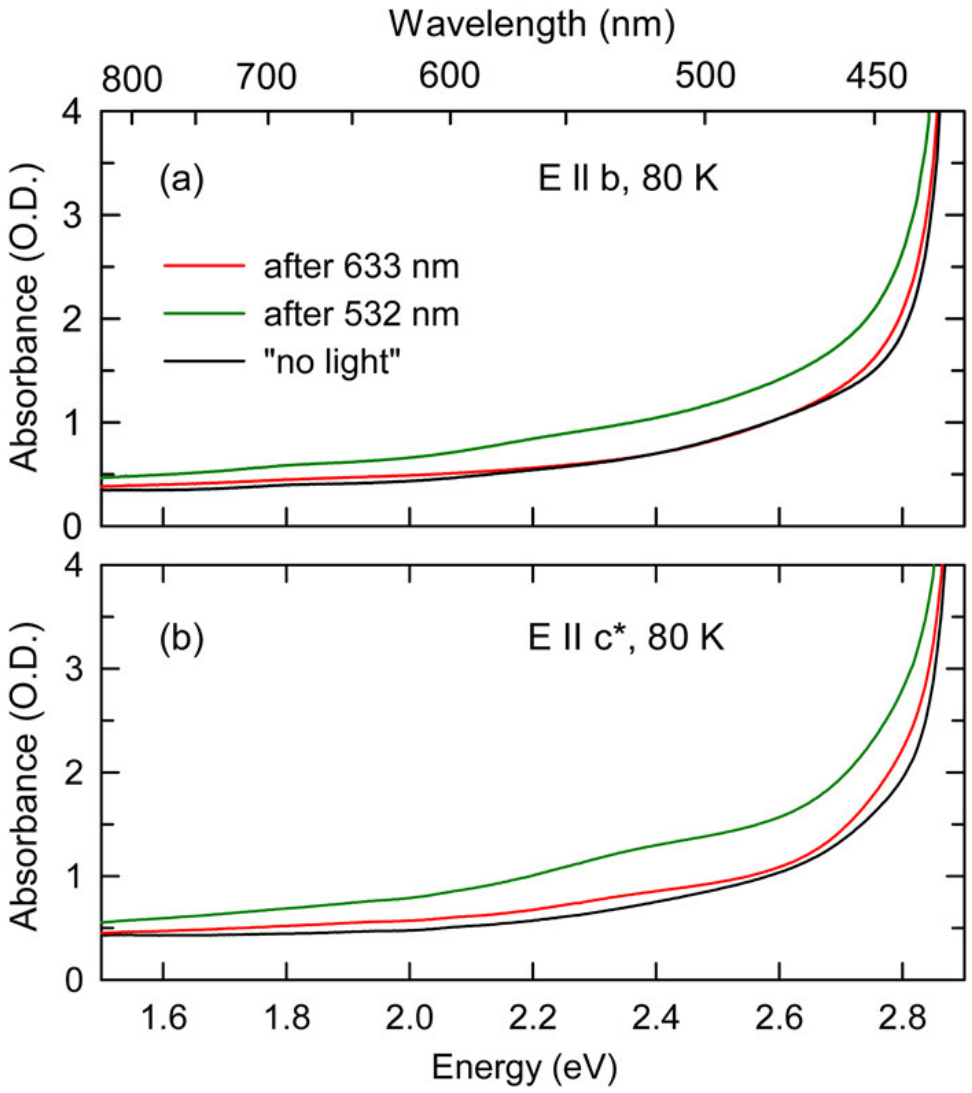

Figure 4.10. Optical absorption spectra taken at 80 K from $BaGa_4Se_7$ crystal sample 5Y1. Light propagates along the a direction with (a) E‖b and (b) E‖c*. Spectra were taken before exposure to laser light (black), after exposure to 532 nm laser light (green), and after exposure to 633 nm laser light (red). Reproduced from [27] with the permission of AIP Publishing.

light. The two curves in this figure are difference spectra where the "before 532 nm light" spectrum has been subtracted from the "after 532 nm light" spectrum. Bands peaking near 520 nm (E‖c*), 530 nm (E‖b), and 710 nm (both polarizations) are present. Additional photoinduced absorption extends beyond 440 nm on the short

wavelength side and to near 1.2 µm on the long wavelength side. We suggest that the bands in the 520–530 nm region are intracenter transitions of the singly ionized selenium vacancies observed with EPR and the band near 710 nm is caused, in part, by the holes trapped at barium vacancies (i.e., the small polarons described in Section 4.4.3). The optical absorption bands and the EPR spectra are both produced by the 532 nm laser light, and they are both destroyed by the 633 nm laser light. Attributing an optical absorption band to a specific selenium vacancy EPR spectrum, however, must await more detailed studies of a larger set of $BaGa_4Se_7$ crystals grown under varying conditions and subjected to post-growth treatments.

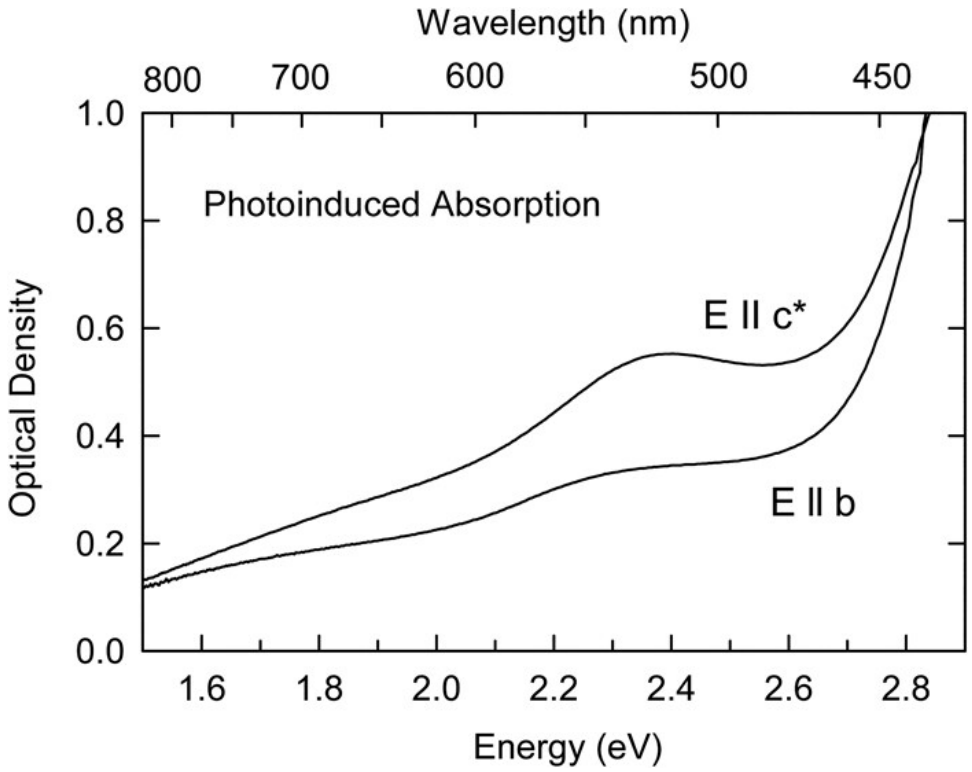

Figure 4.11. Difference curves obtained from the 80 K spectra in Figure 4.10. The spectrum taken before exposure to 532 nm light has been subtracted from the spectrum taken after exposure to 532 nm light. Light propagated along the a direction and was polarized either E‖b and E‖c*. Absorption bands in the 520–530 and 710 nm regions, as well as near the band edge, are produced by the 532 nm laser light. Reproduced from [27] with the permission of AIP Publishing.

4.4.5 Summary

Electron paramagnetic resonance (EPR) has been used to identify and characterize singly ionized selenium vacancies (V_{Se}^{+}) in $BaGa_4Se_7$ crystals. The doubly ionized selenium vacancies (V_{Se}^{2+}) initially present in as-grown crystals are converted to their optically active paramagnetic charge state with 532 nm laser light. Five EPR spectra are observed, each representing a different vacancy site among the seven inequivalent sites in this monoclinic crystal and each showing large ^{69}Ga and ^{71}Ga hyperfine interactions. Holes localized on a selenium ion next to a cation vacancy, most likely a Ba^{2+} vacancy, are also seen with EPR. Optical absorption bands in the visible and near-infrared regions are produced at 80 K with 532 nm light. These bands, attributed to singly ionized selenium and barium vacancies, are expected to contribute to two-photon absorption and also direct one-photon absorption when an OPO is pumped near 1 µm. We suggest that post-growth annealing in a Se atmosphere may remove these vacancies and improve the performance of $BaGa_4Se_7$ crystals.

5. Correlation of EPR V_{Se}^{+}(E) with Optical Absorption

5.1 Abstract

BAE Systems (Nashua, NH) provided six $BaGa_4Se_7$ samples for investigation from two separate growth runs [3]. Variations between the two growth runs arise due to unspecified differences of the operating parameters during growth. It is assumed that there is no variation in the starting materials, powders, or seed crystals. Three $BaGa_4Se_7$ samples were from growth run 2 (with samples labeled by the number 2 followed by a two-digit alpha-numeric code), and the remaining three were from growth run 5 (with samples labeled by the number 5 followed by a two-digit alpha-numeric code). All the EPR and optical absorption data presented in chapter 4 were obtained from a fifth growth run $BaGa_4Se_7$ sample. Similar EPR and optical absorption characteristics were observed within all three $BaGa_4Se_7$ samples from the fifth growth run. EPR and optical absorption data from $BaGa_4Se_7$ of the second growth run varied distinctly from the fifth growth run samples. No EPR spectra signifying the presence of selenium vacancies (V_{Se}^{+}) were observed in any of the samples from the second growth run under any conditions. In chapter 4 five distinct selenium vacancy EPR spectra were presented. Of the five selenium vacancy spectra, only V_{Se}^{+}(E) was present at room temperature prior to exposure to 532 nm light. This feature was replicated across $BaGa_4Se_7$ samples from the fifth growth run. The V_{Se}^{+}(E) EPR spectrum was eliminated in all fifth growth run samples by exposing the crystal to 633 nm light.

Having samples from two separate growth runs, with vastly different room temperature EPR spectra presents an opportunity to investigate the room temperature optical absorption across both $BaGa_4Se_7$ growth runs and correlate the absorption to the V_{Se}^{+}(E) selenium vacancy. Room temperature optical absorption experiments

were conducted between two samples, one from each growth run, in support of this correlation effort.

5.2 Experimental Details

A Cary 5000 spectrophotometer was used to conduct room temperature optical absorption measurements with $BaGa_4Se_7$ samples from growth runs two and five. These samples were stored in a lab at ambient temperatures and exposed to white light during normal laboratory proceedings. The spectrophotometer was set to double-beam mode with the sample placed in the optical path using the quartz halogen light source. A wire-grid polarizer from Thorlabs (Model WP25M-UB) was used to allow for absorption measurements when the light was polarized in the E‖b and E‖c* directions of the crystal. A series of three absorption measurements were taken for each polarization direction: before exposure to laser light, after exposure to 532 nm laser light, and after exposure to 633 nm laser light. The polarizer was set to E‖b orientation and "dark" absorption measurements were taken. The sample was then exposed to 532 nm light for two minutes before optical absorption measurements were taken. Lastly the sample was exposed to 633 nm light, again for two minutes, and absorption measurements were taken. The polarizer was then rotated 90 degrees and the series of three optical absorption measurements repeated with the electric field now E‖c*. This experiment was repeated multiple times with 24 to 48 hours between the last 633 nm exposure of one experimental run and the "dark" optical absorption measure of the next experimental run.

5.3 Optical Absorption Results

Figure 5.1 shows the optical absorption results from the three room temperature scans with the polarizer set to the E‖b orientation. The black line corresponds to

the "dark" measurement, while the green and red lines correspond to measurements taken after two-minute exposure to 532 nm and 633 nm laser light respectively.

The first notable feature is that the absorption edge occurs near 470 nm, which corresponds to and energy of 2.63 eV. Exposing the crystal to 532 nm light induces a broad absorption band that peaks near 575 nm. Lastly, exposure to 633 nm light reduces the absorption spectrum below that of the "dark" absorption spectrum.

This reduction in optical absorption after exposure to 633 nm light, that is below that of the "dark" measurement, implies that the samples in the "dark" state have optically active defects that are generated from exposure to laboratory room lights at room temperature. In figure 5.1 this difference is measured as two tenths of an *OD* at 550 nm and suggests that $BaGa_4Se_7$ samples should be stored such that they are not exposed to room light to minimize the induced absorption. This result also yields information as to the depth of the electron trap. Given that there is ambient light induced absorption, the depth of this electron trap is shallow in relation to the top of the valence band. Room light optically excites electrons from the valence band to the doubly ionized selenium vacancies converting nonparamagnetic V_{Se}^{2+} vacancies to paramagnetic V_{Se}^{+} vacancies.

The absorption mechanism brought about by exposure to 532 nm light is removed when the crystal is exposed to 633 nm light. The blue curve in figure 5.3 is a subtraction of 633 nm absorption spectra from the "dark" absorption spectra and represents the absorption mechanism present in the as-grown $BaGa_4Se_7$ crystals when the light was polarized parallel to the b axis of the crystal. Similar behavior is shown when the light is polarized in the E$\|$c* orientation as shown in figures 5.2 and 5.3. The orange curve in 5.3 is a subtraction of 633 nm absorption spectra from the "dark" absorption spectra and represents the absorption mechanism present in the as-grown $BaGa_4Se_7$ crystals when the light was polarized parallel to the c^* axis of the crystal.

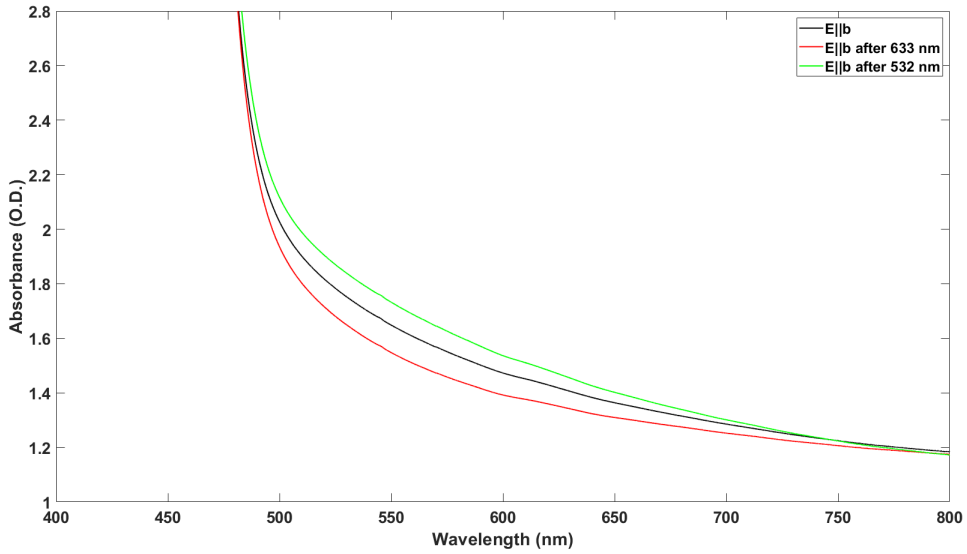

Figure 5.1. Optical absorption from $BaGa_4Se_7$ sample 5Y1 (fifth growth run) with E‖b. The black, green, and red curves show the optical absorption before exposure to light, post 2 minute exposure to 532 nm light, and post exposure to 633 nm light respectively.

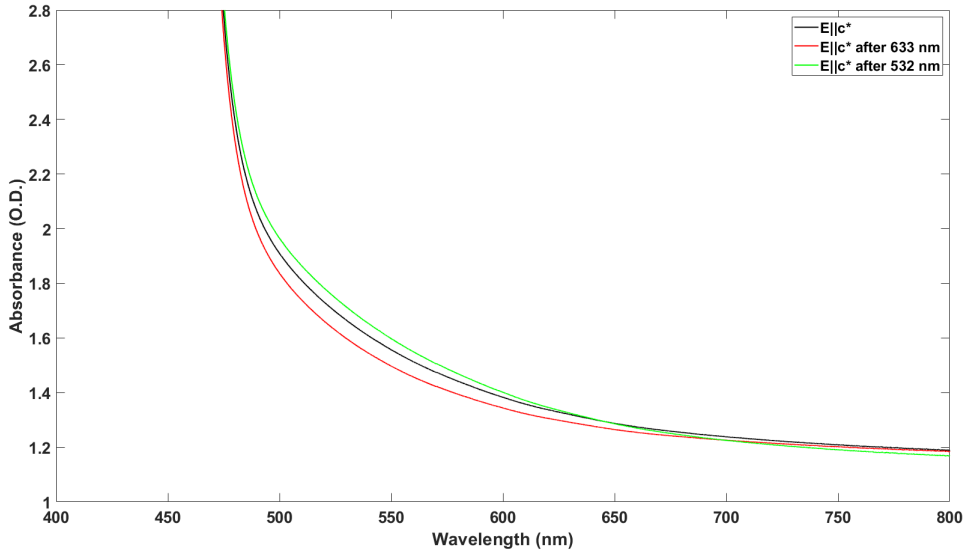

Figure 5.2. Optical absorption from $BaGa_4Se_7$ sample 5Y1 (fifth growth run) with E‖c*. The black, green, and red curves show the optical absorption before exposure to light, post 2 minute exposure to 532 nm light, and post exposure to 633 nm light respectively.

Figures 5.1 and 5.2 show a shift in the band-edge to shorter wavelengths when the light is polarized E||c*. The photo-induced optical absorption is quantified by subtracting the post 633 nm absorption spectra from the before light spectra. A broad photo-induced absorption band peaking near 2.4 eV is observed.

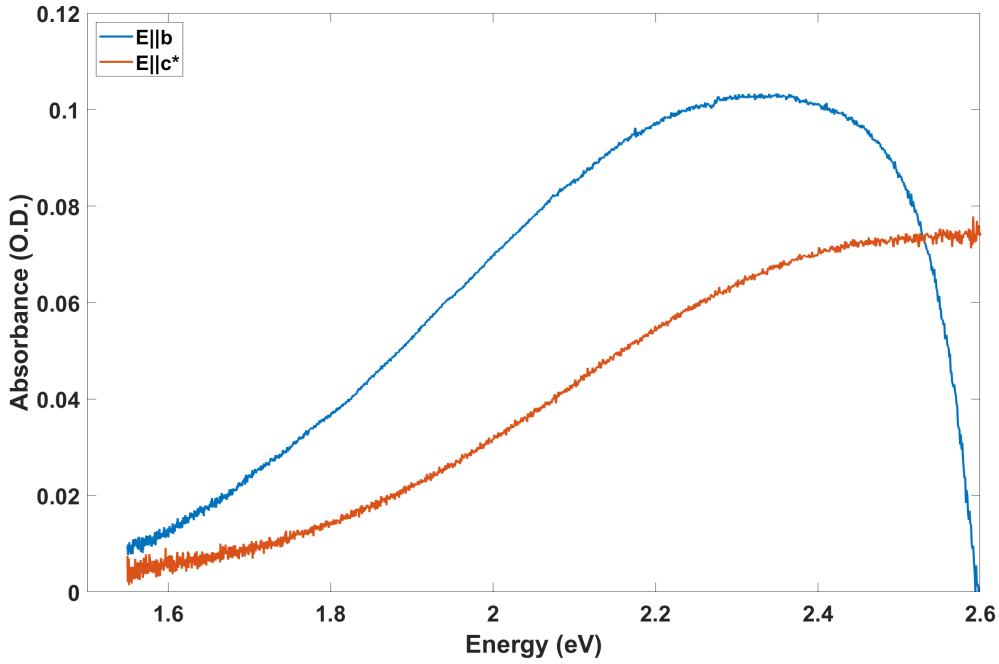

Figure 5.3. Photo-induced optical absorption from $BaGa_4Se_7$ sample 5Y1 (fifth growth run). The 633 nm absorption spectra has been subtracted from the before light spectra.

$BaGa_4Se_7$ samples from the second growth run did not show any selenium vacancy EPR spectra under any condition and, as anticipated, the optical absorption spectra showed less pronounced effects when exposed to 532 or 633 nm light. A similar series of room temperature optical absorption scans were taken with sample 2Y1 from the second growth run.

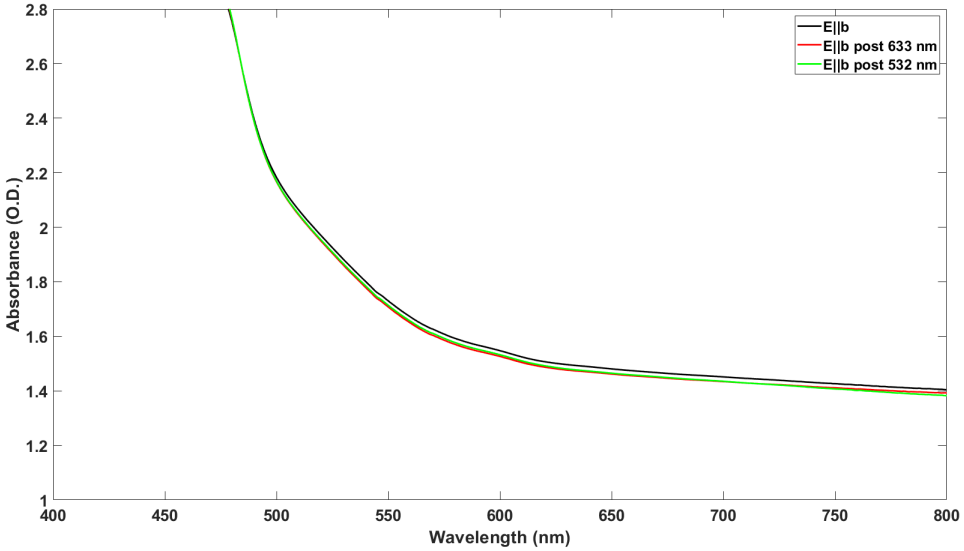

Figure 5.4. Optical absorption from $BaGa_4Se_7$ sample 2Y1 (second growth run) with E‖b. The black, green, and red curves show the optical absorption before exposure to light, post 2 minute exposure to 532 nm light, and post exposure to 633 nm light respectively.

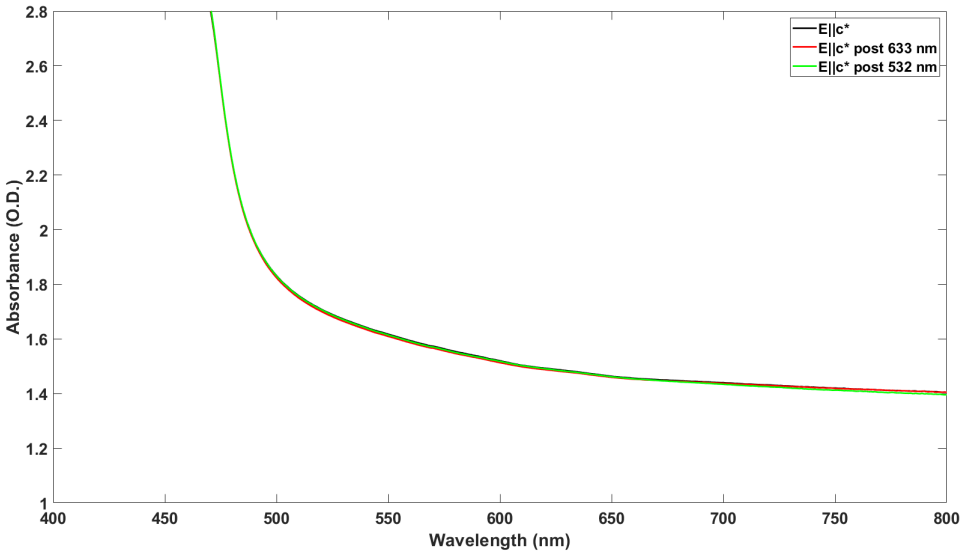

Figure 5.5. Optical absorption from $BaGa_4Se_7$ sample 2Y1 (second growth run) with E‖c*. The black, green, and red curves show the optical absorption before exposure to light, post 2 minute exposure to 532 nm light, and post exposure to 633 nm light respectively.

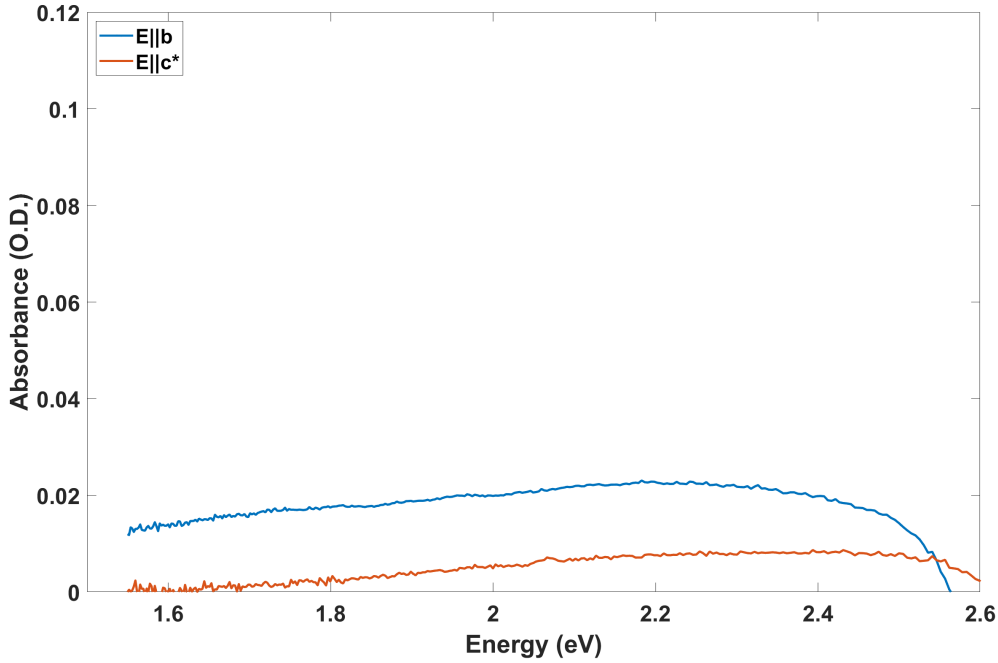

Figure 5.6. Photo-induced optical absorption from $BaGa_4Se_7$ sample 2Y1 (second growth run). The 633 nm absorption spectra has been subtracted from the before light spectra.

5.4 Summary

Examining figures 5.4 and 5.5, from the second growth run, in comparison with figures 5.1 and 5.2, show that the absorption edge occurs at a similar wavelength, however samples from the second growth run did not have comparable optical absorption with samples from the fifth growth run. The induced optical absorption for the $BaGa_4Se_7$ sample from the second growth run in shown in figure 5.6. Comparing the induced absorption between the fifth and second growth runs shows that the induced absorption from the second growth run was an order of magnitude smaller than that of the fifth growth run. The behavior of the EPR signal corresponding to the V_{Se}^{+}(E) selenium vacancy when exposed to 633 nm light is similar to the optical absorption behavior under the same conditions for $BaGa_4Se_7$ samples from the fifth growth run. The EPR signal from this defect was present in the sample before ex-

posure to light and the same EPR signal is subsequently destroyed when exposed to 633 nm light. Likewise there was no appreciable EPR signal detected in $BaGa_4Se_7$ samples from the second growth run, and no comparable optical absorption. This allows a reasonable attribution of of the absorption spectrum seen in figures 5.1 and 5.2 to be assigned to the V_{Se}^{+}(E) selenium vacancy spectrum E shown in figure 4.8(a). The depth of this V_{Se}^{+}(E) electron trap is shallow and thus close to top of the valence band, as demonstrated by the increase in optical absorption after exposure to white light at room temperature.

6. Intrinsic Point Defects in LiB_3O_5 Crystals: Oxygen Vacancies, Lithium Vacancies, and Self-trapped Holes

6.1 Abstract

Lithium triborate (LiB_3O_5, or LBO) is a NLO material widely used to generate second, third, and fourth harmonics of high-power ultra-fast solid-state lasers. Unfortunately, the performance of these crystals is often adversely affected by nonlinear absorption. We show that oxygen vacancies and lithium vacancies are present in as-grown LiB_3O_5 crystals. Transient absorption bands appear, along with thermal degradation, when these intrinsic defects trap "free" electrons and holes created by nonlinear processes (e.g., three- and four-photon absorption). Trapped electrons introduce a band peaking near 300 nm and trapped holes produce bands in the 500-700 nm region [83]. Electron paramagnetic resonance is used to identify and characterize oxygen vacancies (V_O^+) that have trapped an electron on an adjacent boron ion and lithium vacancies (V_{Li}^0) that have trapped a hole on an adjacent oxygen ion. Self-trapped holes are also observed with EPR. EPR results show that some of the lithium vacancies are stabilized by an adjacent OH^- ion or a nearby Cu^{2+} ion. We use x-rays, instead of harmonics from a laser, to generate the free electrons and holes. EPR spectra from oxygen vacancies and self-trapped holes are present after an irradiation at 77 K. The self-trapped holes become unstable near 100 K. Holes trapped at lithium vacancies decay near 160 K. As the temperature is increased, released holes recombine with electrons trapped at oxygen vacancies. These decay temperatures predict that lifetimes of the defect-related absorption bands are between 0.1 and 10 µs at room temperature [83–87].

6.2 Introduction

A fundamental problem in the use of LBO crystals to generate the second, third, and fourth harmonics of rare-earth-based ultra-fast solid-state lasers in the ultraviolet region, is the formation of unwanted transient absorption bands associated with point defects [88–92]. The high pump powers used in these applications allow combinations of the harmonics to bridge the approximate 7.7 eV gap of the LBO crystals and thus produce free electrons and holes. A recent study by Röcker *et al.* has shown that four-photon absorption is the primary nonlinear absorption mechanism during second-harmonic generation and three-photon absorption is the dominant process during third-harmonic generation [88]. Intrinsic point defects (oxygen vacancies and lithium vacancies) are unintentionally present in as-grown LBO crystals and serve as temporary traps for the free electrons and holes generated by the nonlinear absorption processes [20, 23]. Concentrations of these vacancies approach or exceed 1 ppm in typical commercial-quality LBO crystals. Electrons trapped at oxygen vacancies have a broad absorption band peaking near 300 nm and trapped holes have absorption bands in the 500 to 700 nm region [20, 23, 93, 94]. These defect-related absorption bands are especially important as they overlap the second (532 nm) and third (355 nm) harmonics of common near-infrared pump lasers (1064 nm).

In the present paper, we use EPR and infrared optical absorption to demonstrate that oxygen vacancies and lithium vacancies are present in LiB_3O_5 crystals. The oxygen and lithium vacancies are in their nonparamagnetic charge states (V_O^{2+}) and (V_{Li}^{-}) in an as-grown crystal. To maintain charge neutrality, a crystal cannot have just one type of vacancy. Both types must be present, as they provide compensation for each other. Lithium enters the LBO crystal as Li^+ and oxygen enters the LBO crystal as O^{2-}, thus two lithium vacancies compensate one oxygen vacancy. At 77 K, a major portion of the free holes and electrons produced by ionizing radiation (x rays, in our

case) form self-trapped holes and singly ionized oxygen vacancies (V_O^+), respectively, each with a distinct EPR spectrum. When warmed to 100 K after irradiation, the self-trapped holes become thermally unstable and migrate through the crystal before recombining with an electron trapped at an oxygen vacancy, or becoming trapped on an oxygen ion next to a lithium vacancy (and thus forming paramagnetic V_{Li}^0 centers). Further warming above 160 K eliminates the V_{Li}^0 centers and the remaining V_O^+ oxygen vacancies. Estimates of the activation energies describing the thermal decay of self-trapped holes and holes trapped at lithium vacancies are used to predict lifetimes of the transient absorption bands. In addition to the EPR spectra from oxygen vacancies, self-trapped holes, and lithium vacancies, we observe an EPR spectrum from Cu^{2+} ions with an adjacent lithium vacancy. Optical absorption bands, reported in earlier studies, are assigned to specific charge states of the trapped electrons and holes [23, 24, 83].

6.3 Experimental Details

The LiB_3O_5 crystal used in the present study was grown at IPG Photonics Corporation by the top-seeded solution growth method [93,95,96]. An EPR-sized sample with dimensions of $2.3 \times 2.6 \times 3.0$ mm was cut from a larger boule. The crystals were immersed in liquid nitrogen and irradiated with x rays for two minutes from a Varian OEG-76H-Rh tube operating at 60 kV and 30 mA. Our use of x rays, instead of the harmonics of lasers, allowed us to expose the entire volume of the crystal to ionizing radiation and thus increase the concentration of the paramagnetic charge states of defects responsible for unwanted absorption bands.

A Bruker EMX spectrometer operating near 9.39 GHz and an Oxford Instruments ESR-900 helium-gas flow system was used to take the EPR spectra. Corrections for the small difference in the magnetic field at the sample and the spectrometer's Hall

sensor located on a magnet pole cap were made using a Bruker NMR gaussmeter. Approximate concentrations of the EPR-active defects were obtained from comparisons with a Bruker weak-pitch standard. A Cryo Industries optical cryostat with sapphire windows (Model 110-637-DND) was used to maintain the sample temperature near 80 K during the optical absorption measurements.

The LiB_3O_5 crystals are orthorhombic (space group $Pna2_1$) with two glide planes and a screw axis as symmetry elements [97–99]. Lattice constants at 20 °C are $a = 8.4444$ Å, $b = 7.378$ Å, and $c = 5.146$ Å. There are three inequivalent boron sites and five inequivalent oxygen sites in the crystal. All the Li sites are equivalent. The LiB_3O_5 lattice contains both BO_3 and BO_4 units. As shown in figure 6.1, these units combine to form B_3O_7 anionic groups in the crystal. The labeling scheme of the boron and oxygen ions in LBO is in accordance with [97]. Two of the boron ions (B1 and B3) in the B_3O_7 group are threefold bonded and one boron ion (B2) is fourfold bonded. Five of the oxygen ions (O1, O2, O3, O4, and O5) lie close to the plane formed by the B1, B2, and B3 ions. Each lithium ion in the LiB_3O_5 crystals has four oxygen neighbors. Each oxygen ion has two boron neighbors. Four of the five oxygen ions also have a lithium neighbor (O1 is the only oxygen ion that does not have a close Li ion). The Li-O separation distances vary from 1.986 to 2.172 Å, the B1-O and B3-O bond lengths range from 1.348 to 1.397 Å, and the B2-O bond lengths range from 1.461 to 1.487 Å.

6.4 Oxygen Vacancies

Figure 6.2 shows the EPR spectrum produced in LiB_3O_5 by ionizing radiation. The crystal was initially exposed to x rays while being held at 77 K. Immediately after the irradiation, the crystal was quickly transferred from the liquid nitrogen to the cold helium gas flowing through the microwave resonator. The spectrum was then taken

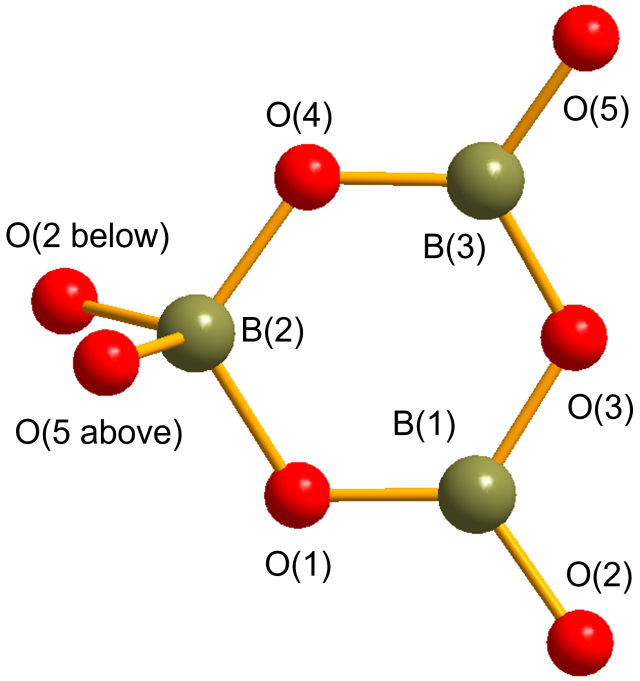

Figure 6.1. A ball-and-stick representation of a portion of the orthorhombic LiB_3O_5 crystal. The boron ions are green, and the oxygen ions are red. Five of the oxygen ions (O1, O2, O3, O4, and O5) lie close to the plane formed by the B1, B2, and B3 ions.

at 55 K, with the magnetic field along the b axis and a microwave frequency of 9.395 GHz. Two defects are present. The upper stick diagrams identify lines from the singly ionized oxygen vacancy (V_O^+) and the lower stick diagram identifies lines from the self-trapped hole. We estimate that the concentration of oxygen vacancies contributing to the spectrum in figure 6.2 is 2.0×10^{17} cm^3. The self-trapped holes appearing in the spectrum have a similar concentration. Oxygen vacancies in LiB_3O_5 crystals have two boron neighbors. Due to the lattice relaxation away from the vacancy, an electron trapped by the vacancy is primarily localized on only one of these boron ions. This results in a large hyperfine interaction with one boron nucleus and a much weaker hyperfine interaction with the other boron nucleus (on the opposite side of the vacancy). The large interaction is responsible for the two widely separated sets of EPR lines in figure 6.2 from the ^{10}B and ^{11}B nuclei. The ^{10}B isotope is 19.9%

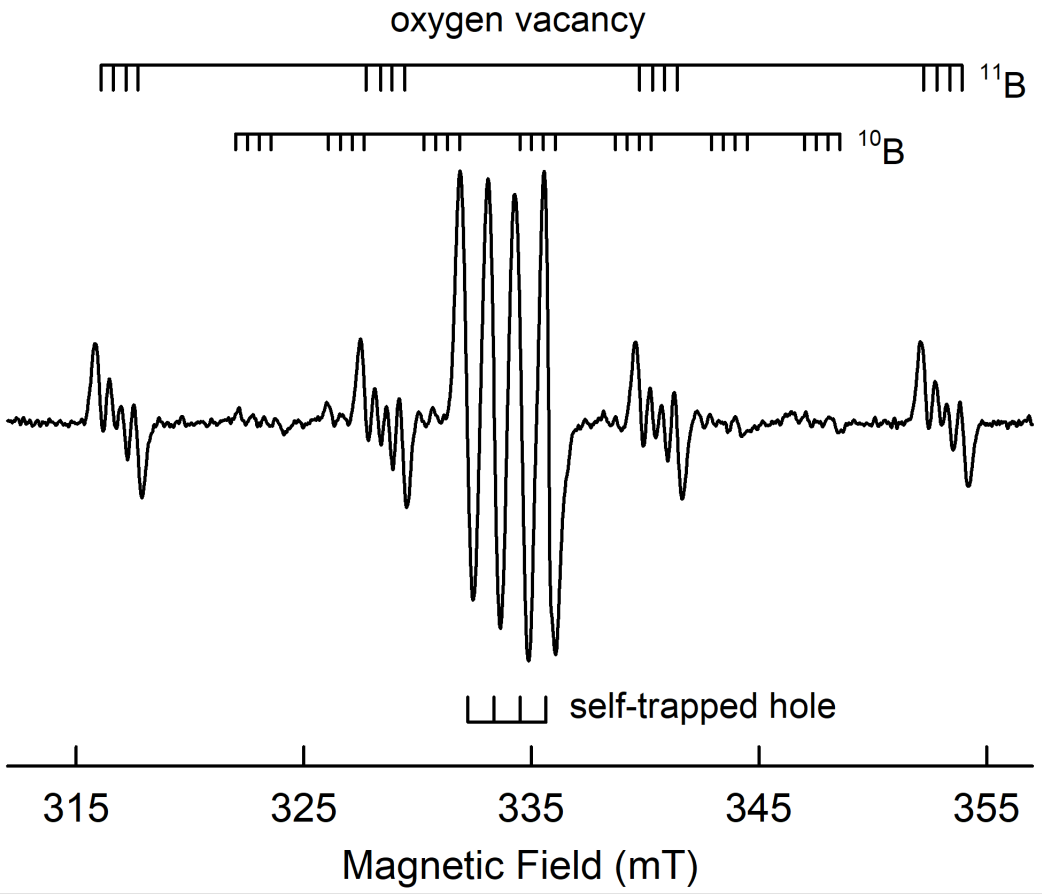

Figure 6.2. EPR spectrum taken at 55 K after the LiB_3O_5 crystal was irradiated at 77 K with x rays. The magnetic field is along the *b* direction and the microwave frequency is 9.39 GHz. The two stick diagrams above the figure identify the positions of the hyperfine patterns from the interaction of the singly ionized oxygen vacancy (V_O^+) with each of the boron isotopes (^{11}B and ^{10}B).

abundant with I = 3 and the ^{11}B isotope is 80.1% abundant with I = 3/2. As the stick diagrams above the spectrum show, the large boron interaction gives four sets of ^{11}B lines separated by 12.47 mT and seven sets of ^{10}B lines separated by 4.16 mT. The number of sets of lines for each isotope are determined by the nuclear spins (2I+1) and the experimental ratio of the separations (2.998) agrees with the ratio of 2.986 predicted by the known nuclear magnetic moments of the ^{10}B and ^{11}B nuclei. The much weaker hyperfine interaction with the opposite boron is responsible for

the additional structure (i.e., the groups of four closely spaced lines with 0.60 mT separation) present on the set of four and the set of seven lines from the primary boron nucleus. These closely spaced lines represent the ^{11}B interaction (the ^{10}B lines are not resolved for this weaker interaction).

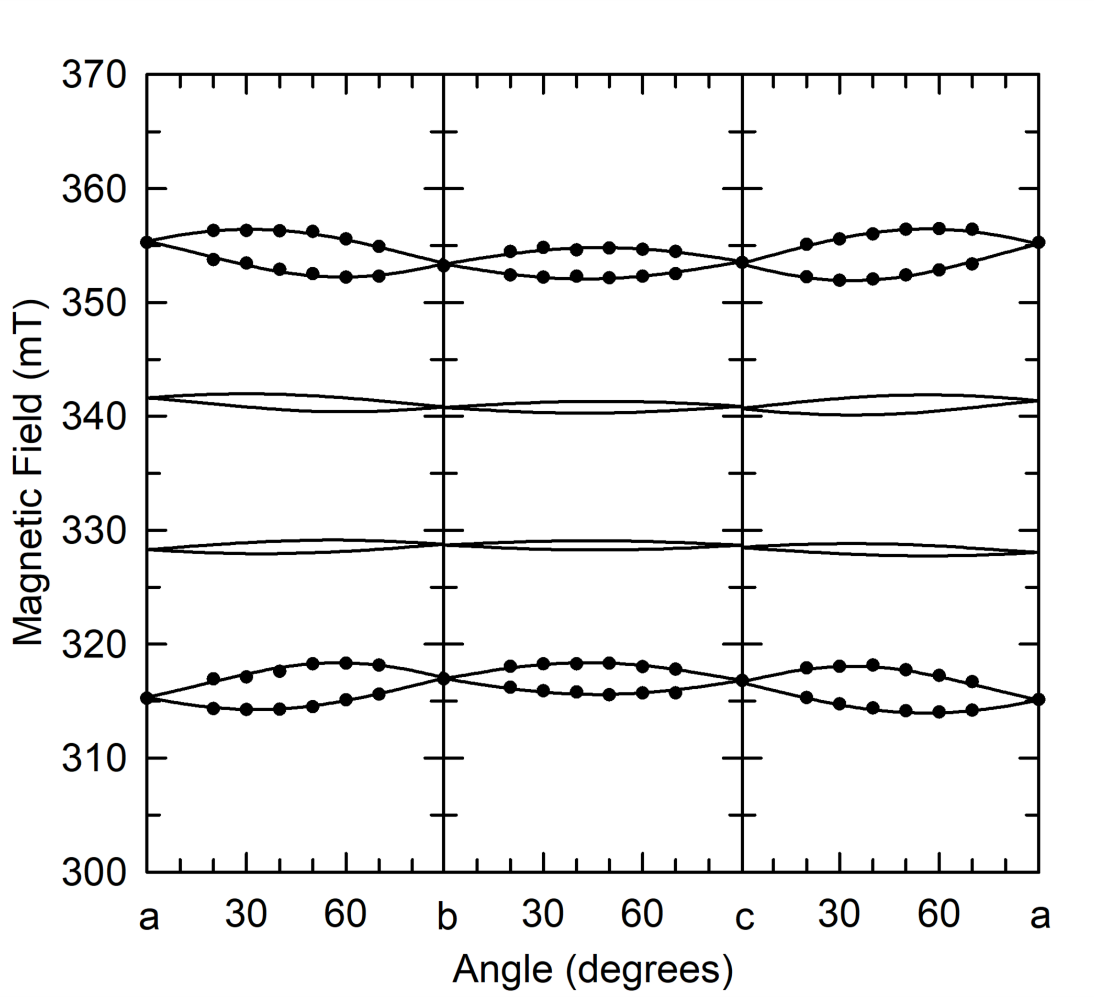

Figure 6.3. EPR data showing the angular dependence of the unpaired spin arising from the *g* matrix for the singly ionized oxygen vacancy (V_O^+). The direction of the magnetic field is rotated from *a* to *b*, *b* to *c*, and *c* to *a*. Discrete points are from experiment. The solid lines were generated using the parameters in table 6.1.

Figure 6.3 shows the angular dependence of the EPR spectrum from the V_O^+ centers. Only the primary ^{11}B interaction is plotted (i.e., the additional weak interaction from the second boron neighbor is not included). The magnetic-field direction is ro-

tated in three planes, from a to b, b to c, and c to a. A spin Hamiltonian, with Zeeman, hyperfine, and nuclear Zeeman terms, describes the angular dependence in figure 6.3.

$$H = \beta \mathbf{S} \cdot \mathbf{g} \cdot \mathbf{B} + \mathbf{I} \cdot \mathbf{A} \cdot \mathbf{S} - g_n \beta_n \mathbf{I} \cdot \mathbf{B} \tag{6.11}$$

V_O^+ Spin Hamiltonian parameters	
g values	A values
2.0016	317.50 MHz
2.0007	415.82 MHz
2.0017	314.58 Mhz
35.44°	41.46°
81.11°	8.25°
16.54°	41.26°

Table 6.1. "Best-fit" spin Hamiltonian parameters for singly ionized oxygen vacancies in a LiB_3O_5 crystal. Line positions used in the fittings were obtained from the EPR spectra shown in figures 6.3. Units for the hyperfine values are MHz. Estimates of uncertainties are ± 0.001 for the g values and ±0.01 MHz for the A values.

The 12 spin parameters in the spin Hamiltonian of equation 6.11 are subdivided into two sets of six parameters; one set for the g values and one set for the A values. Each set contains the three principal values, and the three Euler angles (given in the Z-X-Z convention) defining the principal axis system with respect to the crystal axes [62,100]. To extract the values for the 12 parameters, the spin Hamiltonian in equation 6.11 was rewritten as an 8 × 8 matrix (S = 1/2, I = 3/2) using the $|M_s, m_I\rangle$ basis set. This matrix was then repeatedly diagonalized (to obtain the energy eigenvalues) in a least-squares fitting routine. Input data for the fitting were the 84 pairs of magnetic field values and microwave frequencies representing the experimental points in figure 6.3. In the fitting process, the parameters in the g and A matrices were systematically varied until the predicted line positions agreed with the measured positions. "Best-

fit" values for the spin Hamiltonian parameters are listed in table 6.1.

6.5 Previous Studies of Hole-Traps in LiB_3O_5

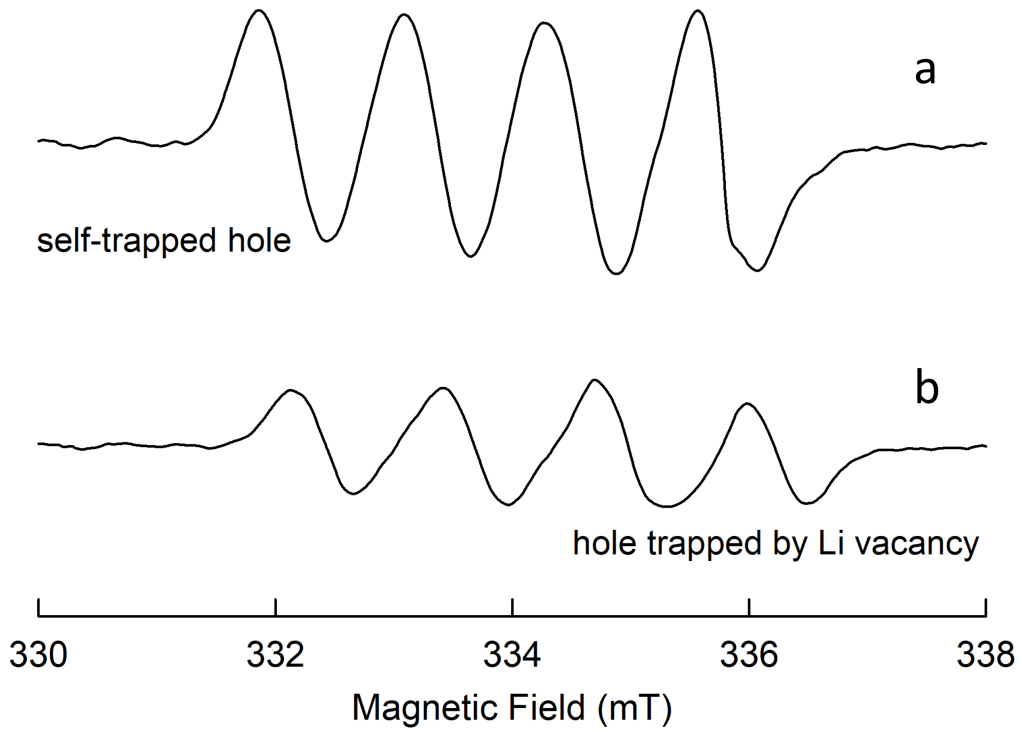

Figure 6.4. The *b* axis EPR spectra of trapped hole centers in LiB_3O_5. Trace a was taken at 55 K after a 77 K irradiation with x rays. The crystal was then warmed to 100 K and trace b was taken at 55 K.

Hole-like centers in single crystals of LBO have been observed after low temperature irradiation and been reported in by previous researchers [20, 23, 101]. Initial observation of the dominant hole center in LBO was first reported by Scripsick *et al.* and is shown as the dominant four-line spectra labeled "self-trapped hole" in figure 6.2 [23]. The four EPR lines correspond to a S = 1/2 defect with I = 3/2 hyperfine interaction, separated by 1.2 mT and centered at 333 mT when the magnetic field is directed parallel the *c* axis. Electron-nuclear double resonance (ENDOR) definitively

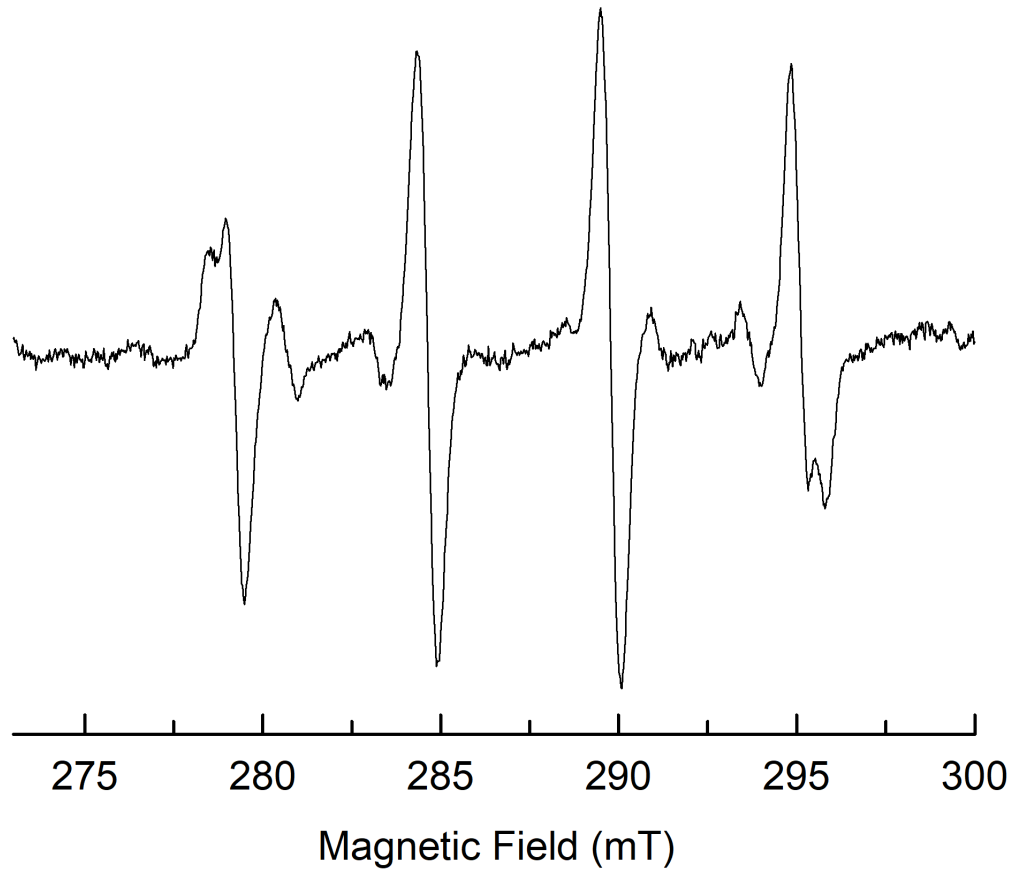

Figure 6.5. Cu^{2+}trapped-hole EPR spectra in LiB_3O_5 irradiated with x rays. The magnetic field was aligned parallel to the *c* axis and the EPR trace taken at 55 K.

assigned ^{11}B as the I = 3/2 nucleus responsible for the four-line hyperfine pattern. Based on the weak hyperfine splitting and the positive g shift, the initial defect model assigned a trapped hole localizing on an oxygen ion adjacent to an effective negatively charged stabilizing entity.

Later Hong *et al.*, under similar experimental conditions, observed both hole-like centers in figure 6.4 and characterized the trapped-hole centers with complete angular dependence studies and ENDOR measurements providing tentative assignments to both defects [20]. Key to Hong's assignment was understanding the thermal stability of each defect through a thermal annealing study. Hole center A, shown in figure 6.4a,

was reported to be thermally unstable when the crystal was held near 130 K [20]. After the decay of hole center A, a second hole center appeared, center B, and is shown in the figure 6.4b. The second hole center decayed when the temperature reached 150 - 200 K region. Both hole-like defects observed were attributed to an S = 1/2 center with the four-line hyperfine pattern caused by a ^{11}B nucleus. Based on these measurements and calculations, center A was attributed to a self-trapped hole, while center B was assigned to a hole trapped at an oxygen ion with a hyperfine interaction with a nearby ^{11}B nucleus and stabilized by a nearby lithium vacancy.

In figure 6.4 we have reproduced both hole centers by irradiating our LiB_3O_5 crystal, at 77 K, placed it in the spectrometer without significant warming and with the magnetic field aligned along the b axis of the crystal. Figure 6.4a is the self-trapped hole center originally identified by Scripsick *et al.* and figure 6.4b is the hole-center that appears after warming the crystal to 100 K. Our observations are consistent with earlier measurements and support the assignments based on the positive g shifts of the order expected for a hole localized primarily on an oxygen ion. While each hole center has strong interaction with only one boron nucleus, the differing thermal stabilities of the defect indicate that these are two separate defects. Hong *et al.* proposed the two possible pathways for this to occur since each oxygen is surrounded by two boron neighbors. The first possibility is a boron vacancy and the other is large lattice relaxation away from the oxygen containing the hole. Of these two possibilities, the large lattice relaxation is consistent with our observations and previously reported results as holes trapped next to vacancies are expected to provide higher thermal stability.

The differing thermal stabilities of the two defects indicate that there are different stabilizing mechanisms. Previously, Hong *et al.* performed ENDOR measurements showing the presence of nearby lithium atoms for center A, while center B did not indicate the nearby lithium. This is consistent with our measurements. Both the

oxygen ion (O^{2-}) and the lithium vacancy (V_{Li}^{-}) are negatively charged and act to stabilize the positive hole trapped at the oxygen ion.

Kananen *et al.* characterized the behavior of Cu^{+} ions diffused into an undoped LiB_3O_5 crystal reporting that the Cu^{+} ions occupy both Li^{+} and interstitial positions in the LiB_3O_5 crystal [102]. Of particular importance to the electron-like defect assignment, Kananen *et al.* reported that the EPR spectra show that Cu^{+} ions at Li^{+} sites trap a hole and convert to Cu^{2+} ions [102]. Two distinct Cu^{2+} trapped-hole spectra in the irradiated LiB_3O_5 crystals are observed: one due to isolated Cu^{2+} ions with no nearby defects and the other due to perturbed Cu^{2+} ions where they perturbing defect was identified as a lithium vacancy (V_{Li}^{-}). In our irradiated LiB_3O_5 crystal, when the magnetic filed was aligned along the c axis we observed the same EPR spectra identified by Kananen *et al.* Figure 6.5 shows an EPR spectra taken at 55 K with the magnetic field along the c axis in our irradiated LiB_3O_5 crystal. This spectra is characterized as a hole (S = 1/2) trapped at Cu^{+} site (thus converting it to Cu^{2+} with a $3d^9$ electron configuration). Copper has two magnetic isotopes, ^{63}Cu and ^{65}Cu, with each having a nuclear spin I = 3/2, but differing magnetic moments that result in two overlapping four-line EPR signals shown in figure 6.5. The ^{65}Cu has a slightly larger magnetic moment that the ^{63}Cu nucleus and thus a the hyperfine spacing is slightly wider. The copper diffusion experiments are important because they establish that copper ions can migrate to lithium sites in the as grown crystal and produce two separate but distinct EPR spectra: those with and without a nearby stabilizing defect. In particular, the more stable of the two reported EPR spectra by Kananen *et al.* indicate the presence of nearby lithium vacancies while the EPR signal attributed to Cu^{2+} ions occupying Li^{+} sites again proves that there are lithium vacancies in LiB_3O_5 crystals.

LBO crystals in the as-grown state require a compensating defect for the charge

deficiency resulting from the presence of lithium vacancies. The firm establishment of lithium vacancies in the as grown crystals severely diminishes the possibility that the electron-like center could result from a boron interstitial. Furthermore, from a purely ionic perspective, the concentration of lithium vacancies and boron interstitials would need to be equal and this is not observed. Based on these observations, we credit our assignment of the electron-like four-line EPR spectra with 12 mT splitting to an electron trapped at an oxygen vacancy with a boron ion as a nearest neighbor as the most likely candidate for the compensating defect to the lithium vacancies.

6.6 Summary

The electron-like center in LiB_3O_5 crystals irradiated at 77 K has been investigated and determined to be an electron trapped at an oxygen vacancy where the lattice relaxation away from the vacancy results in the spin density of the trapped electron to be localized on one boron neighbor. A complete set of spin Hamiltonian parameters is given for this electron trap. A major goal of our present study was to understand the point defects that participate in the transient optical absorption produced in LiB_3O_5 when these crystals are used in second, third, and fourth harmonic generation from rare-earth-based ultrafast solid-state lasers. Two hole-centers and the now identified oxygen vacancy electron trap result in broad absorption bands spanning from 300 nm to 700 nm. This broad absorption band overlaps the wavelength of the second and third harmonics of infrared pump lasers.

7. Summary and Conclusions

7.1 $BaGa_4Se_7$ Summary

Intrinsic anion and cation point defects in $BaGa_4Se_7$ have been identified and characterized for the first time using photo-induced EPR and optical absorption measurements. Samples of two separate and distinct growth runs of single crystals show large concentrations of selenium vacancies are present in the as grown crystals for some growth conditions and serve as transient and stable electron traps when the crystal is illuminated with below band gap photons of 532 nm. Five EPR spectra are observed, each representing singly ionized selenium vacancies V_{Se}^{+} converted from their doubly ionized V_{Se}^{2+} state in the initially received state. The distinct spectra indicate five different vacancy sites among the seven inequivalent sites in this monoclinic crystal and each showing large ^{69}Ga and ^{71}Ga hyperfine interactions. Four of the EPR spectra are stable below room temperature interacting with a single gallium ion while the fifth is stable at 293 K and shows unequal interaction with two neighboring gallium. The electrons localize primarily in an s-like orbital and prevent definitive assignment of each of the defects to specific sites within the crystal due to minimal angular dependence from the spin-orbit coupling. Additionally, EPR measurements have shown for the first time that holes localize on a selenium ions next to a cation vacancy, most likely a Ba^{2+} vacancy, after illumination with sub-band gap light.

The varied stability of the anion defects allowed for a preliminary investigation of the photo-induced optical absorption bands in the visible and near-infrared regions at 80 and 293 K with 532 nm light. While these bands are attributed to singly ionized selenium and barium vacancies, only a tentative assignment of the broad optical absorption band corresponding the selenium vacancy stable at room temperature is able to be effectively isolated in the samples under this study. These optical absorption

bands are expected to contribute to two-photon absorption and also direct one-photon absorption when an OPO is pumped near 1 µm.

Photo-induced EPR signals with 532 nm are destroyed with subsequent illumination at 633 nm for any temperature. The behavior of the EPR signal corresponding to the V_{Se}^{2+} selenium vacancy when exposed to 633 nm light is similar to the optical absorption behavior under the same conditions for $BaGa_4Se_7$ samples from the fifth growth run. The EPR signal from this defect was present in the sample before exposure to light and the same EPR signal is subsequently destroyed when exposed to 633 nm light. Likewise there was no appreciable EPR signal detected in $BaGa_4Se_7$ samples from the second growth run, and no comparable optical absorption. This allows a reasonable attribution of the absorption spectrum seen in figures 5.1 and 5.2 to be assigned to the V_{Se}^{+} selenium vacancy spectrum E shown in figure 4.8(a).

7.2 LiB_3O_5 Summary

Ambiguity surrounding the electron-like center in LiB_3O_5 crystals irradiated at 77 K has conclusively been shown to be an electron trapped at an oxygen vacancy resolving 30 years of speculation to its cause. Single crystals of LiB_3O_5 are shown to contain three intrinsic defects: self-trapped holes, lithium vacancies, and oxygen vacancies. All of these intrinsic defects are shown to be unstable at room temperature, but are important for transient absorption in high power applications. The addition of a complete set of spin Hamiltonian parameters for the oxygen vacancy completes the study of isolated intrinsic point defects building on the previous characterization of the two hole-like centers. The oxygen vacancy has been shown to result in lattice relaxation away from the vacancy site with the majority of the spin density of the trapped electron localizing on one boron neighbor and serves as the compensating defect to native lithium vacancies.

Furthermore, a significant accomplishment is understanding the role of point defects participating in the transient optical absorption produced in LiB_3O_5 when these crystals are used in second, third, and fourth harmonic generation from rare-earth-based ultrafast solid-state lasers. The transient formation of these defect result in broad absorption bands spanning from 300 to 700 nm. This broad absorption band overlaps the wavelength of the second and third harmonics of infrared pump lasers.

7.3 Additional point defects in $BaGa_4Se_7$

In $BaGa_4Se_7$, definitive identification and characterization of the native cation vacancies (barium and gallium vacancies) remain unresolved questions. $BaGa_4Se_7$ is still a relatively unexplored material, owing to its recent availability. Calculations are not available to suggest their depth in the bandgap or which of the defects is most energetically favorable to exist as the compensating defect to observed selenium vacancies. The unusual hyperfine spectra shown from the selenium vacancies indicate that cation vacancy spectrum may bear unique features or present special challenges for observation due to sensitivities with temperature stability and microwave power saturation.

Analysis of more mature growth runs of $BaGa_4Se_7$, combined with neutron irradiation of the crystals may provide a path forward for uncovering and more thorough studying of cation vacancies in this material. To date, neutron irradiation has been performed on a single $BaGa_4Se_7$ crystal. This crystal was from the second growth run of the material where only small changes were detected in defect concentrations, and no changes were observed in the optical absorption. This result is inconsistent with the expectation of neutron irradiation performing knock-on damage to the lattice and indicates that the neutron flux and energy deposition into the crystal may be important for accurate, detailed studies. A wider study, encompassing multiple samples,

various irradiation fluences, and temperatures should be performed with EPR and optical absorption measurements conducted before and after irradiation to measure changes.

Furthermore, many wide band gap nonlinear optical materials have exhibited anti-site defects resulting from varied growth conditions. The large difference in ionic radii between the cation sites of $BaGa_4Se_7$ and the in-equivalence of the gallium and selenium sites provide many possible combinations for anti-site defects to emerge. The disruption to the periodicity and symmetry of the $BaGa_4Se_7$ lattice resulting from such defects is expected to produce absorption bands that may degrade performance. Understanding these defects and the growth conditions that lead to their formation is key to commercial and military advancement of $BaGa_4Se_7$ as a material suitable for high power applications.

7.4 Future Applications for NLO Materials

The materials explored in this dissertation have broad functionality for both commercial and military applications. $BaGa_4Se_7$ crystals are used to down-convert light to longer wavelengths via optical parametric oscillation, while LiB_3O_5 crystals are used in the generation of second, third, and forth harmonics of rare-earth based solid-state lasers. Thee two crystals also represent two opposing ends of NLO materials maturity: one is an established, mature material (LiB_3O_5), and the other is an emerging material ($BaGa_4Se_7$). The forecasted trends for future generations of NLO materials such as $BaGa_2GeSe_6$ and $BaGa_2Ge_2Se_6$ indicate that lower symmetry and more complex constituents will be the norm rather than the academic exception. NLO materials will continue to be of interest to the Department of Defense, Department of Energy, and the United States commercial industry. As result, it is in the national interests of the United States to learn as much as possible about these simpler crystals and

materials before the techniques for investigating them are rendered obsolete by the complexities of their crystallographic nature.

Appendix A. Review of 3-wave mixing and $\chi^{(2)}$ Processes

The exchange of energy between the electric field of the incident light and the nonlinear optical material is through the coupling of the electric field to the induced polarization of the medium via its susceptibility. The equation for the polarization of a dielectric material is

$$\vec{P} = \epsilon_0 \chi^{(1)} \vec{E}(t) + \epsilon_0 \chi^{(2)} \vec{E}^2(t) + \epsilon_0 \chi^{(3)} \vec{E}^3(t) + \dots \tag{A.1}$$

where the susceptibility has been expanded in a power series to show the linear, $\chi^{(1)}$, and nonlinear $\chi^{(n)}$ (where $n \geq 2$) contributions to the polarization. Equation (A.1) can be rewritten as $\vec{P} = \vec{P^L} + \vec{P^{NL}}$ where the first term in equation (A.1) is the linear polarization and the remaining terms are combined into the nonlinear polarization.

Second order polarization effects ($\chi^{(2)}$), are essential to the application of frequency conversion using nonlinear optical crystals, and will be the only nonlinear process discussed in this dissertation. The relationship between the output power from the frequency conversion process and the induced polarization of the medium is shown through the analysis of Poynting's theorem,

$$\oint_s \vec{S} \cdot \vec{da} = \int_v \left[\left(\frac{-\partial U_{EH}}{\partial t}\right) - (\vec{E} \cdot \vec{J_f}) - \left(\vec{E} \cdot \frac{-\partial \vec{P}}{\partial t}\right) \right] d\tau \tag{A.2}$$

where $\vec{S}$ is the Poynting vector, U_{EH} is the electromagnetic energy stored in the the fields bounded by the surface, $\vec{E}$ is the electric field vector, $\vec{J_f}$ is the free current density, and $\vec{P}$ is the polarization from equation (A.1). Equation (A.2) is essentially an energy balance equation (divergence theorem) with three source terms. The left-hand side represents the energy flux through a surface and the right-hand side consists of three source terms: the rate of change in the electromagnetic energy stored in the fields, the rate at which work is done by the fields on free charges in the volume, and

the rate at which work is done by the field on the medium via polarization. This last term shows that change in polarization of the medium contributes to the energy exchange between the incident light and the dielectric medium [7].

Given two co-linear monochromatic plane waves, of the form $E_i(z,t) = A_i(z)e^{(-i\omega_i t)}$, on input with angular frequency ω_1 and ω_2 respectively, the generation of the sum and difference frequencies of the incident optical fields is shown via the expansion of the the E^2, associated with the first nonlinear term ($\chi^{(2)}$) in equation (A.1) as shown below.

$$E^2 = \left[A_2^2 e^{-i(2\omega_2)t} + A_3^2 e^{-i(2\omega_3)t} + 2A_2A_3e^{-i(\omega_2+\omega_3)t} + A_2A_3^* e^{-i(\omega_2-\omega_3)t}\right] + c.c.$$
$$+ 2A_2A_2^* + 2A_3A_3^*$$

The terms with $2\omega_2$ and $2\omega_3$ in the exponential represent second harmonic generation (SHG) of ω_2 fields and ω_3 fields respectively. The third and fourth terms, with $\omega_2 + \omega_3$ and $\omega_2 - \omega_3$ in the exponential, represent sum frequency generation (SFG) and difference frequency generation (DFG) fields respectively. The last two terms represent a static (frequency independent) polarization called optical rectification.

Below is the full derivation of the expansion of the E^2 term. Let two incident collinear monochromatic plane waves E_2 and E_3 be

$$E_2 = A_2e^{(-i\omega_2 t)} + A_2^* e^{(i\omega_2 t)} \tag{A.3}$$

$$E_3 = A_3e^{(-i\omega_3 t)} + A_3^* e^{(i\omega_3 t)} \tag{A.4}$$

where A_i represent the amplitudes and ω_i represent the angular frequencies of the two incident waves respectively. The total input is expressed as a superposition of the two incident waves.

$$
\begin{aligned}
E &= E_2 + E_3 \\
&= A_2 e^{-i(\omega_2 t)} + A_2^* e^{i(\omega_2 t)} + A_3 e^{-i(\omega_3 t)} + A_3^* e^{i(\omega_3 t)} \\
E^2 &= A_2^2 e^{-i(2\omega_2)t} + A_2 A_3 e^{-i(\omega_2+\omega_3)t} + A_2 A_2^* + A_2 A_3^* e^{i(\omega_3-\omega_2)t} \\
&+ A_3 A_2 e^{-i(\omega_2+\omega_3)t} + A_3^2 e^{-i(2\omega_3)t} + A_3 A_2^* e^{i(\omega_2-\omega_3)t} + A_3 A_3^* \\
&+ A_2^* A_2 + A_2^* A_3 e^{i(\omega_2-\omega_3)t} + A_2^* A_2 * e^{i(2\omega_2)t} + A_2^* A_3^* e^{i(\omega_2+\omega_3)t} \\
&+ A_3^* A_2 e^{i(\omega_3-\omega_2)t} + A_3^* A_3^* + A_3^* A_2^* e^{i(\omega_2+\omega_3)t} + A_3^* A_3^* e^{(i(2\omega_3)t}
\end{aligned}
$$

By grouping like terms, the expression for the square of the complex electric field can be succinctly written as

$$
E = \left[A_2^2 e^{-i(2\omega_2)t} + A_3^2 e^{-i(2\omega_3)t} + 2A_2 A_3 e^{-i(\omega_2+\omega_3)t} + A_2 A_3^* e^{-i(\omega_2-\omega_3)t}\right] + c.c. + 2A_2 A_2^* + 2A_3 A_3^* \tag{A.5}
$$

It is now clear to see how the mixing of input plane waves generates waves at the sum and difference frequencies of all waves present. The terms with $2\omega_2$ and $2\omega_3$ in the exponent represent the second harmonic generation (SHG) of ω_2 and ω_3 respectively. The terms with $\omega_2 + \omega_3$ and $\omega_2 - \omega_3$ in the exponent represents the sum frequency generation (SFG) and difference frequency generation (DFG)respectively. These four terms also have corresponding complex conjugates. The last two terms represent optical rectification (OR) of the ω_2 and ω_3 waves respectively. This exercise also makes clear that SFG and DFG process have two waves on input whereas SHG and OR each only have one frequency term. Using this fact in conjunction with equations (A.10) and (A.11) a general polarization formula encompassing all four

$\chi^{(2)}$ processes can be used.

$$P_i^{(2)}(\omega_1) = 4D\epsilon_0 \sum_{j,k} \chi_{ijk}^{(2)} E_j(\omega_2) E_k(\omega_3) \tag{A.6}$$

where

$$D = \begin{cases} 1/2 & \text{for OR and SHG} \\ 1 & \text{for SFG and DFG} \end{cases} \tag{A.7}$$

The labeling of the subscripts is consistent with the convention

$$\omega_1 > \omega_2 \geq \omega_3 \tag{A.8}$$

where each corresponds to the pump, signal, and idler frequencies respectively [7]. In literature the quantity $\sum_{j,k} \chi_{ijk}^{(2)}$ is referred to as effective nonlinearity, d_{eff}, for each second-order Cartesian polarization direction $P_i^{(2)}$.

Note that equation A.5 has 10 unique terms, the number of which is predicted by the multinomial theorem. The multinomial theorem states the the number of unique terms in the expansion of $(x_1 + x_2 + \ldots x_m)^n$ is:

$$N = \frac{(n+m-1)!}{n!(m-1)!}. \tag{A.9}$$

Third order nonlinear effects, χ^3 processes, entail the effects of four-wave mixing, specifically: self focusing, phase conjugation, Raman scattering, and Brillouin scattering. Third order nonlinear optical interactions include self-induced effects, where the interaction generates nonlinear polarization at the same frequency as the the input and can occur in both centrosymmetric and noncentrosymmetric media [7, 103]. These χ^3 processes can have up to three possible input frequencies and the expansion of E^3 yields a total of 56 terms in accordance with the multinomial theorem.

The second-order nonlinear susceptibility ($\chi^{(2)}$) is a third-rank tensor with 27 components. The second-order polarization, with two waves at optical frequencies ω_n and ω_m respectively, can be expressed mathematically by:

$$P_i^{(2)}(\omega_n + \omega_m) = 2\epsilon_0 \sum_{j,k} \chi_{ijk}^{(2)} E_j(\omega_m) E_k(\omega_n) \tag{A.10}$$

where i, j, k correspond to the Cartesian x, y, z coordinates. For each Cartesian direction i, there are nine possible permutations of j, k. For example when $i = x$ the permutations of j, k are

i	j	k
x	x	x
x	x	y
x	x	z
x	y	x
x	y	y
x	y	z
x	z	x
x	z	y
x	z	z

The (xyz) tensor element gives the nonlinear polarization generated along the x axis when one optical field is applied along the y axis and another applied along the z axis. Crystals can be described as a lattice with a basis. There are certain rotation operation that transform the crystal into itself that leave one point in the lattice fixed. This group of rotation operations are called the point group symmetry of the crystal. It is due to the point group symmetry of crystals that many of the susceptibility tensor terms are zero. When operating at frequencies below the absorption edge some of

the susceptibility tensor elements are degenerate (i.e.the same). This latter condition (degenerate tensor elements) is referred to as Kleinmann symmetry [15]. There are only 18 physically distinct elements of the ($\chi^{(2)}$) tensor, 6 for each Cartesian direction, as the (xxy) element is identical to the (xyx) element. With full permutation symmetry applied the ijk index notation is contracted to il where the second and third indices jk have been contracted into one index l

j	k	l
x	x	11
y	y	12
z	z	13
$z(y)$	$y(z)$	14
$z(x)$	$x(z)$	15
$x(y)$	$y(x)$	16

In literature the ($\chi^{(2)}$) tensor is usually presented in terms of the contracted tensor called a "d-tensor" where the relationship between the d-tensor and the ($\chi^{(2)}$) tensor is

$$d_{il} = \frac{1}{2}\chi^{(2)}_{il}. \tag{A.11}$$

These d-tensors are classified by the point group symmetry of the crystal and can be found in Butcher [104]. Specific elements of the d-tensor are the NLO coefficients reported in literature. For example, the d-tensor for $BaGa_4Se_7$, which is monoclinic, denoted as point group symmetry class m is

$$d_{il} = \begin{bmatrix} d_{11} & d_{12} & d_{13} & 0 & d_{15} & 0 \\ 0 & 0 & 0 & d_{24} & 0 & d_{26} \\ d_{31} & d_{32} & d_{33} & 0 & d_{35} & 0 \end{bmatrix}, \tag{A.12}$$

where

$$d_{12} = d_{26}$$

$$d_{13} = d_{35}$$

$$d_{15} = d_{31}$$

$$d_{24} = d_{32}$$

due to Kleinmann symmetry. LiB_3O_5 has an orthorhomic crystal structure with point group symmetry class $mm2$ and a d-tensor

$$d_{il} = \begin{bmatrix} 0 & 0 & 0 & 0 & d_{15} & 0 \\ 0 & 0 & 0 & d_{24} & 0 & 0 \\ d_{31} & d_{32} & d_{33} & 0 & 0 & 0 \end{bmatrix}, \tag{A.13}$$

where

$$d_{15} = d_{31}$$

$$d_{24} = d_{32}$$

.

For any given direction in anisotropic crystals there are two phase velocities, and thus two indices of refraction. This is of critical importance when phase matching is desired as the index of refraction (n) is related to the wave number.

$$k = \frac{2\pi}{(\lambda/n)} = \frac{n\omega}{c} \tag{A.14}$$

This fact is elucidated by evaluating the two solutions to Fresnel's equation for the

index of refraction n.

$$\begin{aligned} 0 = &(\frac{1}{n_y^2} - \frac{1}{n^2})(\frac{1}{n_z^2} - \frac{1}{n^2})s_x^2 \\ &+ (\frac{1}{n_x^2} - \frac{1}{n^2})(\frac{1}{n_z^2} - \frac{1}{n^2})s_y^2 \\ &+ (\frac{1}{n_x^2} - \frac{1}{n^2})(\frac{1}{n_y^2} - \frac{1}{n^2})s_z^2 \end{aligned}$$

where s_i are the x, y, z amplitudes of the wave vector $\vec{k}$, such that

$$\vec{k} = s_x\hat{x} + s_y\hat{y} + s_z\hat{z}$$

and the n_i are the principal indicies of refraction. By evaluating Fresnel's equation one principal plane at a time, (for example in the (k_x, k_y) plane $s_z = 0$ and noting that $s_y^2 + s_x^2 = 1$), the equation reduces to

$$0 = (\frac{1}{n_z^2} - \frac{1}{n^2})(\frac{s_x^2}{n_y^2} + \frac{s_y^2}{n_x^2} - \frac{1}{n^2}) \tag{A.15}$$

The two solutions are either $n = n_z$ or n takes the form of an ellipse dependent on the direction of the wave vector (i.e the s_x and s_y components), in the (k_x, k_y) plane. The constant solution is called the *ordinary wave* and is independent of the wave vector direction in the plane, and the electric field vector is perpendicular to the principal plane of propagation. The elliptical solution changes depending on the wave vector direction and is called the *extraordinary wave*, where the electric field vector lies in the principal plane of propagation. Phase matching dictates the relationship between the wave vectors of the three waves and this birefringent property, where the index of refraction is dependent upon the polarization and wave vector, of NLO crystals

offers a tuning range where the phase matching condition (equation A.16) is satisfied. For an OPO laser there are two possible phase matching conditions: *ooe* and *eoe*, where *o* and and *e* represent ordinary and extraordinary waves, and the combination is understood to be of the form: input, input, output. For example, an *ooe* phase matching condition corresponds to two ordinary waves on input and an extraordinary wave on output.

The perfect phase matching condition specific to the sum frequency generation process is given as

$$\Delta\vec{k} = \vec{k}_2 + \vec{k}_3 - \vec{k}_1 = 0, \tag{A.16}$$

where $\Delta\vec{k}$ is called the "phase mismatch" of wave vectors and the labeling of the subscripts are consistent with the convention in equation A.8.

Phase matching dictates the relationship between the wave vectors of the three waves and due to the frequency dependence of the index of refraction, called dispersion. The spread of angles of incidence around $\Delta\vec{k}$ offers a tuning range where the phase matching condition, equation A.16, is nearly satisfied. When the perfect phase matching condition is satisfied, the most efficient transfer power between the input and output light beams is possible.

Appendix B. Poynting's theorem

This appendix showing the derivation of Poynting's theorem from Maxwell's equations is provided in order to solidify the understanding of how the induced polarization contributes to the energy exchange between optical fields in a dielectric medium. We begin with Maxwell's equations in matter

$$\boldsymbol{\nabla} \cdot \vec{D} = \rho_f \tag{B.1}$$

$$\boldsymbol{\nabla} \cdot \vec{B} = 0 \tag{B.2}$$

$$\boldsymbol{\nabla} \times \vec{E} = -\frac{\partial \vec{B}}{\partial t} \tag{B.3}$$

$$\boldsymbol{\nabla} \times \vec{H} = \vec{J}_f + \frac{\partial \vec{D}}{\partial t} \tag{B.4}$$

and the two constitutive equations for the electric displacement and the magnetic field

$$\vec{D} = \epsilon_0 \vec{E} + \vec{P} \tag{B.5}$$

$$\vec{H} = \frac{1}{\mu_0} \vec{B} - \vec{M} \tag{B.6}$$

Equation B.5 is the first of the constitutive equations and relates the electric displacement $\vec{D}$ to the electric field vector $\vec{E}$ and the polarization $\vec{P}$. Equation B.6 is the second of the constitutive equations and relates the magnetic field $\vec{H}$ to the magnetic flux density $\vec{B}$ and the magnetization $\vec{M}$. A useful vector identity for the divergence of the cross product of two vectors, $\vec{X}$ and $\vec{Y}$, is employed in this derivation is given below.

$$\boldsymbol{\nabla} \cdot \left(\vec{X} \times \vec{Y} \right) = -\vec{X} \cdot (\boldsymbol{\nabla} \times \vec{Y}) + \vec{Y} \cdot (\boldsymbol{\nabla} \times \vec{X}) \tag{B.7}$$

The Poynting vector is defined as

$$\vec{S} = \vec{E} \times \vec{H} \tag{B.8}$$

The divergence of the Poynting vector given in B.8, and using the vector identity given in equation B.7 yields

$$\boldsymbol{\nabla} \cdot \vec{S} = -\vec{E} \cdot (\boldsymbol{\nabla} \times \vec{H}) + \vec{H} \cdot (\boldsymbol{\nabla} \times \vec{E}) \tag{B.9}$$

By substituting equations B.4 and B.3 for the two field terms within the two parentheses, respectively, equation B.9 becomes

$$\boldsymbol{\nabla} \cdot \vec{S} = -\vec{E} \cdot (\vec{J}_f + \frac{\partial \vec{D}}{\partial t}) - \vec{H} \cdot -\frac{\partial \vec{B}}{\partial t} \tag{B.10}$$

Using the two constitutive equations (B.5 and B.6) equation B.10 becomes

$$\boldsymbol{\nabla} \cdot \vec{S} = -\vec{E} \cdot (\vec{J}_f + \epsilon_0 \frac{\partial \vec{E}}{\partial t} + \frac{\partial \vec{P}}{\partial t}) - \vec{H} \cdot (\frac{\partial \vec{H}}{\partial t} + \frac{\partial \vec{M}}{\partial t}) \tag{B.11}$$

Note that in equation (B.11) there is a $\vec{E} \cdot \frac{\partial \vec{E}}{\partial \vec{E}}$ term and a $\vec{H} \cdot \frac{\partial \vec{H}}{\partial \vec{H}}$ term. By defining $U_{EH} = \frac{1}{2}(\epsilon_0 \vec{E} \cdot \vec{E} + \mu_0 \vec{H} \cdot \vec{H})$ to be the energy stored in the electric ($\vec{E}$) and magnetic ($\vec{H}$) fields, equation (B.11) can now be written as

$$\boldsymbol{\nabla} \cdot \vec{S} = -\frac{\partial}{\partial t} U_{EH} - \vec{E} \cdot \vec{J}_f - \vec{E} \cdot \frac{\partial \vec{P}}{\partial t} - \mu \vec{H} \cdot \frac{\partial \vec{M}}{\partial t} \tag{B.12}$$

Next integrate both sides of equation (B.12) over the entire volume of charge, which yields

$$\int_v \boldsymbol{\nabla} \cdot \vec{S} d\tau = \int_v [(\frac{-\partial U_{EH}}{\partial t}) - (\vec{E} \cdot \vec{J}_f) - (\vec{E} \cdot \frac{-\partial \vec{P}}{\partial t}) - (\mu \vec{H} \cdot \frac{\partial \vec{M}}{\partial t})] d\tau \tag{B.13}$$

Finally, applying the divergence theorem to the left-hand side (LHS) and setting the magnetization of the material to zero ($\mathbf{M} = 0$), and we arrive at the form of Poynting's theorem mentioned in Appendix A equation (A.2), and repeated here in equation B.14.

$$\oint_s \vec{S} \cdot \vec{da} = \int_v \left[(\frac{-\partial U_{EH}}{\partial t}) - (\vec{E} \cdot \vec{J_f}) - (\vec{E} \cdot \frac{-\partial \vec{P}}{\partial t}) \right] d\tau \tag{B.14}$$

Again, the left-hand side represents the energy flux through a closed surface. The first term on the right-hand side (RHS) is the rate of change in the electromagnetic energy stored in the fields bounded by the surface. The second term on the RHS is the rate at which work is done on free charges in the volume. The third term on the RHS is the rate at which work is done by the electric field on the medium via polarization (separation of charge). Polarization of a medium is central to the study of nonlinear optics and is the source energy exchange between a medium and the electric field [7].

Appendix C. Spin Hamiltonian Matrix Diagonalization

We begin the calculation of the Selenium vacancy (V^{+}_{Se}) in $BaGa_4Se_7$ spin hamiltonian by assuming the following form containing only the isotropic electron Zeeman and hyperfine terms; see Chapter 2 equations (2.21) and (2.30).

$$\hat{H} = g\beta \mathbf{B}^T \cdot \hat{S} + A_0 \hat{S}^T \cdot \hat{I} \tag{C.1}$$

The electron configuration the Selenium atom is $[\mathrm{Ar}]3d^{1}04s^{2}4p^{4}$. The ionic notation shows that the outer p shell lacks two electrons to be full and will likely accept two electrons to achieve an electron configuration of the nearest noble gas, Krypton. Thus, the neutral Selenium vacancy (V^{0}_{Se}) has an effective charge of +2e, as the missing anion has an effective positive charge. We suggest that the singly ionized selenium vacancies are formed by the 532 nm light when electrons are optically excited from the valence band to doubly ionized selenium vacancies V^{2+}_{Se}. This excitation process converts nonparamagnetic V^{2+}_{Se} vacancies to paramagnetic V^{+}_{Se} vacancies. The V^{+}_{Se} charge state is paramagnetic with an effective spin $\mathbf{S} = \frac{1}{2}$. This is an F-center as discussed in section 2.2.3 of Chapter 2. A similar ionic analysis of barium (Ba) and gallium (Ga) show that each exist in the $BaGa_4Se_7$ crystal as Ba^{+2} and Ga^{+3} respectively. Both barium and gallium have the same nuclear spin value $I = \frac{3}{2}$. The unpaired spin of the V^{+}_{Se} vacancy will be attracted to the Ga^{+3} ion and thus a 4-line hyperfine absorption pattern is expected. When $\hat{H}_{EZ} > \hat{H}_{HF}$ the predicted number of EPR absorption lines is equal to $2I + 1$. The selection rules for allowed EPR transitions are $\Delta M_s = 1$ and $\Delta M_I = 0$. An energy-level scheme for the hyperfine energy splitting is shown below.

We choose $\mathbf{B}$ to be in the z direction and therefore equation (C.1) becomes

$$\hat{H} = g\beta B S_z + A_0(I_x S_x + I_y S_y + I_z S_z) \tag{C.2}$$

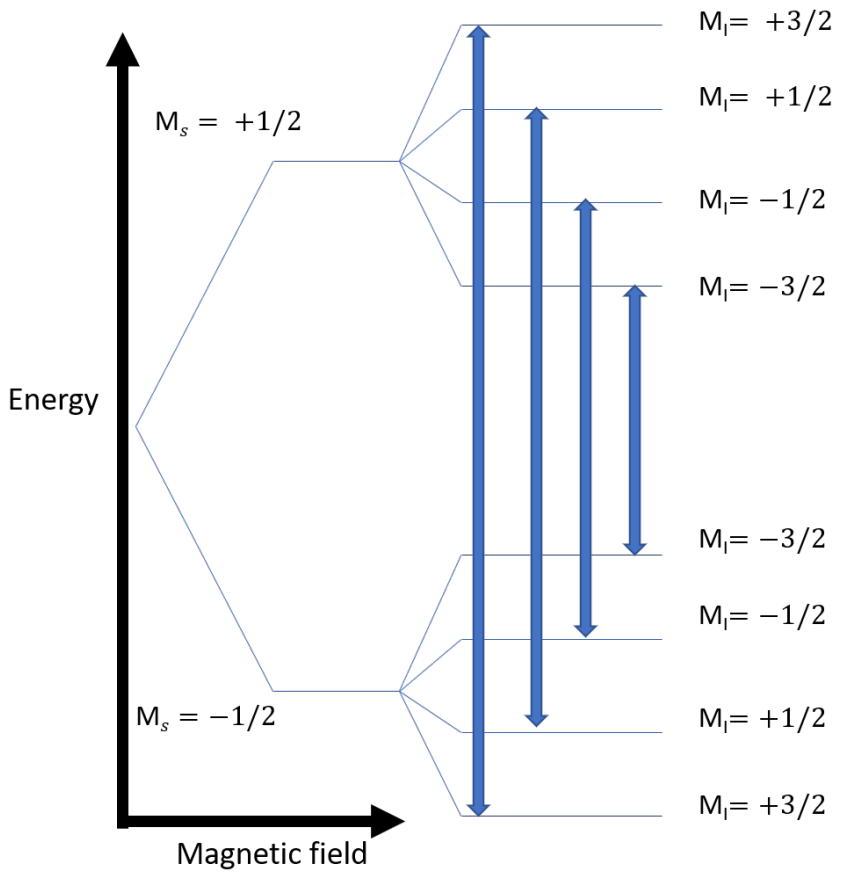

Figure C.1. Energy-level scheme for $\mathrm{S} = \frac{1}{2}$, $\mathrm{I} = \frac{3}{2}$

C.1 Raising and Lowering Operator Method

This section presents the calculation of the matrix elements of the spin Hamiltonian using raising and lowering operators with transitions constrained to the selection rules for allowed EPR transitions. An alternate, and more mathematically simple, is presented in the next section.

Starting with equation (C.2) and separating the terms that depend on the z-component from all others yields

$$\hat{H} = g\beta B S_z + A_0 I_z S_z + A_0 (I_x S_x + I_y S_y) \tag{C.3}$$

We now define raising and lowering operators $\hat{S_+}, \hat{S_-}, \hat{I_+}$, and $\hat{I_-}$ as follows

$$\hat{S}_+ \equiv \hat{S}_x + i\hat{S}_y \tag{C.4}$$

$$\hat{S}_- \equiv \hat{S}_x - i\hat{S}_y \tag{C.5}$$

$$\hat{I}_+ \equiv \hat{I}_x + i\hat{I}_y \tag{C.6}$$

$$\hat{I}_- \equiv \hat{I}_x - i\hat{I}_y \tag{C.7}$$

$$\tag{C.8}$$

By adding equations (C.4) and (C.5) we arrive at an expression for $\hat{S}_x$; and by subtracting the same two equations an expression for $\hat{S}_y$.

$$\hat{S}_x = \frac{1}{2}(\hat{S}_+ + \hat{S}_-) \tag{C.9}$$

$$\hat{S}_y = \frac{1}{2i}(\hat{S}_+ + i\hat{S}_-) \tag{C.10}$$

and likewise for $\hat{I}_+$ and $\hat{I}_-$. Equation (C.3) now becomes

$$\hat{H} = g\beta B S_z + A_0 I_z S_z + \frac{A_0}{2}(\hat{S}_+\hat{I}_- + \hat{S}_-\hat{I}_+) \tag{C.11}$$

The electronic and nuclear spin states form a complete set of commuting observables, and thus the eigenvalues of the commuting operators completely describe the spin state of the system. We label the electronic and nuclear spin states as $|M_s\rangle$ and $|M_I\rangle$ respectively. The action of the S_z and I_z operators operating on their respective electronic and nuclear spin states respectively are

$$\hat{S}_z |M_s\rangle = M_s |M_s\rangle \tag{C.12}$$

$$\hat{I}_z |M_I\rangle = M_I |M_I\rangle \tag{C.13}$$

The action of the raising and lowering spin operators operating on a spin state represented by $|M_s\rangle$ are given by

$$\hat{S}_+ |M_s\rangle = \sqrt{(S(S+1) - M_s(M_s+1)}\, |M_s+1\rangle \tag{C.14}$$

$$\hat{S}_- |M_s\rangle = \sqrt{(S(S+1) - M_s(M_s-1)}\, |M_s-1\rangle \tag{C.15}$$

and likewise for $\hat{I}_+$ and $\hat{I}_-$ operating on a corresponding nuclear spin state represented as $|M_I\rangle$. For a given value S, the eigenvalues M_S span from S to $-S$ in increments of one. For a given value of I, the eigenvalues M_I span from I to $-I$ in increments of one. The sum of the first two terms in equation (C.11) constitute the diagonal matrix elements of the spin Hamiltonian as the $\hat{S}_z$ and $\hat{I}_z$ operators acting on states labeled by $|M_s, M_I\rangle$ do not produce changes to the M_s or M_I states. The off-diagonal elements of the spin Hamiltonian matrix correspond to a change in electronic state. An example calculation of the matrix elements forming the Hamiltonian operator, for the elements H_{22} and H_{52}, where $S = \frac{1}{2}$, $I = \frac{3}{2}$, $M_s = \frac{1}{2}$ and $M_I = \frac{1}{2}$, are shown below.

$$H_{22} = g\beta B S_z |M_s, M_I\rangle + A_0 I_z S_z |M_s, M_I\rangle \tag{C.16}$$

$$= \frac{1}{2} g\beta B + \frac{A_0}{4} \tag{C.17}$$

$$H_{52} = \frac{A}{2}(\hat{S}_+\hat{I}_- + \hat{S}_-\hat{I}_+) |M_s, M_I\rangle \tag{C.18}$$

$$= \frac{A}{2}[(\sqrt{(S(S+1) - M_s(M_s+1))} * \sqrt{(I(I+1) - M_I(M_I-1))}) \tag{C.19}$$

$$+ (\sqrt{(S(S+1) - M_s(M_s-1))} * \sqrt{(I(I+1) - M_I(M_I+1))}] \tag{C.20}$$

$$= \frac{A}{2}[\sqrt{(0*2)} + \sqrt{(1*3)}] \tag{C.21}$$

$$= \frac{A}{2}\sqrt{3} \tag{C.22}$$

The dimension of the Hamiltonian operator, which is always square,

is $(2S\ +\ 1) * \ (2I\ +\ 1)$. For this case, $(S = \frac{1}{2}, I = \frac{3}{2})$ yields an 8×8 matrix given below, where the input $|M_s, M_I\rangle$ states are labeled across the top horizontal row and the output $\langle M_s, M_I|$ states are labeled along the far left vertical column. Although the full matrix form is given, only the upper or lower triangular matrix is required as the off-diagonal elements with the same subscripts are simply the complex conjugates of each other ($H_{52} = H_{25}^*$).

$\lvert M_s, M_I\rangle$	$(\frac{1}{2}, \frac{3}{2})$	$(\frac{1}{2}, \frac{1}{2})$	$(\frac{1}{2}, -\frac{1}{2})$	$(\frac{1}{2}, -\frac{3}{2})$	$(-\frac{1}{2}, \frac{3}{2})$	$(-\frac{1}{2}, \frac{1}{2})$	$(-\frac{1}{2}, -\frac{1}{2})$	$(-\frac{1}{2}, -\frac{3}{2})$
$(\frac{1}{2}, \frac{3}{2})$	H_{11}							
$(\frac{1}{2}, \frac{1}{2})$		H_{22}			H_{25}			
$(\frac{1}{2}, -\frac{1}{2})$			H_{33}			H_{36}		
$(\frac{1}{2}, -\frac{3}{2})$				H_{44}			H_{47}	
$(-\frac{1}{2}, \frac{1}{2})$		H_{52}			H_{55}			
$(-\frac{1}{2}, \frac{1}{2})$			H_{63}			H_{66}		
$(-\frac{1}{2}, -\frac{3}{2})$				H_{74}			H_{77}	
$(-\frac{1}{2}, -\frac{3}{2})$								H_{88}

(C.23)

The eigenvalues of this matrix were computed in MATLAB and are shown in Table C.1.

C.2 Direct Product Method

"Wisely and slow. They stumble that run fast" [105]. The MATLAB script below calculates the symbolic spin-Hamiltonian and eigenvalues for an isotropic S = 1/2 and I = 3/2 spin system using the direct product method. This method does not require the use of raising and lowering operators and calculates all of the matrix elements of the spin Hamiltonian at once. Both methods yield the exactly the same results.

$$\begin{bmatrix} -\frac{A}{4} - \frac{\sqrt{4A^2 - 2AB\beta g + B^2\beta^2 g^2}}{2} \\ \frac{\sqrt{4A^2 - 2AB\beta g + B^2\beta^2 g^2}}{2} - \frac{A}{4} \\ -\frac{A}{4} - \frac{\sqrt{4A^2 + 2AB\beta g + B^2\beta^2 g^2}}{2} \\ \frac{\sqrt{4A^2 + 2AB\beta g + B^2\beta^2 g^2}}{2} - \frac{A}{4} \\ \frac{3A}{4} - \frac{B\beta g}{2} \\ \frac{3A}{4} + \frac{B\beta g}{2} \\ -\frac{A}{4} - \frac{\sqrt{4A^2 + B^2\beta^2 g^2}}{2} \\ \frac{\sqrt{4A^2 + B^2\beta^2 g^2}}{2} - \frac{A}{4} \end{bmatrix}$$

Table C.1. Eigenvalues of the $S = \frac{1}{2}$ $I = \frac{3}{2}$ spin Hamiltonian matrix corresponding to an $S = 1/2$ Selenium vacancy (V_{Se}^{+}) with $I = 3/2$ Ga^{+3} hyperfine interaction in $BaGa_4Se_7$

The direct product method requires significantly less algebra compared to calculating each matrix element using the raising and lowering operators, but does require an understanding of the direct product expansion process. Texts by Shankar [106], and Poole [107] both provide an excellent review of this matrix method. This Matlab code uses Easyspin functions for generating the various spin matrices and plotting the energy levels (eigenvalues) as a function of the magnetic field.

```
clc, clear

% declare symbolic variables
syms beta H A g_e

%Use EasySpin 'sop' function to generate the spin matrices

%J=1/2 matrices
I = sop(1/2,'e'); %identity (2x2)
X = sop(1/2,'x');  %(same as the Pauli x S=1/2 matrix)
Y = sop(1/2,'y'); %y spin matrix
Z = sop(1/2,'z'); %z spin matrix
```

```
13
14 %J=3/2 matrices
15 I_4 = sop(3/2,'e'); %identity (4x4)
16 X_4 = sop(3/2,'x'); %x spin matrix
17 Y_4 = sop(3/2,'y'); %y spin matrix
18 Z_4 = sop(3/2,'z'); %z spin matrix
19
20 % compute the symbolic spin Hamiltonian
21 Ham2 = beta*H*(g_e*kron(Z,I_4))+A*((kron(X,X_4)+...
22     kron(Y,Y_4)+kron(Z,Z_4)))
23
24 % compute and sort the eigenvalues of the Hamiltonian
     matrix
25 E = simplify(eig(Ham2))
26
27 % These are the eight eigenvalues/ levels of the 8x8 spin
     Hamiltonian matrix.
28 E =
29 -A/4-(4*A^2-2*A*H*beta*g_e+H^2*beta^2*g_e^2)^(1/2)/2
30 (4*A^2-2*A*H*beta*g_e+H^2*beta^2*g_e^2)^(1/2)/2-A/4
31 -A/4-(4*A^2+2*A*H*beta*g_e+H^2*beta^2*g_e^2)^(1/2)/2
32 (4*A^2+2*A*H*beta*g_e+H^2*beta^2*g_e^2)^(1/2)/2-A/4
33 (3*A)/4-(H*beta*g_e)/2
34 (3*A)/4+(H*beta*g_e)/2
35 -A/4-(4*A^2+H^2*beta^2*g_e^2)^(1/2)/2
36 (4*A^2+H^2*beta^2*g_e^2)^(1/2)/2- A/4
```

```
%%
%Use EasySpin levelsplot function to plot the eigenvalues as a function of
%magnetic field and show the EPR transitions at a given microwave
%frequency.

% Define the Spin System
Sys.S = 1/2; %Spin quantum number
Sys.g = 2; %isotropic g -value
Sys.Nucs = '69Ga'; %specify the interacting nucleus and isotope
Sys.A = 4417; %isotropic hypefine parameter in GHz

Brange = [0 700]; %magnetic field sweep range mT
mwFreq = 9.38; %micowave frequency in MHz

levelsplot(Sys,'z',Brange,mwFreq) %specify direction of B field (z)
```

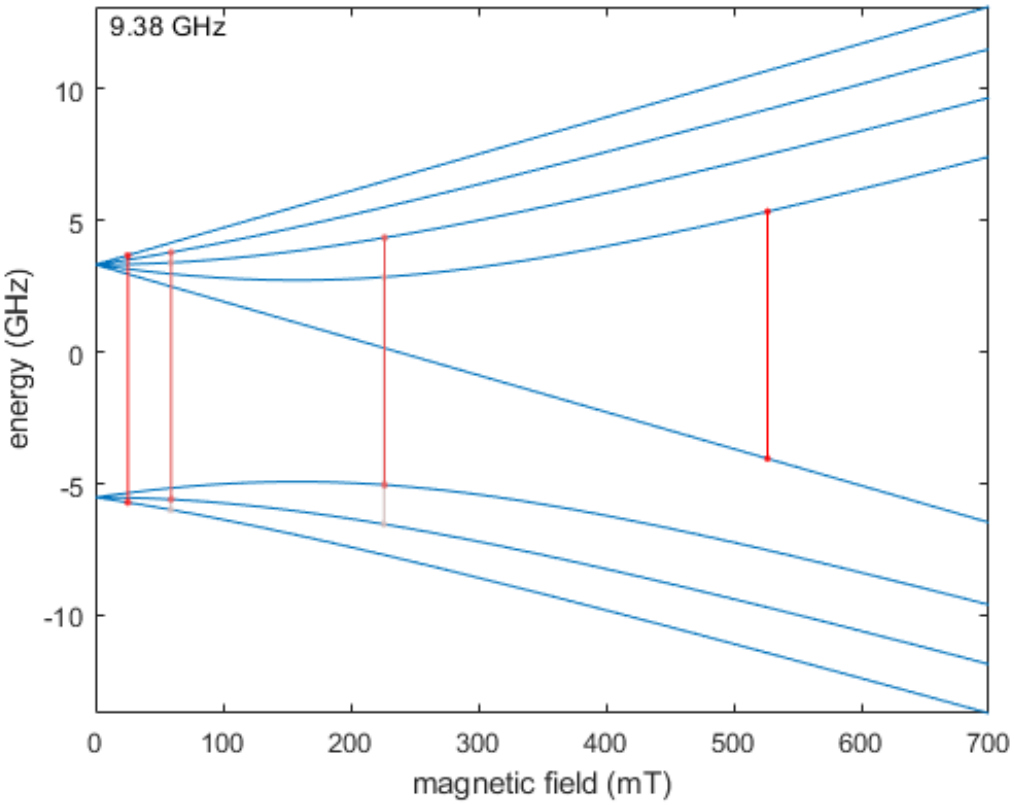

Figure C.2. Easyspin [68] energy levels plotted as a function of magnetic field for 69Ga nuclei, $I = 3/2$, in the singly ionized V_{Se}^{+}(A) vacancy, $S = 1/2$. The red vertical lines represent the four ^{69}Ga EPR transitions.

Appendix D. MATLAB Programs for the Selenium Vacancy in $BaGa_4Se_7$

D.1 Fitting Routine for g and A Parameters for the Selenium Vacancy in $BaGa_4Se_7$

This program determines the best values for the **g** and **A** parameter matrices for the selenium vacancy in $BaGa_4Se_7$. This program is used in conjunction with a second program named "SUMM BGSe Ga". The measured magnetic fields and microwave frequencies are contained in "SUMM BGSe Ga".

```
% Constants:

h = 6.62606957;                    % Planck's constant
Beta = 9.27400968/h;     % Bohr magneton divided by Planck'
   s constant
gbn = 0.001024777;                 % gn*bn for gallium 69
% gbn = 0.001302074;               % gn*bn for gallium 71

% Initial values for the parameters:

P(1) = 2.00;              % g value
P(2) = 4000;              % A value

% Step size for each parameter:

step(1) = 0.00001;        % step size for g value
step(2) = 0.01;      % step size for A value
```

```
17
18 sum2 = 0; %starting value
19 sum1 = SUMM_BGSe_Ga(P,Beta,gbn);
20
21 while sum2<sum1
22    for n = 1:2 %fits g value (n=1), then A value (n=2)
23       summ = SUMM_BGSe_Ga(P,Beta,gbn);
24       sum2 = summ;
25         if n==1
26                  sum1 = summ;
27         end
28       P(n) = P(n) + step(n); %increase parameter by step
            size
29       summ = SUMM_BGSe_Ga(P,Beta,gbn); %run function with
            updated parameter value
30         if summ >= sum2  %if new value is greater than or
              equal to the old value
31            P(n) = P(n) - 2*step(n);  %decrease previous
                 parameter value by 2 step sizes
32            summ = SUMM_BGSe_Ga(P,Beta,gbn);  %run
                 function with updated parameter value
33            if summ >= sum2
34               P(n) = P(n) + step(n);  %increase parameter
                     by step size
35               end
36          end
```

```
37        end
38        if summ<sum2
39            sum2 = summ;
40        end
41        sum2
42    end
43
44    P                       % Display final set of parameters
45    sum2                    % Display final value for sum2
46
47    % End of program
```

D.2 Least Squares Sub-routine for the Selenium Vacancy in $BaGa_4Se_7$ Crystals

This subroutine is used in conjunction with "BGSe Ga fitting" to determine best values for the **g** and **A** parameter matrices for the selenium vacancy in $BaGa_4Se_7$. It calculates a sum of the frequency differences squared and returns it to the main program. The input data are the measured magnetic fields and microwave frequencies. There are four sets of field values taken from the EPR spectrometer that correspond to V_{Se}^{+}(A), V_{Se}^{+}(B), V_{Se}^{+}(C), and V_{Se}^{+}(D) as detailed in Chapter 4. There is a correction applied to the magnetic field values read from the spectrometer that accounts for the small distance from the Hall-effect probe to the center of the resonant cavity. This correction is explained in detail in Dr. Scherrer's dissertation [37]. Each spectrum must be fit separately for each nuclei. In the MATLAB code below, the fitting is for the V_{Se}^{+}(B) spectra with the ^{69}Ga hyperfine interaction; all other field values are commented out.

```
function summ = SUMM_BGSe_Ga(P,Beta,gbn)

%The corrected magnetic field values (B') are calculated
   using Dr. Elizabeth Scherrer's dissertation equation
   3.3

%For field values below 10000 Gauss B' = 1.00229527 *B +
   0.39773306
%FRQ is the microwave frequency IC labels the EPR line(s)

% Spectrum A (69Ga)   Formed during initial 532 nm
```

```
    exposure at 35 K.
9
10 % hh(1)=5255.7*1.00229527+0.39773306;FRQ(1)=9384.501;IC(1)
    =1;
11 % hh(2)=2260.3*1.00229527+0.39773306;FRQ(2)=9384.501;IC(2)
    =2;
12 % hh(3)=600.1*1.00229527+0.39773306;FRQ(3)=9384.501;IC(3)
    =3;
13 % hh(4)=256.0*1.00229527+0.39773306;FRQ(4)=9384.501;IC(4)
    =4;
14 %
15 % hh(1)=5255.7*1.00229527+0.39773306
16 % hh(2)=2260.3*1.00229527+0.39773306
17 % hh(3)=600.1*1.00229527+0.39773306
18 % hh(4)=256.0*1.00229527+0.39773306
19
20 % Spectrum A (71Ga)
21
22 % hh(1)=5654.7*1.00229527+0.39773306;FRQ(1)=9384.501;IC(1)
    =1;
23 % hh(2)=939.1*1.00229527+0.39773306;FRQ(2)=9384.501;IC(2)
    =2;
24 %
25 % hh(1)=5654.7*1.00229527+0.39773306
26 % hh(2)=939.1*1.00229527+0.39773306
27
```

```
28 % Spectrum B (69Ga)   Formed during initial 532 nm
     exposure at 35 K.
29
30 % hh(1)=5091.7*1.00229527+0.39773306;FRQ(1)=9384.526;IC(1)
     =1;
31 % hh(2)=2540.3*1.00229527+0.39773306;FRQ(2)=9384.526;IC(2)
     =2;
32 % hh(3)=1019.1*1.00229527+0.39773306;FRQ(3)=9384.526;IC(3)
     =3;
33 % hh(4)=517.1*1.00229527+0.39773306;FRQ(4)=9384.526;IC(4)
     =4;
34 %
35 % hh(1)=5091.7*1.00229527+0.39773306
36 % hh(2)=2540.3*1.00229527+0.39773306
37 % hh(3)=1019.1*1.00229527+0.39773306
38 % hh(4)=517.1*1.00229527+0.39773306
39
40 % Spectrum B (71Ga)
41
42 % hh(1)=5468.7*1.00229527+0.39773306;FRQ(1)=9384.526;IC(1)
     =1;
43 % hh(2)=517.1*1.00229527+0.39773306;FRQ(2)=9384.526;IC(2)
     =2;
44 %
45 % hh(1)=5468.7*1.00229527+0.39773306
46 % hh(2)=517.1*1.00229527+0.39773306
```

```
47
48 % Spectrum B (69Ga) Second set of data.
49
50 hh(1)=5090.7*1.00229527+0.39773306;FRQ(1)=9384.516;IC(1)
      =1;
51 hh(2)=2545.3*1.00229527+0.39773306;FRQ(2)=9384.516;IC(2)
      =2;
52 hh(3)=1020.1*1.00229527+0.39773306;FRQ(3)=9384.516;IC(3)
      =3;
53 hh(4)=519.1*1.00229527+0.39773306;FRQ(4)=9384.516;IC(4)=4;
54
55 hh(1)=5090.7*1.00229527+0.39773306;
56 hh(2)=2545.3*1.00229527+0.39773306;
57 hh(3)=1020.1*1.00229527+0.39773306;
58 hh(4)=519.1*1.00229527+0.39773306;
59
60 % Spectrum B (71Ga) Second set of data.
61
62 % hh(1)=5466.7*1.00229527+0.39773306;FRQ(1)=9384.516;IC(1)
      =1;
63 % hh(2)=519.1*1.00229527+0.39773306;FRQ(2)=9384.516;IC(2)
      =2;
64 %
65 % hh(1)=5466.7*1.00229527+0.39773306
66 % hh(2)=519.1*1.00229527+0.39773306
67
```

```
% Spectrum C (69Ga)   Formed during heating to 90 K.

% hh(1)=5292.7*1.00229527+0.39773306;FRQ(1)=9384.516;IC(1)
   =1;
% hh(2)=288.0*1.00229527+0.39773306;FRQ(2)=9384.516;IC(2)
   =2;
%
% hh(1)=5292.7*1.00229527+0.39773306
% hh(2)=288.0*1.00229527+0.39773306

% Spectrum C (71Ga)

% hh(1)=5708.8*1.00229527+0.39773306;FRQ(1)=9384.516;IC(1)
   =1;
% hh(2)=1740.2*1.00229527+0.39773306;FRQ(2)=9384.516;IC(2)
   =2;
%
% hh(1)=5708.8*1.00229527+0.39773306
% hh(2)=1740.2*1.00229527+0.39773306

% Spectrum D (69Ga)   Formed during heating to 120 K.

% hh(1)=4966.7*1.00229527+0.39773306;FRQ(1)=9384.516;IC(1)
   =1;
% hh(2)=3170.4*1.00229527+0.39773306;FRQ(2)=9384.516;IC(2)
   =2;
```

```
88 % hh(3)=1892.2*1.00229527+0.39773306;FRQ(3)=9384.516;IC(3)
     =3;
89 % hh(4)=1126.1*1.00229527+0.39773306;FRQ(4)=9384.516;IC(4)
     =4;
90 %
91 % hh(1)=4966.7*1.00229527+0.39773306
92 % hh(2)=3170.4*1.00229527+0.39773306
93 % hh(3)=1892.2*1.00229527+0.39773306
94 % hh(4)=1126.1*1.00229527+0.39773306
95
96 % Spectrum D (71Ga)
97
98 % hh(1)=5321.7*1.00229527+0.39773306;FRQ(1)=9384.516;IC(1)
     =1;
99 % hh(2)=2641.3*1.00229527+0.39773306;FRQ(2)=9384.516;IC(2)
     =2;
100 % hh(3)=360.0*1.00229527+0.39773306;FRQ(3)=9384.516;IC(3)
     =4;
101 % %hh(4)=360.0*1.00229527+0.39773306;FRQ(4)=9384.516;IC(4)
     =4;
102 % %
103 % hh(1)=5321.7*1.00229527+0.39773306
104 % hh(2)=2641.3*1.00229527+0.39773306
105 % hh(3)=360.0*1.00229527+0.39773306
106 % %hh(4)=360.0*1.00229527+0.39773306
107
```

```
datapoints = length(hh); %four data points for the 4 lines

for n=1:datapoints
   HH = hh(n);
   ic = IC(n);

% Ham is the matrix representing the spin-Hamiltonian.

Ham = zeros(8);
Ham(1,1) = 0.5*P(1)*Beta*HH + 0.75*P(2)-1.5*gbn*HH;
Ham(2,2) = 0.5*P(1)*Beta*HH + 0.25*P(2)-0.5*gbn*HH;
Ham(3,3) = 0.5*P(1)*Beta*HH - 0.25*P(2)+0.5*gbn*HH;
Ham(4,4) = 0.5*P(1)*Beta*HH - 0.75*P(2)+1.5*gbn*HH;
Ham(5,5) = -0.5*P(1)*Beta*HH - 0.75*P(2)-1.5*gbn*HH;
Ham(6,6) = -0.5*P(1)*Beta*HH - 0.25*P(2)-0.5*gbn*HH;
Ham(7,7) = -0.5*P(1)*Beta*HH + 0.25*P(2)+0.5*gbn*HH;
Ham(8,8) = -0.5*P(1)*Beta*HH + 0.75*P(2)+1.5*gbn*HH;

Ham(5,2) = 0.5*sqrt(3)*P(2);
Ham(6,3) = P(2);
Ham(7,4) = 0.5*sqrt(3)*P(2);

Ham(2,5) = conj(Ham(5,2));
Ham(3,6) = conj(Ham(6,3));
Ham(4,7) = conj(Ham(7,4));

```

```
EE = sort(real(eig(Ham)));

if ic==1
   freq(n) = EE(5)-EE(4);

elseif ic==2
   freq(n) = EE(6)-EE(3);

elseif ic==3
   freq(n) = EE(7)-EE(2);

elseif ic==4
   freq(n) = EE(8)-EE(1);

end
end

summ=0;
for n=1:datapoints
   summ = summ + (FRQ(n)-freq(n))^2;
end
```

D.3 Line Positions of EPR Transitions for Selenium Vacancies V_{Se}^{+} in $BaGa_4Se_7$

This main program calculates EPR line positions as a function of angle, using g and A matrices, for the selenium vacancies V_{Se}^{+} in $BaGa_4Se_7$. This program uses a subroutine named "energylevels Ga".

```
clear all
clf reset

% Constants:

h = 6.62606957;                    % Planck's constant
Beta = 9.27400968/h;     % Bohr magneton divided by Planck's constant
gbn = 0.001024777;                 % gn*bn for gallium 69
% gbn = 0.001302074;               % gn*bn for gallium 71
InitialHH = 1400;                  % Initial guess for line positions (in gauss)

% Spin-Hamiltonian parameters:
% One for the g matrix and one for the A matrix.

P(1) = 2.00025;
P(2) = 4416.72;

% When the separation between two levels is increasing with increasing field, the correct ratio below is FREQQ/FREQ.
```

```
19
20 % When the separation between two levels is decreasing
     with increasing field, the correct ratio below is FREQ/
     FREQQ. This case arises for the 4-3 transition.
21
22 for n=1:91                % Angle increment is one degree.
23
24 FREQQ = 9384.501;        % Microwave frequency (in MHz).
25
26 N(n) = n-1;
27
28         for ic=1:4
29            if ic==1
30               HH = InitialHH;
31               EE = energylevels_Ga(HH,P,gbn,Beta);
32               FREQ = EE(5)-EE(4);
33                  while abs(FREQQ-FREQ)>0.1;
34                           HH = HH * (FREQQ/FREQ);
35                  EE = energylevels_Ga(HH,P,gbn,Beta);
36                           FREQ = EE(5)-EE(4);
37                end
38                MagneticField(n,1) = HH;
39
40            elseif ic==2
41               HH = InitialHH;
42               EE = energylevels_Ga(HH,P,gbn,Beta);
```

```
43              FREQ = EE(6)-EE(3);
44                 while abs(FREQQ-FREQ)>0.1;
45                         HH = HH * (FREQQ/FREQ);
46                 EE = energylevels_Ga(HH,P,gbn,Beta);
47                         FREQ = EE(6)-EE(3);
48                   end
49                   MagneticField(n,2) = HH;
50
51           elseif ic==3
52              HH = InitialHH;
53              EE = energylevels_Ga(HH,P,gbn,Beta);
54              FREQ = EE(7)-EE(2);
55                 while abs(FREQQ-FREQ)>0.1;
56                         HH = HH * (FREQQ/FREQ);
57                 EE = energylevels_Ga(HH,P,gbn,Beta);
58                         FREQ = EE(7)-EE(2);
59                   end
60                   MagneticField(n,3) = HH;
61
62           elseif ic==4
63              HH = InitialHH;
64              EE = energylevels_Ga(HH,P,gbn,Beta);
65              FREQ = EE(8)-EE(1);
66                 while abs(FREQQ-FREQ)>0.1;
67                         HH = HH * (FREQQ/FREQ);
68                 EE = energylevels_Ga(HH,P,gbn,Beta);
```

```
69                          FREQ = EE(8)-EE(1);
70                  end
71                  MagneticField(n,4) = HH;
72
73  % For the transitions below the separation between two
       levels is decreasing with increasing field, thus the
       correct ratio below is FREQ/FREQQ. This case arises for
        the 4-3 transition.
74
75  %                 elseif ic==5
76  %                 HH = InitialHH;
77  %                 EE = energylevels_Ga(HH,P,gbn,Beta);
78  %                 FREQ = EE(6)-EE(1);
79  %                           while abs(FREQQ-FREQ)>0.1;
80  %                           HH = HH * (FREQQ/FREQ);
81  %                           EE = energylevels_Ga(HH,P,gbn,Beta
       );
82  %                           FREQ = EE(6)-EE(1);
83  %                   end
84  %                   MagneticField(n,5) = HH;
85  %
86  %                   elseif ic==6
87  %                 HH = InitialHH;
88  %                 EE = energylevels_Ga(HH,P,gbn,Beta);
89  %                 FREQ = EE(8)-EE(1);
90  %                           while abs(FREQQ-FREQ)>0.1;
```

```
91 %                         HH = HH * (FREQQ/FREQ);
92 %                         EE = energylevels_Ga(HH,P,gbn,Beta
   );
93 %                         FREQ = EE(8)-EE(1);
94 %                   end
95 %                   MagneticField(n,6) = HH;
96 %
97 %                   elseif ic==7
98 %                HH = InitialHH;
99 %                EE = energylevels_Ga(HH,P,gbn,Beta);
100 %               FREQ = EE(4)-EE(3);
101 %                        while abs(FREQQ-FREQ)>0.1;
102 %                        HH = HH * (FREQQ/FREQ);
103 %                        EE = energylevels_Ga(HH,P,gbn,Beta
   );
104 %                        FREQ = EE(4)-EE(3);
105 %                   end
106 %                   MagneticField(n,7) = HH;
107
108              end
109         end
110     end
111
112 plot(N,MagneticField)
113 ylabel('Magnetic Field (gauss)')
114 xlabel('Angle (degrees)')
```

D.4 Energy Levels and Eigenvalues of the Spin Hamiltonian for the Selenium Vacancy in $BaGa_4Se_7$

This subroutine is used in conjunction with "BGSe Ga line positions". That main program determines the line positions as a function of angle for the selenium vacancy in $BaGa_4Se_7$. This subroutine calculates the eigenvalues and returns them to the main program. The spin Hamiltonian operator for the selenium vacancy in $BaGa_4Se_7$ is an 8×8 hermitian matrix with eight corresponding eigenvalues. These eigenvalues are the levels between which the unpaired spin transitions. In accordance with the selection rules detailed in chapter 4, for eight levels there are four possible transitions. These four transitions are then plotted as a function of the magnetic field.

```
function EE = energylevels_Ga(HH,P,gbn,Beta)

% Ham is the matrix representing the spin-Hamiltonian.

Ham = zeros(8);
Ham(1,1) = 0.5*P(1)*Beta*HH + 0.75*P(2)-1.5*gbn*HH;
Ham(2,2) = 0.5*P(1)*Beta*HH + 0.25*P(2)-0.5*gbn*HH;
Ham(3,3) = 0.5*P(1)*Beta*HH - 0.25*P(2)+0.5*gbn*HH;
Ham(4,4) = 0.5*P(1)*Beta*HH - 0.75*P(2)+1.5*gbn*HH;
Ham(5,5) = -0.5*P(1)*Beta*HH - 0.75*P(2)-1.5*gbn*HH;
Ham(6,6) = -0.5*P(1)*Beta*HH - 0.25*P(2)-0.5*gbn*HH;
Ham(7,7) = -0.5*P(1)*Beta*HH + 0.25*P(2)+0.5*gbn*HH;
Ham(8,8) = -0.5*P(1)*Beta*HH + 0.75*P(2)+1.5*gbn*HH;

Ham(5,2) = 0.5*sqrt(3)*P(2);
Ham(6,3) = P(2);
```

```
Ham(7,4) = 0.5*sqrt(3)*P(2);

Ham(2,5) = conj(Ham(5,2));
Ham(3,6) = conj(Ham(6,3));
Ham(4,7) = conj(Ham(7,4));

EE = sort(real(eig(Ham)));
```

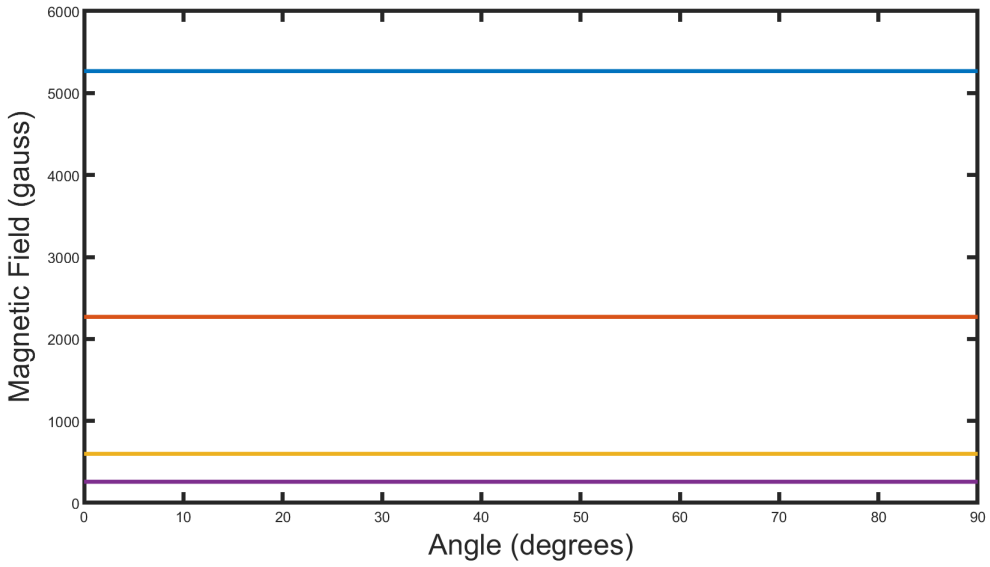

Figure D.1. Output from Line Positions MATLAB routine for selenium vacancies V_{Se}^{+} in $BaGa_4Se_7$. The four lines represent where the EPR transitions occur in the magnetic field as a function of crystal orientation. Since the g and A parameter matrices are isotropic there is no variation in line position. These four lines correspond to the V_{Se}^{+}(A) spectra presented in Chapter 4 Figure 4.3

Appendix E. MATLAB Programs for the Oxygen Vacancy in LiB_3O_5

E.1 Fitting Routine for g and A Parameters for the Oxygen Vacancy in LiB_3O_5

This program determines the best values for the **g** and **A** parameter matrices for the oxygen vacancy in LiB_3O_5. This program is used in conjunction with a second program named "SUMM LBO oxy vac BH". The measured magnetic fields and microwave frequencies are contained in "SUMM LBO oxy vac BH".

```
% Constants:

h = 6.62606957;                    % Planck's constant
B = 9.27400968/h;                  % Bohr magneton divided by
    Planck's constant
gbn = 0.001366299;                 % gn*bn for the boron 11
   isotope
CTR = pi/180;                      % Conversion constant,
   degrees to radians

% Initial values for the g and A matrix parameters; three
   principal values
% and three Euler angles for each parameter.

P(1) = 2.0000;              % g matrix
P(2) = 2.0000;
P(3) = 2.0000;
```

```
P(4) = 45*CTR;
P(5) = 45*CTR;
P(6) = 45*CTR;
P(7) = 350;              % A matrix
P(8) = 350;
P(9) = 350;
P(10) = 45*CTR;
P(11) = 45*CTR;
P(12) = 45*CTR;

% Step size for each parameter:

gg = 0.0001;                    % step size for g values
aa = 0.01;              % step size for A values
delta = 0.01*CTR;       % step size for angles

step(1) = gg;             % g matrix
step(2) = gg;             %
step(3) = gg;             %
step(4) = delta;          %
step(5) = delta;          %
step(6) = delta;          %
step(7) = aa;             % A matrix
step(8) = aa;             %
step(9) = aa;             %
step(10) = delta;         %
```

```
step(11) = delta;          %
step(12) = delta;          %

sum2 = 0;
sum1 = SUMM_LBO_oxy_vac_BH(P,B,gbn);

while sum2<sum1
   for n = 1:12
       summ = SUMM_LBO_oxy_vac_BH(P,B,gbn);
       sum2 = summ;
         if n==1;
                  sum1 = summ;
         end
       P(n) = P(n) + step(n);
       summ = SUMM_LBO_oxy_vac_BH(P,B,gbn);
         if summ >= sum2;
              P(n) = P(n) - 2*step(n);
              summ = SUMM_LBO_oxy_vac_BH(P,B,gbn);
              if summ >= sum2;
                 P(n) = P(n) + step(n);
                  end
          end
       end
       if summ<sum2;
          sum2 = summ;
       end
```

```
66        sum2
67    end
68    %convert Euler angles from radians to degrees
69    P(4) = P(4)*180/pi;
70    P(5) = P(5)*180/pi;
71    P(6) = P(6)*180/pi;
72    P(10) = P(10)*180/pi;
73    P(11) = P(11)*180/pi;
74    P(12) = P(12)*180/pi;
75
76    P                    % Display final set of parameters
77    sum2                 % Display funal value for sum2
78
79    % End of program
```

E.2 Least Squares Sub-routine for the Oxygen Vacancy in LiB_3O_5

This subroutine is used in conjunction with "LBO oxy vac fitting BH" to determine the best values for the **g** and **A** parameter matrices for the oxygen vacancy in LiB_3O_5. It calculates a sum of the frequency differences squared and returns it to the main program. The input data are the measured magnetic fields and microwave frequencies.

When the magnetic field is rotated from the b axis towards the c axis, the EPR spectrum will split into two doubly degenerate spectra [108]. In this a plane sites 1 & 2 and 3 & 4 are equivalent. The low-field spectrum may be due to sites 3 & 4, while the high-field spectrum may be due to sites 1 & 2 (corresponds to choice 1). The opposite case is also possible (corresponds to choice 2) [108]. Setzler detailed in his dissertation that this degeneracy yields two sets of spin Hamiltonian parameters that both equally fit the EPR angular dependence data along the high-symmetry a, b, and c planes, but predict different angular dependencies for non-high symmetry planes. He further details how to determine which set if assignments, and thus which set of parameters, is the correct set that agrees with the data [108]. In short, the crystal must be oriented so that the rotation is from one high symmetry direction to a point in between the two other high symmetry directions. In this case, the crystal was oriented so that the rotation performed was from the c direction to the mid-point of the ab plane. In this rotation each of the four lines are further split into an additional four lines. The first choice of parameters predicts that the high-field line will split into four lines, with three of the four lines shifting to lower field during the first half of the rotation, and that the low-field line will likewise split into four with three of the lines shifting to higher field. The second choice of parameters predicted that the high-field line will split into four lines, with three of the four shifting to higher field during the first half of the rotation, and that the low-field line will likewise split into four with three of the lines shifting to lower field. Experimentally we observed line

splitting that corresponds with the first choice of parameters when rotating from the c direction to the mid-point of the ab plane. Plots of the two predictions are shown at the end of this chapter in figures E.4 and E.5.

```
function summ = SUMM_LBO_oxy_vac_BH(P,B,gbn)

% G is the 3x3 rotation matrix which takes the principal
% axes of the g matrix into the crystal coordinate system.

% H is the 3x3 rotation matrix which takes the principal
% axes of the A matrix into the crystal coordinate system.

% RR is the 3x3 rotation matrix that takes sites 2,3,and 4
    into
%site 1 based on the point symmetry operations of the
   group.

% R is the 3x3 rotation matrix which takes the crystal
   coordinate
% system into the magnetic field coordinate system.

G(1,1) = cos(P(6))*cos(P(5)) - cos(P(4))*sin(P(5))*sin(P
   (6));
G(1,2) = cos(P(6))*sin(P(5)) + cos(P(4))*cos(P(5))*sin(P
   (6));
G(1,3) = sin(P(6))*sin(P(4));
G(2,1) = -sin(P(6))*cos(P(5)) - cos(P(4))*sin(P(5))*cos(P
```

```
   (6));
19 G(2,2) = -sin(P(6))*sin(P(5)) + cos(P(4))*cos(P(5))*cos(P
   (6));
20 G(2,3) = cos(P(6))*sin(P(4));
21 G(3,1) = sin(P(4))*sin(P(5));
22 G(3,2) = -sin(P(4))*cos(P(5));
23 G(3,3) = cos(P(4));
24
25 H(1,1) = cos(P(12))*cos(P(11)) - cos(P(10))*sin(P(11))*sin
   (P(12));
26 H(1,2) = cos(P(12))*sin(P(11)) + cos(P(10))*cos(P(11))*sin
   (P(12));
27 H(1,3) = sin(P(12))*sin(P(10));
28 H(2,1) = -sin(P(12))*cos(P(11)) - cos(P(10))*sin(P(11))*
   cos(P(12));
29 H(2,2) = -sin(P(12))*sin(P(11)) + cos(P(10))*cos(P(11))*
   cos(P(12));
30 H(2,3) = cos(P(12))*sin(P(10));
31 H(3,1) = sin(P(10))*sin(P(11));
32 H(3,2) = -sin(P(10))*cos(P(11));
33 H(3,3) = cos(P(10));
34 %%%%%%%%%%%%%%%%%%%%%%%%%%%%%%
35 %The corrected magnetic field values (B') are calculated
   using Dr. Elizabeth
36 %Scherrer's dissertation equation 3.3
37
```

```
%For field values below 10000 Gauss B' = (B * 1.00229527)
   + 0.39773306
%FRQ is the microwave frequency
%IC labels the EPR line(s)
%K labels the sites
%%%%%%%%%%%%%%%%%%%%%%%%%%%%%%%%
% Rotating from a to b

hh(1)=3144.62*1.00229527+0.39773306;FRQ(1)=9402.333;K(1)
   =1;IC(1)=1;Alpha1(1)=90;Beta1(1)=0;
hh(2)=3543.95*1.00229527+0.39773306;FRQ(2)=9402.333;K(2)
   =1;IC(2)=4;Alpha1(2)=90;Beta1(2)=0;

hh(3)=3135.61*1.00229527+0.39773306;FRQ(3)=9402.317;K(3)
   =2;IC(3)=1;Alpha1(3)=90;Beta1(3)=20;
hh(4)=3528.94*1.00229527+0.39773306;FRQ(4)=9402.317;K(4)
   =1;IC(4)=4;Alpha1(4)=90;Beta1(4)=20;
hh(5)=3161.63*1.00229527+0.39773306;FRQ(5)=9402.317;K(5)
   =1;IC(5)=1;Alpha1(5)=90;Beta1(5)=20;
hh(6)=3554.46*1.00229527+0.39773306;FRQ(6)=9402.317;K(6)
   =2;IC(6)=4;Alpha1(6)=90;Beta1(6)=20;

hh(7)=3134.61*1.00229527+0.39773306;FRQ(7)=9402.300;K(7)
   =2;IC(7)=1;Alpha1(7)=90;Beta1(7)=30;
hh(8)=3525.94*1.00229527+0.39773306;FRQ(8)=9402.300;K(8)
   =1;IC(8)=4;Alpha1(8)=90;Beta1(8)=30;
```

```
hh(9)=3163.14*1.00229527+0.39773306;FRQ(9)=9402.300;K(9)
   =1;IC(9)=1;Alpha1(9)=90;Beta1(9)=30;
hh(10)=3554.46*1.00229527+0.39773306;FRQ(10)=9402.300;K
   (10)=2;IC(10)=4;Alpha1(10)=90;Beta1(10)=30;

hh(11)=3135.11*1.00229527+0.39773306;FRQ(11)=9402.286;K
   (11)=2;IC(11)=1;Alpha1(11)=90;Beta1(11)=40;
hh(12)=3520.43*1.00229527+0.39773306;FRQ(12)=9402.286;K
   (12)=1;IC(12)=4;Alpha1(12)=90;Beta1(12)=40;
hh(13)=3168.14*1.00229527+0.39773306;FRQ(13)=9402.286;K
   (13)=1;IC(13)=1;Alpha1(13)=90;Beta1(13)=40;
hh(14)=3553.96*1.00229527+0.39773306;FRQ(14)=9402.286;K
   (14)=2;IC(14)=4;Alpha1(14)=90;Beta1(14)=40;

hh(15)=3137.11*1.00229527+0.39773306;FRQ(15)=9402.284;K
   (15)=2;IC(15)=1;Alpha1(15)=90;Beta1(15)=50;
hh(16)=3516.43*1.00229527+0.39773306;FRQ(16)=9402.284;K
   (16)=1;IC(16)=4;Alpha1(16)=90;Beta1(16)=50;
hh(17)=3174.65*1.00229527+0.39773306;FRQ(17)=9402.284;K
   (17)=1;IC(17)=1;Alpha1(17)=90;Beta1(17)=50;
hh(18)=3553.46*1.00229527+0.39773306;FRQ(18)=9402.284;K
   (18)=2;IC(18)=4;Alpha1(18)=90;Beta1(18)=50;

hh(19)=3143.12*1.00229527+0.39773306;FRQ(19)=9402.287;K
   (19)=2;IC(19)=1;Alpha1(19)=90;Beta1(19)=60;
hh(20)=3513.43*1.00229527+0.39773306;FRQ(20)=9402.287;K
```

```
    (20)=1;IC(20)=4;Alpha1(20)=90;Beta1(20)=60;
hh(21)=3175.15*1.00229527+0.39773306;FRQ(21)=9402.287;K
    (21)=1;IC(21)=1;Alpha1(21)=90;Beta1(21)=60;
hh(22)=3546.96*1.00229527+0.39773306;FRQ(22)=9402.287;K
    (22)=2;IC(22)=4;Alpha1(22)=90;Beta1(22)=60;

hh(23)=3148.12*1.00229527+0.39773306;FRQ(23)=9402.287;K
    (23)=2;IC(23)=1;Alpha1(23)=90;Beta1(23)=70;
hh(24)=3514.43*1.00229527+0.39773306;FRQ(24)=9402.287;K
    (24)=1;IC(24)=4;Alpha1(24)=90;Beta1(24)=70;
hh(25)=3173.64*1.00229527+0.39773306;FRQ(25)=9402.287;K
    (25)=1;IC(25)=1;Alpha1(25)=90;Beta1(25)=70;
hh(26)=3540.45*1.00229527+0.39773306;FRQ(26)=9402.287;K
    (26)=2;IC(26)=4;Alpha1(26)=90;Beta1(26)=70;

hh(27)=3163.14*1.00229527+0.39773306;FRQ(27)=9402.296;K
    (27)=1;IC(27)=1;Alpha1(27)=90;Beta1(27)=90;
hh(28)=3525.44*1.00229527+0.39773306;FRQ(28)=9402.296;K
    (28)=1;IC(28)=4;Alpha1(28)=90;Beta1(28)=90;

% Rotating from b to c (there are two choices for this
    plane)

% First choice

hh(29)=3161.63*1.00229527+0.39773306;FRQ(29)=9400.590;K
```

```
    (29)=1;IC(29)=1;Alpha1(29)=90;Beta1(29)=90;
86 hh(30)=3523.44*1.00229527+0.39773306;FRQ(30)=9400.590;K
    (30)=1;IC(30)=4;Alpha1(30)=90;Beta1(30)=90;
87
88 hh(31)=3154.13*1.00229527+0.39773306;FRQ(31)=9400.592;K
    (31)=1;IC(31)=1;Alpha1(31)=70;Beta1(31)=90;
89 hh(32)=3515.43*1.00229527+0.39773306;FRQ(32)=9400.592;K
    (32)=3;IC(32)=4;Alpha1(32)=70;Beta1(32)=90;
90 hh(33)=3172.64*1.00229527+0.39773306;FRQ(33)=9400.592;K
    (33)=3;IC(33)=1;Alpha1(33)=70;Beta1(33)=90;
91 hh(34)=3535.95*1.00229527+0.39773306;FRQ(34)=9400.592;K
    (34)=1;IC(34)=4;Alpha1(34)=70;Beta1(34)=90;
92
93 hh(35)=3151.13*1.00229527+0.39773306;FRQ(35)=9400.603;K
    (35)=1;IC(35)=1;Alpha1(35)=60;Beta1(35)=90;
94 hh(36)=3513.43*1.00229527+0.39773306;FRQ(36)=9400.603;K
    (36)=3;IC(36)=4;Alpha1(36)=60;Beta1(36)=90;
95 hh(37)=3174.65*1.00229527+0.39773306;FRQ(37)=9400.603;K
    (37)=3;IC(37)=1;Alpha1(37)=60;Beta1(37)=90;
96 hh(38)=3539.45*1.00229527+0.39773306;FRQ(38)=9400.603;K
    (38)=1;IC(38)=4;Alpha1(38)=60;Beta1(38)=90;
97
98 hh(39)=3150.13*1.00229527+0.39773306;FRQ(39)=9400.619;K
    (39)=1;IC(39)=1;Alpha1(39)=50;Beta1(39)=90;
99 hh(40)=3514.43*1.00229527+0.39773306;FRQ(40)=9400.619;K
    (40)=3;IC(40)=4;Alpha1(40)=50;Beta1(40)=90;
```

```
100 hh(41)=3174.65*1.00229527+0.39773306;FRQ(41)=9400.619;K
       (41)=3;IC(41)=1;Alpha1(41)=50;Beta1(41)=90;
101 hh(42)=3537.45*1.00229527+0.39773306;FRQ(42)=9400.619;K
       (42)=1;IC(42)=4;Alpha1(42)=50;Beta1(42)=90;
102
103 hh(43)=3147.62*1.00229527+0.39773306;FRQ(43)=9400.633;K
       (43)=1;IC(43)=1;Alpha1(43)=40;Beta1(43)=90;
104 hh(44)=3512.93*1.00229527+0.39773306;FRQ(44)=9400.633;K
       (44)=3;IC(44)=4;Alpha1(44)=40;Beta1(44)=90;
105 hh(45)=3175.15*1.00229527+0.39773306;FRQ(45)=9400.633;K
       (45)=3;IC(45)=1;Alpha1(45)=40;Beta1(45)=90;
106 hh(46)=3538.95*1.00229527+0.39773306;FRQ(46)=9400.633;K
       (46)=1;IC(46)=4;Alpha1(46)=40;Beta1(46)=90;
107
108 hh(47)=3149.12*1.00229527+0.39773306;FRQ(47)=9400.637;K
       (47)=1;IC(47)=1;Alpha1(47)=30;Beta1(47)=90;
109 hh(48)=3514.43*1.00229527+0.39773306;FRQ(48)=9400.637;K
       (48)=3;IC(48)=4;Alpha1(48)=30;Beta1(48)=90;
110 hh(49)=3172.14*1.00229527+0.39773306;FRQ(49)=9400.637;K
       (49)=3;IC(49)=1;Alpha1(49)=30;Beta1(49)=90;
111 hh(50)=3537.95*1.00229527+0.39773306;FRQ(50)=9400.637;K
       (50)=1;IC(50)=4;Alpha1(50)=30;Beta1(50)=90;
112
113 hh(51)=3149.12*1.00229527+0.39773306;FRQ(51)=9400.636;K
       (51)=1;IC(51)=1;Alpha1(51)=20;Beta1(51)=90;
114 hh(52)=3516.43*1.00229527+0.39773306;FRQ(52)=9400.636;K
```

```
    (52)=3;IC(52)=4;Alpha1(52)=20;Beta1(52)=90;
115 hh(53)=3170.14*1.00229527+0.39773306;FRQ(53)=9400.636;K
    (53)=3;IC(53)=1;Alpha1(53)=20;Beta1(53)=90;
116 hh(54)=3535.95*1.00229527+0.39773306;FRQ(54)=9400.636;K
    (54)=1;IC(54)=4;Alpha1(54)=20;Beta1(54)=90;
117
118 hh(55)=3160.13*1.00229527+0.39773306;FRQ(55)=9400.682;K
    (55)=1;IC(55)=1;Alpha1(55)=0;Beta1(55)=90;
119 hh(56)=3526.44*1.00229527+0.39773306;FRQ(56)=9400.682;K
    (56)=1;IC(56)=4;Alpha1(56)=0;Beta1(56)=90;
120
121 % Rotating from b to c
122
123 % Second choice
124
125 % hh(29)=3161.63*1.00229527+0.39773306;FRQ(29)=9400.590;K
    (29)=1;IC(29)=1;Alpha1(29)=90;Beta1(29)=90;
126 % hh(30)=3523.44*1.00229527+0.39773306;FRQ(30)=9400.590;K
    (30)=1;IC(30)=4;Alpha1(30)=90;Beta1(30)=90;
127 %
128 % hh(31)=3154.13*1.00229527+0.39773306;FRQ(31)=9400.592;K
    (31)=3;IC(31)=1;Alpha1(31)=70;Beta1(31)=90;
129 % hh(32)=3515.43*1.00229527+0.39773306;FRQ(32)=9400.592;K
    (32)=1;IC(32)=4;Alpha1(32)=70;Beta1(32)=90;
130 % hh(33)=3172.64*1.00229527+0.39773306;FRQ(33)=9400.592;K
    (33)=1;IC(33)=1;Alpha1(33)=70;Beta1(33)=90;
```

```
131 % hh(34)=3535.95*1.00229527+0.39773306;FRQ(34)=9400.592;K
      (34)=3;IC(34)=4;Alpha1(34)=70;Beta1(34)=90;
132 %
133 % hh(35)=3151.13*1.00229527+0.39773306;FRQ(35)=9400.603;K
      (35)=3;IC(35)=1;Alpha1(35)=60;Beta1(35)=90;
134 % hh(36)=3513.43*1.00229527+0.39773306;FRQ(36)=9400.603;K
      (36)=1;IC(36)=4;Alpha1(36)=60;Beta1(36)=90;
135 % hh(37)=3174.65*1.00229527+0.39773306;FRQ(37)=9400.603;K
      (37)=1;IC(37)=1;Alpha1(37)=60;Beta1(37)=90;
136 % hh(38)=3539.45*1.00229527+0.39773306;FRQ(38)=9400.603;K
      (38)=3;IC(38)=4;Alpha1(38)=60;Beta1(38)=90;
137 %
138 % hh(39)=3150.13*1.00229527+0.39773306;FRQ(39)=9400.619;K
      (39)=3;IC(39)=1;Alpha1(39)=50;Beta1(39)=90;
139 % hh(40)=3514.43*1.00229527+0.39773306;FRQ(40)=9400.619;K
      (40)=1;IC(40)=4;Alpha1(40)=50;Beta1(40)=90;
140 % hh(41)=3174.65*1.00229527+0.39773306;FRQ(41)=9400.619;K
      (41)=1;IC(41)=1;Alpha1(41)=50;Beta1(41)=90;
141 % hh(42)=3537.45*1.00229527+0.39773306;FRQ(42)=9400.619;K
      (42)=3;IC(42)=4;Alpha1(42)=50;Beta1(42)=90;
142 %
143 % hh(43)=3147.62*1.00229527+0.39773306;FRQ(43)=9400.633;K
      (43)=3;IC(43)=1;Alpha1(43)=40;Beta1(43)=90;
144 % hh(44)=3512.93*1.00229527+0.39773306;FRQ(44)=9400.633;K
      (44)=1;IC(44)=4;Alpha1(44)=40;Beta1(44)=90;
145 % hh(45)=3175.15*1.00229527+0.39773306;FRQ(45)=9400.633;K
```

```
    (45)=1;IC(45)=1;Alpha1(45)=40;Beta1(45)=90;
146 % hh(46)=3538.95*1.00229527+0.39773306;FRQ(46)=9400.633;K
    (46)=3;IC(46)=4;Alpha1(46)=40;Beta1(46)=90;
147 %
148 % hh(47)=3149.12*1.00229527+0.39773306;FRQ(47)=9400.637;K
    (47)=3;IC(47)=1;Alpha1(47)=30;Beta1(47)=90;
149 % hh(48)=3514.43*1.00229527+0.39773306;FRQ(48)=9400.637;K
    (48)=1;IC(48)=4;Alpha1(48)=30;Beta1(48)=90;
150 % hh(49)=3172.14*1.00229527+0.39773306;FRQ(49)=9400.637;K
    (49)=1;IC(49)=1;Alpha1(49)=30;Beta1(49)=90;
151 % hh(50)=3537.95*1.00229527+0.39773306;FRQ(50)=9400.637;K
    (50)=3;IC(50)=4;Alpha1(50)=30;Beta1(50)=90;
152 %
153 % hh(51)=3149.12*1.00229527+0.39773306;FRQ(51)=9400.636;K
    (51)=3;IC(51)=1;Alpha1(51)=20;Beta1(51)=90;
154 % hh(52)=3516.43*1.00229527+0.39773306;FRQ(52)=9400.636;K
    (52)=1;IC(52)=4;Alpha1(52)=20;Beta1(52)=90;
155 % hh(53)=3170.14*1.00229527+0.39773306;FRQ(53)=9400.636;K
    (53)=1;IC(53)=1;Alpha1(53)=20;Beta1(53)=90;
156 % hh(54)=3535.95*1.00229527+0.39773306;FRQ(54)=9400.636;K
    (54)=3;IC(54)=4;Alpha1(54)=20;Beta1(54)=90;
157 %
158 % hh(55)=3160.13*1.00229527+0.39773306;FRQ(55)=9400.682;K
    (55)=1;IC(55)=1;Alpha1(55)=0;Beta1(55)=90;
159 % hh(56)=3526.44*1.00229527+0.39773306;FRQ(56)=9400.682;K
    (56)=1;IC(56)=4;Alpha1(56)=0;Beta1(56)=90;
```

```
160
161 % Rotating from c to a
162
163 hh(57)=3159.59*1.00229527+0.39773306;FRQ(57)=9395.581;K
      (57)=1;IC(57)=1;Alpha1(57)=0;Beta1(57)=0;
164 hh(58)=3525.90*1.00229527+0.39773306;FRQ(58)=9395.581;K
      (58)=1;IC(58)=4;Alpha1(58)=0;Beta1(58)=0;
165
166 hh(59)=3145.08*1.00229527+0.39773306;FRQ(59)=9395.563;K
      (59)=2;IC(59)=1;Alpha1(59)=20;Beta1(59)=0;
167 hh(60)=3513.89*1.00229527+0.39773306;FRQ(60)=9395.563;K
      (60)=1;IC(60)=4;Alpha1(60)=20;Beta1(60)=0;
168 hh(61)=3171.10*1.00229527+0.39773306;FRQ(61)=9395.563;K
      (61)=1;IC(61)=1;Alpha1(61)=20;Beta1(61)=0;
169 hh(62)=3542.41*1.00229527+0.39773306;FRQ(62)=9395.563;K
      (62)=2;IC(62)=4;Alpha1(62)=20;Beta1(62)=0;
170
171 hh(63)=3139.57*1.00229527+0.39773306;FRQ(63)=9395.489;K
      (63)=2;IC(63)=1;Alpha1(63)=30;Beta1(63)=0;
172 hh(64)=3510.88*1.00229527+0.39773306;FRQ(64)=9395.489;K
      (64)=1;IC(64)=4;Alpha1(64)=30;Beta1(64)=0;
173 hh(65)=3172.60*1.00229527+0.39773306;FRQ(65)=9395.489;K
      (65)=1;IC(65)=1;Alpha1(65)=30;Beta1(65)=0;
174 hh(66)=3546.91*1.00229527+0.39773306;FRQ(66)=9395.489;K
      (66)=2;IC(66)=4;Alpha1(66)=30;Beta1(66)=0;
175
```

```
176 hh(67)=3136.07*1.00229527+0.39773306;FRQ(67)=9395.178;K
    (67)=2;IC(67)=1;Alpha1(67)=40;Beta1(67)=0;
177 hh(68)=3511.88*1.00229527+0.39773306;FRQ(68)=9395.178;K
    (68)=1;IC(68)=4;Alpha1(68)=40;Beta1(68)=0;
178 hh(69)=3173.60*1.00229527+0.39773306;FRQ(69)=9395.178;K
    (69)=1;IC(69)=1;Alpha1(69)=40;Beta1(69)=0;
179 hh(70)=3551.42*1.00229527+0.39773306;FRQ(70)=9395.178;K
    (70)=2;IC(70)=4;Alpha1(70)=40;Beta1(70)=0;
180
181 hh(71)=3133.57*1.00229527+0.39773306;FRQ(71)=9395.624;K
    (71)=2;IC(71)=1;Alpha1(71)=50;Beta1(71)=0;
182 hh(72)=3515.39*1.00229527+0.39773306;FRQ(72)=9395.624;K
    (72)=1;IC(72)=4;Alpha1(72)=50;Beta1(72)=0;
183 hh(73)=3169.60*1.00229527+0.39773306;FRQ(73)=9395.624;K
    (73)=1;IC(73)=1;Alpha1(73)=50;Beta1(73)=0;
184 hh(74)=3555.42*1.00229527+0.39773306;FRQ(74)=9395.624;K
    (74)=2;IC(74)=4;Alpha1(74)=50;Beta1(74)=0;
185
186 hh(75)=3132.57*1.00229527+0.39773306;FRQ(75)=9395.606;K
    (75)=2;IC(75)=1;Alpha1(75)=60;Beta1(75)=0;
187 hh(76)=3519.89*1.00229527+0.39773306;FRQ(76)=9395.606;K
    (76)=1;IC(76)=4;Alpha1(76)=60;Beta1(76)=0;
188 hh(77)=3164.60*1.00229527+0.39773306;FRQ(77)=9395.606;K
    (77)=1;IC(77)=1;Alpha1(77)=60;Beta1(77)=0;
189 hh(78)=3555.92*1.00229527+0.39773306;FRQ(78)=9395.606;K
    (78)=2;IC(78)=4;Alpha1(78)=60;Beta1(78)=0;
```

```
190
191 hh(79)=3134.07*1.00229527+0.39773306;FRQ(79)=9395.599;K
       (79)=2;IC(79)=1;Alpha1(79)=70;Beta1(79)=0;
192 hh(80)=3524.90*1.00229527+0.39773306;FRQ(80)=9395.599;K
       (80)=1;IC(80)=4;Alpha1(80)=70;Beta1(80)=0;
193 hh(81)=3159.09*1.00229527+0.39773306;FRQ(81)=9395.599;K
       (81)=1;IC(81)=1;Alpha1(81)=70;Beta1(81)=0;
194 hh(82)=3555.42*1.00229527+0.39773306;FRQ(82)=9395.599;K
       (82)=2;IC(82)=4;Alpha1(82)=70;Beta1(82)=0;
195
196 hh(83)=3143.58*1.00229527+0.39773306;FRQ(83)=9395.578;K
       (83)=1;IC(83)=1;Alpha1(83)=90;Beta1(83)=0;
197 hh(84)=3543.91*1.00229527+0.39773306;FRQ(84)=9395.578;K
       (84)=1;IC(84)=4;Alpha1(84)=90;Beta1(84)=0;
198
199 datapoints = length(hh);
200
201 for n=1:datapoints
202    HH = hh(n);
203    k = K(n);
204    ic = IC(n);
205    Alpha = Alpha1(n)*pi/180;
206    Beta = Beta1(n)*pi/180;
207
208     R(1,1) = cos(Alpha)*cos(Beta);
209     R(1,2) = -sin(Beta);
```

```
210     R(1,3) = sin(Alpha)*cos(Beta);
211     R(2,1) = cos(Alpha)*sin(Beta);
212     R(2,2) = cos(Beta);
213     R(2,3) = sin(Alpha)*sin(Beta);
214     R(3,1) = -sin(Alpha);
215     R(3,2) = 0;
216     R(3,3) = cos(Alpha);
217
218     if k==1          % Site 1 (the unit matrix)
219
220         RR(1,1) = 1;RR(1,2) = 0;RR(1,3) = 0;
221         RR(2,1) = 0;RR(2,2) = 1;RR(2,3) = 0;
222         RR(3,1) = 0;RR(3,2) = 0;RR(3,3) = 1;
223
224     elseif k==2      % Site 2 (reflection in a plane)
225         %transformation from site 1 to site 2; 1st glide
               plane
226
227         RR(1,1) = -1;RR(1,2) = 0;RR(1,3) = 0;
228         RR(2,1) = 0;RR(2,2) = 1;RR(2,3) = 0;
229         RR(3,1) = 0;RR(3,2) = 0;RR(3,3) = 1;
230
231     elseif k==3      % Site 3 (reflection in b plane)
232         %transformation from site 1 to site 3; 2nd glide
               plane
233
```

```
234         RR(1,1) = 1;RR(1,2) = 0;RR(1,3) = 0;
235         RR(2,1) = 0;RR(2,2) = -1;RR(2,3) = 0;
236         RR(3,1) = 0;RR(3,2) = 0;RR(3,3) = 1;
237
238     elseif k==4     % Site 4 (reflection in a and b plane)
239         %transformation from site 1 to site 4; screw axis
240
241         RR(1,1) = -1;RR(1,2) = 0;RR(1,3) = 0;
242         RR(2,1) = 0;RR(2,2) = -1;RR(2,3) = 0;
243         RR(3,1) = 0;RR(3,2) = 0;RR(3,3) = 1;
244
245     end
246
247     R1 = RR * R;
248     TG = G * R1;
249     TH = H * R1;
250
251 W1 = B*HH*(P(1)*TG(1,1)*TG(1,3)+P(2)*TG(2,1)*TG(2,3)+P(3)*
       TG(3,1)*TG(3,3));
252 W2 = B*HH*(P(1)*TG(1,2)*TG(1,3)+P(2)*TG(2,2)*TG(2,3)+P(3)*
       TG(3,2)*TG(3,3));
253 W3 = B*HH*(P(1)*TG(1,3)*TG(1,3)+P(2)*TG(2,3)*TG(2,3)+P(3)*
       TG(3,3)*TG(3,3));
254 W4 = P(7)*TH(1,1)*TH(1,1)+P(8)*TH(2,1)*TH(2,1)+P(9)*TH
       (3,1)*TH(3,1);
255 W5 = P(7)*TH(1,1)*TH(1,2)+P(8)*TH(2,1)*TH(2,2)+P(9)*TH
```

```
    (3,1)*TH(3,2);
256 W6 = P(7)*TH(1,1)*TH(1,3)+P(8)*TH(2,1)*TH(2,3)+P(9)*TH
    (3,1)*TH(3,3);
257 W7 = P(7)*TH(1,2)*TH(1,2)+P(8)*TH(2,2)*TH(2,2)+P(9)*TH
    (3,2)*TH(3,2);
258 W8 = P(7)*TH(1,2)*TH(1,3)+P(8)*TH(2,2)*TH(2,3)+P(9)*TH
    (3,2)*TH(3,3);
259 W9 = P(7)*TH(1,3)*TH(1,3)+P(8)*TH(2,3)*TH(2,3)+P(9)*TH
    (3,3)*TH(3,3);
260
261 Q1 = 0.5*(W1+i*W2);
262 Q2 = 0.25*(W4-W7)+0.5*i*W5;
263 Q3 = 0.25*(W4+W7);
264 Q4 = 0.5*(W6+i*W8);
265
266 % Ham is the matrix representing the spin-Hamiltonian:
267
268 Ham = zeros(8);
269 Ham(1,1) = 0.5*W3 + 0.75*W9 - 1.5*gbn*HH;
270 Ham(2,2) = 0.5*W3 + 0.25*W9 - 0.5*gbn*HH;
271 Ham(3,3) = 0.5*W3 - 0.25*W9 + 0.5*gbn*HH;
272 Ham(4,4) = 0.5*W3 - 0.75*W9 + 1.5*gbn*HH;
273 Ham(5,5) = -0.5*W3 - 0.75*W9 - 1.5*gbn*HH;
274 Ham(6,6) = -0.5*W3 - 0.25*W9 - 0.5*gbn*HH;
275 Ham(7,7) = -0.5*W3 + 0.25*W9 + 0.5*gbn*HH;
276 Ham(8,8) = -0.5*W3 + 0.75*W9 + 1.5*gbn*HH;
```

```
277
278 Ham(2,1) = 0.5*sqrt(3)*Q4;
279 Ham(3,2) = Q4;
280 Ham(4,3) = 0.5*sqrt(3)*Q4;
281 Ham(5,1) = Q1 + 1.5*Q4;
282 Ham(5,2) = sqrt(3)*Q3;
283 Ham(6,1) = sqrt(3)*Q2;
284 Ham(6,2) = Q1 + 0.5*Q4;
285 Ham(6,3) = 2*Q3;
286 Ham(6,5) = -0.5*sqrt(3)*Q4;
287 Ham(7,2) = 2*Q2;
288 Ham(7,3) = Q1 - 0.5*Q4;
289 Ham(7,4) = sqrt(3)*Q3;
290 Ham(7,6) = -Q4;
291 Ham(8,3) = sqrt(3)*Q2;
292 Ham(8,4) = Q1 - 1.5*Q4;
293 Ham(8,7) = -0.5*sqrt(3)*Q4;
294
295 Ham(1,2) = conj(Ham(2,1));
296 Ham(2,3) = conj(Ham(3,2));
297 Ham(3,4) = conj(Ham(4,3));
298 Ham(1,5) = conj(Ham(5,1));
299 Ham(2,5) = conj(Ham(5,2));
300 Ham(1,6) = conj(Ham(6,1));
301 Ham(2,6) = conj(Ham(6,2));
302 Ham(3,6) = conj(Ham(6,3));
```

```
303 Ham(5,6) = conj(Ham(6,5));
304 Ham(2,7) = conj(Ham(7,2));
305 Ham(3,7) = conj(Ham(7,3));
306 Ham(4,7) = conj(Ham(7,4));
307 Ham(6,7) = conj(Ham(7,6));
308 Ham(3,8) = conj(Ham(8,3));
309 Ham(4,8) = conj(Ham(8,4));
310 Ham(7,8) = conj(Ham(8,7));
311
312 EE = sort(real(eig(Ham)));
313
314 if ic==1
315    freq(n) = EE(8)-EE(1);
316
317 elseif ic==2
318    freq(n) = EE(7)-EE(2);
319
320 elseif ic==3
321    freq(n) = EE(6)-EE(3);
322
323 elseif ic==4
324    freq(n) = EE(5)-EE(4);
325
326 end
327 end
328
```

```
329 summ=0;
330 for n=1:datapoints
331     summ = summ + (FRQ(n)-freq(n))^2;
332 end
```

E.3 Line Positions of EPR Transitions for Oxygen Vacancies in LiB_3O_5

This program calculates the angular dependence of the EPR spectrum from oxygen vacancies in LiB_3O_5. The **g** and **A** parameter matrices are used. This program is used in conjunction with a second program named "EnergyLevels oxy vac BH".

```
% Constants:

h = 6.626069;                       % Planck's constant
B = 9.274009/h;                     % Bohr magneton divided by
    Planck's constant
gbn = 0.001366298;                  % gn*bn for boron 11
   nucleus
CTR = pi/180;                       % Conversion constant,
   degrees to radians
FREQQ = 9395.5;                 % Measured microwave frequency
    (in MHz)
InitialHH = 3300;                   % Initial guess for line
   positions (in gauss)

% Spin-Hamiltonian parameters:
% Six for the g matrix (three principal values and three
   angles).
% Six for the A matrix (three principal values and three
   angles).

% First choice (best fit to out-of-plane data)

```

```
P(1) = 2.0016;
P(2) = 2.0007;
P(3) = 2.0017;
P(4) = 36.03*CTR;
P(5) = 77.54*CTR;
P(6) = 19.74*CTR;
P(7) = 317.39;
P(8) = 415.82;
P(9) = 314.69;
P(10) = 45.32*CTR;
P(11) = 2.22*CTR;
P(12) = 45.65*CTR;

% Second choice

% P(1) = 2.001900000005771;
% P(2) = 2.000800000005593;
% P(3) = 2.001200000005773;
% P(4) = 133.3099999999945*CTR;
% P(5) = -19.619999999999322*CTR;
% P(6) = 51.969999999999565*CTR;
% P(7) = 2.792500000000871e+02;
% P(8) = 4.009399999999764e+02;
% P(9) = 3.659500000000082e+02;
% P(10) = 47.229999999999855*CTR;
% P(11) = 4.930000000001176*CTR;
```

```
42 % P(12) = 56.259999999999302*CTR;
43
44 % G is the 3x3 rotation matrix which takes the principal
45 % axes of the g matrix into the crystal coordinate system.
46 % [From "Classical Mechanics, 2nd ed." by Goldstein, pp.
     146-147.]
47
48 % H is the 3x3 rotation matrix which takes the principal
49 % axes of the A matrix into the crystal coordinate system.
50
51 % RR is the 3x3 rotation matrix that takes sites 2, 3, and
      4 into site 1.
52
53 % R is the 3x3 rotation matrix which takes the crystal
     coordinate
54 % system into the magnetic field coordinate system.
55
56         G(1,1) = cos(P(6))*cos(P(5)) - cos(P(4))*sin(P(5))
              *sin(P(6));
57         G(1,2) = cos(P(6))*sin(P(5)) + cos(P(4))*cos(P(5))
              *sin(P(6));
58         G(1,3) = sin(P(6))*sin(P(4));
59         G(2,1) = -sin(P(6))*cos(P(5)) - cos(P(4))*sin(P(5)
              )*cos(P(6));
60         G(2,2) = -sin(P(6))*sin(P(5)) + cos(P(4))*cos(P(5)
              )*cos(P(6));
```

```
61          G(2,3) = cos(P(6))*sin(P(4));
62          G(3,1) = sin(P(4))*sin(P(5));
63          G(3,2) = -sin(P(4))*cos(P(5));
64          G(3,3) = cos(P(4));
65
66          H(1,1) = cos(P(12))*cos(P(11)) - cos(P(10))*sin(P
               (11))*sin(P(12));
67          H(1,2) = cos(P(12))*sin(P(11)) + cos(P(10))*cos(P
               (11))*sin(P(12));
68          H(1,3) = sin(P(12))*sin(P(10));
69          H(2,1) = -sin(P(12))*cos(P(11)) - cos(P(10))*sin(P
               (11))*cos(P(12));
70          H(2,2) = -sin(P(12))*sin(P(11)) + cos(P(10))*cos(P
               (11))*cos(P(12));
71          H(2,3) = cos(P(12))*sin(P(10));
72          H(3,1) = sin(P(10))*sin(P(11));
73          H(3,2) = -sin(P(10))*cos(P(11));
74          H(3,3) = cos(P(10));
75
76  % Select a plane of rotation before running the program.
77
78  % Plane = 1 corresponds to rotation from a to b.
79  % Plane = 2 corresponds to rotation from b to c.
80  % Plane = 3 corresponds to rotation from c to a.
81  % Plane = 4 corresponds to rotation from c to the midpoint
        of a and b.
```

```
82
83 % Enter the number below for the plane to be used.
84
85 Plane = 4;
86
87 if Plane==1              %  Rotation from a to b.
88
89 FREQQ = 9402.3;              % Measured microwave frequency
       (in MHz)
90
91 for n=1:91               %  Field direction increment is
      one degree.
92     Alpha = 90*CTR;
93     Beta = (n-1)*CTR;
94     N(n) = n-1;
95
96     R(1,1) = cos(Alpha)*cos(Beta);
97     R(1,2) = -sin(Beta);
98     R(1,3) = sin(Alpha)*cos(Beta);
99     R(2,1) = cos(Alpha)*sin(Beta);
100    R(2,2) = cos(Beta);
101    R(2,3) = sin(Alpha)*sin(Beta);
102    R(3,1) = -sin(Alpha);
103    R(3,2) = 0;
104    R(3,3) = cos(Alpha);
105
```

```
106     for k=1:4
107
108     if k==1          % Site 1
109         RR(1,1) = 1;RR(1,2) = 0;RR(1,3) = 0;
110         RR(2,1) = 0;RR(2,2) = 1;RR(2,3) = 0;
111         RR(3,1) = 0;RR(3,2) = 0;RR(3,3) = 1;
112
113     elseif k==2      % Site 2 (reflection in a plane)
114         RR(1,1) = -1;RR(1,2) = 0;RR(1,3) = 0;
115         RR(2,1) = 0;RR(2,2) = 1;RR(2,3) = 0;
116         RR(3,1) = 0;RR(3,2) = 0;RR(3,3) = 1;
117
118     elseif k==3      % Site 3 (reflection in b plane)
119         RR(1,1) = 1;RR(1,2) = 0;RR(1,3) = 0;
120         RR(2,1) = 0;RR(2,2) = -1;RR(2,3) = 0;
121         RR(3,1) = 0;RR(3,2) = 0;RR(3,3) = 1;
122
123     elseif k==4      % Site 4 (reflection in a and b planes
          )
124         RR(1,1) = -1;RR(1,2) = 0;RR(1,3) = 0;
125         RR(2,1) = 0;RR(2,2) = -1;RR(2,3) = 0;
126         RR(3,1) = 0;RR(3,2) = 0;RR(3,3) = 1;
127
128     end
129
130     R1 = RR * R;
```

```
131     TG = G * R1;
132     TH = H * R1;
133
134        for ic=1:4
135
136           if ic==1
137              HH = InitialHH;
138              EE = EnergyLevels_oxy_vac(TG,TH,HH,P,B,gbn);
139              FREQ = EE(8)-EE(1);
140                while abs(FREQQ-FREQ)>1;
141                         HH = HH * (FREQQ/FREQ);
142                         EE = EnergyLevels_oxy_vac(TG,TH,HH
                               ,P,B,gbn);
143                         FREQ = EE(8)-EE(1);
144                end
145              MagneticField(n,k) = HH;
146
147           elseif ic==2
148              HH = InitialHH;
149              EE = EnergyLevels_oxy_vac(TG,TH,HH,P,B,gbn);
150              FREQ = EE(7)-EE(2);
151                while abs(FREQQ-FREQ)>1;
152                         HH = HH * (FREQQ/FREQ);
153                         EE = EnergyLevels_oxy_vac(TG,TH,HH
                               ,P,B,gbn);
154                         FREQ = EE(7)-EE(2);
```

```
155                 end
156             MagneticField(n,k+4) = HH;
157
158         elseif ic==3
159             HH = InitialHH;
160             EE = EnergyLevels_oxy_vac(TG,TH,HH,P,B,gbn);
161             FREQ = EE(6)-EE(3);
162               while abs(FREQQ-FREQ)>1;
163                         HH = HH * (FREQQ/FREQ);
164                         EE = EnergyLevels_oxy_vac(TG,TH,HH
                               ,P,B,gbn);
165                         FREQ = EE(6)-EE(3);
166               end
167             MagneticField(n,k+8) = HH;
168
169         elseif ic==4
170             HH = InitialHH;
171             EE = EnergyLevels_oxy_vac(TG,TH,HH,P,B,gbn);
172             FREQ = EE(5)-EE(4);
173               while abs(FREQQ-FREQ)>1;
174                         HH = HH * (FREQQ/FREQ);
175                         EE = EnergyLevels_oxy_vac(TG,TH,HH
                               ,P,B,gbn);
176                         FREQ = EE(5)-EE(4);
177               end
178             MagneticField(n,k+12) = HH;
```

```
179
180             end
181         end
182     end
183 end
184
185 elseif Plane==2          %  Rotation from b to c.
186
187 FREQQ = 9400.6;              % Measured microwave frequency
        (in MHz)
188
189 for n=1:91               %  Field direction increment is
       one degree.
190     Alpha = (91-n)*CTR;
191     Beta = 90*CTR;
192     N(n) = n-1;
193
194     R(1,1) = cos(Alpha)*cos(Beta);
195     R(1,2) = -sin(Beta);
196     R(1,3) = sin(Alpha)*cos(Beta);
197     R(2,1) = cos(Alpha)*sin(Beta);
198     R(2,2) = cos(Beta);
199     R(2,3) = sin(Alpha)*sin(Beta);
200     R(3,1) = -sin(Alpha);
201     R(3,2) = 0;
202     R(3,3) = cos(Alpha);
```

```
203
204     for k=1:4
205
206     if k==1          % Site 1
207         RR(1,1) = 1;RR(1,2) = 0;RR(1,3) = 0;
208         RR(2,1) = 0;RR(2,2) = 1;RR(2,3) = 0;
209         RR(3,1) = 0;RR(3,2) = 0;RR(3,3) = 1;
210
211     elseif k==2      % Site 2 (reflection in a plane)
212         RR(1,1) = -1;RR(1,2) = 0;RR(1,3) = 0;
213         RR(2,1) = 0;RR(2,2) = 1;RR(2,3) = 0;
214         RR(3,1) = 0;RR(3,2) = 0;RR(3,3) = 1;
215
216     elseif k==3      % Site 3 (reflection in b plane)
217         RR(1,1) = 1;RR(1,2) = 0;RR(1,3) = 0;
218         RR(2,1) = 0;RR(2,2) = -1;RR(2,3) = 0;
219         RR(3,1) = 0;RR(3,2) = 0;RR(3,3) = 1;
220
221     elseif k==4      % Site 4 (reflection in a and b planes
        )
222         RR(1,1) = -1;RR(1,2) = 0;RR(1,3) = 0;
223         RR(2,1) = 0;RR(2,2) = -1;RR(2,3) = 0;
224         RR(3,1) = 0;RR(3,2) = 0;RR(3,3) = 1;
225
226     end
227
```

```
228     R1 = RR * R;
229     TG = G * R1;
230     TH = H * R1;
231
232        for ic=1:4
233
234           if ic==1
235              HH = InitialHH;
236              EE = EnergyLevels_oxy_vac(TG,TH,HH,P,B,gbn);
237              FREQ = EE(8)-EE(1);
238                while abs(FREQQ-FREQ)>1;
239                         HH = HH * (FREQQ/FREQ);
240                         EE = EnergyLevels_oxy_vac(TG,TH,HH
                               ,P,B,gbn);
241                         FREQ = EE(8)-EE(1);
242                end
243              MagneticField(n,k) = HH;
244
245           elseif ic==2
246              HH = InitialHH;
247              EE = EnergyLevels_oxy_vac(TG,TH,HH,P,B,gbn);
248              FREQ = EE(7)-EE(2);
249                while abs(FREQQ-FREQ)>1;
250                         HH = HH * (FREQQ/FREQ);
251                         EE = EnergyLevels_oxy_vac(TG,TH,HH
                               ,P,B,gbn);
```

```
252                     FREQ = EE(7)-EE(2);
253                 end
254             MagneticField(n,k+4) = HH;
255
256         elseif ic==3
257             HH = InitialHH;
258             EE = EnergyLevels_oxy_vac(TG,TH,HH,P,B,gbn);
259             FREQ = EE(6)-EE(3);
260                 while abs(FREQQ-FREQ)>1;
261                     HH = HH * (FREQQ/FREQ);
262                     EE = EnergyLevels_oxy_vac(TG,TH,HH
                            ,P,B,gbn);
263                     FREQ = EE(6)-EE(3);
264                 end
265             MagneticField(n,k+8) = HH;
266
267         elseif ic==4
268             HH = InitialHH;
269             EE = EnergyLevels_oxy_vac(TG,TH,HH,P,B,gbn);
270             FREQ = EE(5)-EE(4);
271                 while abs(FREQQ-FREQ)>1;
272                     HH = HH * (FREQQ/FREQ);
273                     EE = EnergyLevels_oxy_vac(TG,TH,HH
                            ,P,B,gbn);
274                     FREQ = EE(5)-EE(4);
275                 end
```

```
276                 MagneticField(n,k+12) = HH;
277
278             end
279         end
280     end
281 end
282
283 elseif Plane==3          %  Rotation from c to a.
284
285 FREQQ = 9395.5;              % Measured microwave frequency
        (in MHz)
286
287 for n=1:91               %  Field direction increment is
       one degree.
288     Alpha = (n-1)*CTR;
289     Beta = 0*CTR;
290     N(n) = n-1;
291
292     R(1,1) = cos(Alpha)*cos(Beta);
293     R(1,2) = -sin(Beta);
294     R(1,3) = sin(Alpha)*cos(Beta);
295     R(2,1) = cos(Alpha)*sin(Beta);
296     R(2,2) = cos(Beta);
297     R(2,3) = sin(Alpha)*sin(Beta);
298     R(3,1) = -sin(Alpha);
299     R(3,2) = 0;
```

```
300     R(3,3) = cos(Alpha);
301
302     for k=1:4
303
304     if k==1          % Site 1
305         RR(1,1) = 1;RR(1,2) = 0;RR(1,3) = 0;
306         RR(2,1) = 0;RR(2,2) = 1;RR(2,3) = 0;
307         RR(3,1) = 0;RR(3,2) = 0;RR(3,3) = 1;
308
309     elseif k==2      % Site 2 (reflection in a plane)
310         RR(1,1) = -1;RR(1,2) = 0;RR(1,3) = 0;
311         RR(2,1) = 0;RR(2,2) = 1;RR(2,3) = 0;
312         RR(3,1) = 0;RR(3,2) = 0;RR(3,3) = 1;
313
314     elseif k==3      % Site 3 (reflection in b plane)
315         RR(1,1) = 1;RR(1,2) = 0;RR(1,3) = 0;
316         RR(2,1) = 0;RR(2,2) = -1;RR(2,3) = 0;
317         RR(3,1) = 0;RR(3,2) = 0;RR(3,3) = 1;
318
319     elseif k==4      % Site 4 (reflection in a and b planes
        )
320         RR(1,1) = -1;RR(1,2) = 0;RR(1,3) = 0;
321         RR(2,1) = 0;RR(2,2) = -1;RR(2,3) = 0;
322         RR(3,1) = 0;RR(3,2) = 0;RR(3,3) = 1;
323
324     end
```

```
325
326     R1 = RR * R;
327     TG = G * R1;
328     TH = H * R1;
329
330        for ic=1:4
331
332           if ic==1
333              HH = InitialHH;
334              EE = EnergyLevels_oxy_vac(TG,TH,HH,P,B,gbn);
335              FREQ = EE(8)-EE(1);
336                while abs(FREQQ-FREQ)>1;
337                         HH = HH * (FREQQ/FREQ);
338                         EE = EnergyLevels_oxy_vac(TG,TH,HH
                               ,P,B,gbn);
339                         FREQ = EE(8)-EE(1);
340                end
341              MagneticField(n,k) = HH;
342
343           elseif ic==2
344              HH = InitialHH;
345              EE = EnergyLevels_oxy_vac(TG,TH,HH,P,B,gbn);
346              FREQ = EE(7)-EE(2);
347                while abs(FREQQ-FREQ)>1;
348                         HH = HH * (FREQQ/FREQ);
349                         EE = EnergyLevels_oxy_vac(TG,TH,HH
```

```
                        ,P,B,gbn);
350                     FREQ = EE(7)-EE(2);
351               end
352           MagneticField(n,k+4) = HH;
353
354       elseif ic==3
355           HH = InitialHH;
356           EE = EnergyLevels_oxy_vac(TG,TH,HH,P,B,gbn);
357           FREQ = EE(6)-EE(3);
358             while abs(FREQQ-FREQ)>1;
359                     HH = HH * (FREQQ/FREQ);
360                     EE = EnergyLevels_oxy_vac(TG,TH,HH
                        ,P,B,gbn);
361                     FREQ = EE(6)-EE(3);
362             end
363           MagneticField(n,k+8) = HH;
364
365       elseif ic==4
366           HH = InitialHH;
367           EE = EnergyLevels_oxy_vac(TG,TH,HH,P,B,gbn);
368           FREQ = EE(5)-EE(4);
369             while abs(FREQQ-FREQ)>1;
370                     HH = HH * (FREQQ/FREQ);
371                     EE = EnergyLevels_oxy_vac(TG,TH,HH
                        ,P,B,gbn);
372                     FREQ = EE(5)-EE(4);
```

```
373                 end
374                 MagneticField(n,k+12) = HH;
375
376             end
377         end
378     end
379 end
380
381 elseif Plane==4          %  Rotation from c to the midpoint
    of a and b.
382
383 FREQQ = 9395.5;              % Measured microwave frequency
    (in MHz)
384
385 for n=1:91               %  Field direction increment is
   one degree.
386     Alpha = (n-1)*CTR;
387     Beta = 45*CTR;
388     N(n) = n-1;
389
390     R(1,1) = cos(Alpha)*cos(Beta);
391     R(1,2) = -sin(Beta);
392     R(1,3) = sin(Alpha)*cos(Beta);
393     R(2,1) = cos(Alpha)*sin(Beta);
394     R(2,2) = cos(Beta);
395     R(2,3) = sin(Alpha)*sin(Beta);
```

```
396     R(3,1) = -sin(Alpha);
397     R(3,2) = 0;
398     R(3,3) = cos(Alpha);
399
400     for k=1:4
401
402     if k==1          % Site 1
403         RR(1,1) = 1;RR(1,2) = 0;RR(1,3) = 0;
404         RR(2,1) = 0;RR(2,2) = 1;RR(2,3) = 0;
405         RR(3,1) = 0;RR(3,2) = 0;RR(3,3) = 1;
406
407     elseif k==2      % Site 2 (reflection in a plane)
408         RR(1,1) = -1;RR(1,2) = 0;RR(1,3) = 0;
409         RR(2,1) = 0;RR(2,2) = 1;RR(2,3) = 0;
410         RR(3,1) = 0;RR(3,2) = 0;RR(3,3) = 1;
411
412     elseif k==3      % Site 3 (reflection in b plane)
413         RR(1,1) = 1;RR(1,2) = 0;RR(1,3) = 0;
414         RR(2,1) = 0;RR(2,2) = -1;RR(2,3) = 0;
415         RR(3,1) = 0;RR(3,2) = 0;RR(3,3) = 1;
416
417     elseif k==4      % Site 4 (reflection in a and b planes
        )
418         RR(1,1) = -1;RR(1,2) = 0;RR(1,3) = 0;
419         RR(2,1) = 0;RR(2,2) = -1;RR(2,3) = 0;
420         RR(3,1) = 0;RR(3,2) = 0;RR(3,3) = 1;
```

```
421
422     end
423
424     R1 = RR * R;
425     TG = G * R1;
426     TH = H * R1;
427
428        for ic=1:4
429
430           if ic==1
431              HH = InitialHH;
432              EE = EnergyLevels_oxy_vac(TG,TH,HH,P,B,gbn);
433              FREQ = EE(8)-EE(1);
434                while abs(FREQQ-FREQ)>1;
435                         HH = HH * (FREQQ/FREQ);
436                         EE = EnergyLevels_oxy_vac(TG,TH,HH
                                ,P,B,gbn);
437                         FREQ = EE(8)-EE(1);
438                end
439              MagneticField(n,k) = HH;
440
441           elseif ic==2
442              HH = InitialHH;
443              EE = EnergyLevels_oxy_vac(TG,TH,HH,P,B,gbn);
444              FREQ = EE(7)-EE(2);
445                while abs(FREQQ-FREQ)>1;
```

```
446                         HH = HH * (FREQQ/FREQ);
447                         EE = EnergyLevels_oxy_vac(TG,TH,HH
                               ,P,B,gbn);
448                         FREQ = EE(7)-EE(2);
449                   end
450               MagneticField(n,k+4) = HH;
451
452           elseif ic==3
453               HH = InitialHH;
454               EE = EnergyLevels_oxy_vac(TG,TH,HH,P,B,gbn);
455               FREQ = EE(6)-EE(3);
456                 while abs(FREQQ-FREQ)>1;
457                         HH = HH * (FREQQ/FREQ);
458                         EE = EnergyLevels_oxy_vac(TG,TH,HH
                               ,P,B,gbn);
459                         FREQ = EE(6)-EE(3);
460                   end
461               MagneticField(n,k+8) = HH;
462
463           elseif ic==4
464               HH = InitialHH;
465               EE = EnergyLevels_oxy_vac(TG,TH,HH,P,B,gbn);
466               FREQ = EE(5)-EE(4);
467                 while abs(FREQQ-FREQ)>1;
468                         HH = HH * (FREQQ/FREQ);
469                         EE = EnergyLevels_oxy_vac(TG,TH,HH
```

```
                                ,P,B,gbn);
470                           FREQ = EE(5)-EE(4);
471                   end
472                MagneticField(n,k+12) = HH;
473
474             end
475         end
476     end
477
478 plot(N,MagneticField,'-')
479 ylabel('Magnetic Field (gauss)')
480 xlabel('Angle (degrees)')
481
482 end
483
484 end
485
486 %%%%%%%%%%%%%%%%%%%%%%%%%%%%%%%
487
488 % Experimental magnetic field values for each plane.
489
490 if Plane==1
491
492 % a to b plane (Plane 1)
493
494 h(1)=3144.62*1.00229527+0.39773306;Beta(1)=0;
```

```
495 h(2)=3543.95*1.00229527+0.39773306;Beta(2)=0;
496
497 h(3)=3135.61*1.00229527+0.39773306;Beta(3)=20;
498 h(4)=3528.94*1.00229527+0.39773306;Beta(4)=20;
499 h(5)=3161.63*1.00229527+0.39773306;Beta(5)=20;
500 h(6)=3554.46*1.00229527+0.39773306;Beta(6)=20;
501
502 h(7)=3134.61*1.00229527+0.39773306;Beta(7)=30;
503 h(8)=3525.94*1.00229527+0.39773306;Beta(8)=30;
504 h(9)=3163.14*1.00229527+0.39773306;Beta(9)=30;
505 h(10)=3554.46*1.00229527+0.39773306;Beta(10)=30;
506
507 h(11)=3135.11*1.00229527+0.39773306;Beta(11)=40;
508 h(12)=3520.43*1.00229527+0.39773306;Beta(12)=40;
509 h(13)=3168.14*1.00229527+0.39773306;Beta(13)=40;
510 h(14)=3553.96*1.00229527+0.39773306;Beta(14)=40;
511
512 h(15)=3137.11*1.00229527+0.39773306;Beta(15)=50;
513 h(16)=3516.43*1.00229527+0.39773306;Beta(16)=50;
514 h(17)=3174.65*1.00229527+0.39773306;Beta(17)=50;
515 h(18)=3553.46*1.00229527+0.39773306;Beta(18)=50;
516
517 h(19)=3143.12*1.00229527+0.39773306;Beta(19)=60;
518 h(20)=3513.43*1.00229527+0.39773306;Beta(20)=60;
519 h(21)=3175.15*1.00229527+0.39773306;Beta(21)=60;
520 h(22)=3546.96*1.00229527+0.39773306;Beta(22)=60;
```

```
521
522 h(23)=3148.12*1.00229527+0.39773306;Beta(23)=70;
523 h(24)=3514.43*1.00229527+0.39773306;Beta(24)=70;
524 h(25)=3173.64*1.00229527+0.39773306;Beta(25)=70;
525 h(26)=3540.45*1.00229527+0.39773306;Beta(26)=70;
526
527 h(27)=3163.14*1.00229527+0.39773306;Beta(27)=90;
528 h(28)=3525.44*1.00229527+0.39773306;Beta(28)=90;
529
530 plot(N,MagneticField,'-',Beta,h,'o')
531 ylabel('Magnetic Field (gauss)')
532 xlabel('Angle (degrees)')
533
534 filename = 'LBOangulardependenceab,xls'
535 xlswrite(filename,MagneticField)
536
537 filename = 'LBOexperimentalpointsab'
538 xlswrite(filename,h)
539
540
541 elseif Plane==2
542
543 % b to c plane (Plane 2)
544
545 h(1)=3161.63*1.00229527+0.39773306;Alpha(1)=90;
546 h(2)=3523.44*1.00229527+0.39773306;Alpha(2)=90;
```

```
547
548 h(3)=3154.13*1.00229527+0.39773306;Alpha(3)=70;
549 h(4)=3515.43*1.00229527+0.39773306;Alpha(4)=70;
550 h(5)=3172.64*1.00229527+0.39773306;Alpha(5)=70;
551 h(6)=3535.95*1.00229527+0.39773306;Alpha(6)=70;
552
553 h(7)=3151.13*1.00229527+0.39773306;Alpha(7)=60;
554 h(8)=3513.43*1.00229527+0.39773306;Alpha(8)=60;
555 h(9)=3174.65*1.00229527+0.39773306;Alpha(9)=60;
556 h(10)=3539.45*1.00229527+0.39773306;Alpha(10)=60;
557
558 h(11)=3150.13*1.00229527+0.39773306;Alpha(11)=50;
559 h(12)=3514.43*1.00229527+0.39773306;Alpha(12)=50;
560 h(13)=3174.65*1.00229527+0.39773306;Alpha(13)=50;
561 h(14)=3537.45*1.00229527+0.39773306;Alpha(14)=50;
562
563 h(15)=3147.62*1.00229527+0.39773306;Alpha(15)=40;
564 h(16)=3512.93*1.00229527+0.39773306;Alpha(16)=40;
565 h(17)=3175.15*1.00229527+0.39773306;Alpha(17)=40;
566 h(18)=3538.95*1.00229527+0.39773306;Alpha(18)=40;
567
568 h(19)=3149.12*1.00229527+0.39773306;Alpha(19)=30;
569 h(20)=3514.43*1.00229527+0.39773306;Alpha(20)=30;
570 h(21)=3172.14*1.00229527+0.39773306;Alpha(21)=30;
571 h(22)=3537.95*1.00229527+0.39773306;Alpha(22)=30;
572
```

```
573 h(23)=3149.12*1.00229527+0.39773306;Alpha(23)=20;
574 h(24)=3516.43*1.00229527+0.39773306;Alpha(24)=20;
575 h(25)=3170.14*1.00229527+0.39773306;Alpha(25)=20;
576 h(26)=3535.95*1.00229527+0.39773306;Alpha(26)=20;
577
578 h(27)=3160.12*1.00229527+0.39773306;Alpha(27)=0;
579 h(28)=3526.44*1.00229527+0.39773306;Alpha(28)=0;
580
581 plot(N,MagneticField,'-',Alpha,h,'o')
582 ylabel('Magnetic Field (gauss)')
583 xlabel('Angle (degrees)')
584
585 filename = 'LBOangulardependencebc,xls'
586 xlswrite(filename,MagneticField)
587
588 filename = 'LBOexperimentalpointsbc'
589 xlswrite(filename,h)
590
591 elseif Plane==3
592
593 % c to a plane (Plane 3)
594
595 h(1)=3159.59*1.00229527+0.39773306;Alpha(1)=0;
596 h(2)=3525.90*1.00229527+0.39773306;Alpha(2)=0;
597
598 h(3)=3145.08*1.00229527+0.39773306;Alpha(3)=20;
```

```
599 h(4)=3513.89*1.00229527+0.39773306;Alpha(4)=20;
600 h(5)=3171.10*1.00229527+0.39773306;Alpha(5)=20;
601 h(6)=3542.41*1.00229527+0.39773306;Alpha(6)=20;
602
603 h(7)=3139.57*1.00229527+0.39773306;Alpha(7)=30;
604 h(8)=3510.88*1.00229527+0.39773306;Alpha(8)=30;
605 h(9)=3172.60*1.00229527+0.39773306;Alpha(9)=30;
606 h(10)=3546.91*1.00229527+0.39773306;Alpha(10)=30;
607
608 h(11)=3136.07*1.00229527+0.39773306;Alpha(11)=40;
609 h(12)=3511.88*1.00229527+0.39773306;Alpha(12)=40;
610 h(13)=3173.60*1.00229527+0.39773306;Alpha(13)=40;
611 h(14)=3551.42*1.00229527+0.39773306;Alpha(14)=40;
612
613 h(15)=3133.57*1.00229527+0.39773306;Alpha(15)=50;
614 h(16)=3515.39*1.00229527+0.39773306;Alpha(16)=50;
615 h(17)=3169.60*1.00229527+0.39773306;Alpha(17)=50;
616 h(18)=3555.42*1.00229527+0.39773306;Alpha(18)=50;
617
618 h(19)=3132.57*1.00229527+0.39773306;Alpha(19)=60;
619 h(20)=3519.89*1.00229527+0.39773306;Alpha(20)=60;
620 h(21)=3164.60*1.00229527+0.39773306;Alpha(21)=60;
621 h(22)=3555.92*1.00229527+0.39773306;Alpha(22)=60;
622
623 h(23)=3134.07*1.00229527+0.39773306;Alpha(23)=70;
624 h(24)=3524.90*1.00229527+0.39773306;Alpha(24)=70;
```

```
h(25)=3159.09*1.00229527+0.39773306;Alpha(25)=70;
h(26)=3555.42*1.00229527+0.39773306;Alpha(26)=70;

h(27)=3143.58*1.00229527+0.39773306;Alpha(27)=90;
h(28)=3543.91*1.00229527+0.39773306;Alpha(28)=90;

plot(N,MagneticField,'-',Alpha,h,'o')
ylabel('Magnetic Field (gauss)')
xlabel('Angle (degrees)')

filename = 'LBOangulardependenceca,xls'
xlswrite(filename,MagneticField)

filename = 'LBOexperimentalpointsca'
xlswrite(filename,h)

end
```

E.4 Energy Levels and Eigenvalues of the Spin Hamiltonian for the Oxygen Vacancies in LiB_3O_5

This subroutine is used in conjunction with "LBO oxy vac linepositions BH" to calculate the line positions as a function of angle for oxygen vacancies in LiB_3O_5. It calculates the eigenvalues and returns them to the main program.

```
function EE = EnergyLevels_oxy_vac_BH(TG,TH,HH,P,B,gbn)

W1 = B*HH*(P(1)*TG(1,1)*TG(1,3)+P(2)*TG(2,1)*TG(2,3)+P(3)*
   TG(3,1)*TG(3,3));
W2 = B*HH*(P(1)*TG(1,2)*TG(1,3)+P(2)*TG(2,2)*TG(2,3)+P(3)*
   TG(3,2)*TG(3,3));
W3 = B*HH*(P(1)*TG(1,3)*TG(1,3)+P(2)*TG(2,3)*TG(2,3)+P(3)*
   TG(3,3)*TG(3,3));
W4 = P(7)*TH(1,1)*TH(1,1)+P(8)*TH(2,1)*TH(2,1)+P(9)*TH
   (3,1)*TH(3,1);
W5 = P(7)*TH(1,2)*TH(1,1)+P(8)*TH(2,2)*TH(2,1)+P(9)*TH
   (3,2)*TH(3,1);
W6 = P(7)*TH(1,3)*TH(1,1)+P(8)*TH(2,3)*TH(2,1)+P(9)*TH
   (3,3)*TH(3,1);
W7 = P(7)*TH(1,2)*TH(1,2)+P(8)*TH(2,2)*TH(2,2)+P(9)*TH
   (3,2)*TH(3,2);
W8 = P(7)*TH(1,3)*TH(1,2)+P(8)*TH(2,3)*TH(2,2)+P(9)*TH
   (3,3)*TH(3,2);
W9 = P(7)*TH(1,3)*TH(1,3)+P(8)*TH(2,3)*TH(2,3)+P(9)*TH
   (3,3)*TH(3,3);

```

```
Q1 = 0.5*(W1+i*W2);
Q2 = 0.25*(W4-W7)+0.5*i*W5;
Q3 = 0.25*(W4+W7);
Q4 = 0.5*(W6+i*W8);

% HAM is the matrix representing the spin-Hamiltonian

Ham = zeros(8);
Ham(1,1) = 0.5*W3 + 0.75*W9 - 1.5*gbn*HH;
Ham(2,2) = 0.5*W3 + 0.25*W9 - 0.5*gbn*HH;
Ham(3,3) = 0.5*W3 - 0.25*W9 + 0.5*gbn*HH;
Ham(4,4) = 0.5*W3 - 0.75*W9 + 1.5*gbn*HH;
Ham(5,5) = -0.5*W3 - 0.75*W9 - 1.5*gbn*HH;
Ham(6,6) = -0.5*W3 - 0.25*W9 - 0.5*gbn*HH;
Ham(7,7) = -0.5*W3 + 0.25*W9 + 0.5*gbn*HH;
Ham(8,8) = -0.5*W3 + 0.75*W9 + 1.5*gbn*HH;
Ham(2,1) = 0.5*sqrt(3)*Q4;
Ham(3,2) = Q4;
Ham(4,3) = 0.5*sqrt(3)*Q4;
Ham(5,1) = Q1 + 1.5*Q4;
Ham(5,2) = sqrt(3)*Q3;
Ham(6,1) = sqrt(3)*Q2;
Ham(6,2) = Q1 + 0.5*Q4;
Ham(6,3) = 2*Q3;
Ham(6,5) = -0.5*sqrt(3)*Q4;
Ham(7,2) = 2*Q2;
```

```
39 Ham(7,3) = Q1 - 0.5*Q4;
40 Ham(7,4) = sqrt(3)*Q3;
41 Ham(7,6) = -Q4;
42 Ham(8,3) = sqrt(3)*Q2;
43 Ham(8,4) = Q1 - 1.5*Q4;
44 Ham(8,7) = -0.5*sqrt(3)*Q4;
45 Ham(1,2) = conj(Ham(2,1));
46 Ham(2,3) = conj(Ham(3,2));
47 Ham(3,4) = conj(Ham(4,3));
48 Ham(1,5) = conj(Ham(5,1));
49 Ham(2,5) = conj(Ham(5,2));
50 Ham(1,6) = conj(Ham(6,1));
51 Ham(2,6) = conj(Ham(6,2));
52 Ham(3,6) = conj(Ham(6,3));
53 Ham(5,6) = conj(Ham(6,5));
54 Ham(2,7) = conj(Ham(7,2));
55 Ham(3,7) = conj(Ham(7,3));
56 Ham(4,7) = conj(Ham(7,4));
57 Ham(6,7) = conj(Ham(7,6));
58 Ham(3,8) = conj(Ham(8,3));
59 Ham(4,8) = conj(Ham(8,4));
60 Ham(7,8) = conj(Ham(8,7));
61
62 EE = sort(real(eig(Ham)));
```

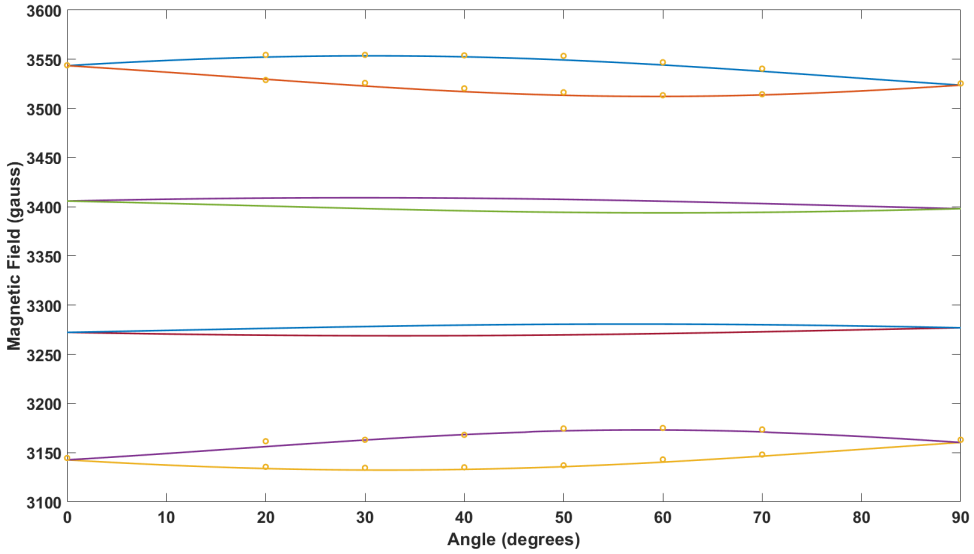

Figure E.1. Angular dependence fitting in the *ab* plane. The crystal was oriented in the spectrometer such that the c direction was up and the crystal could be rotated in the *ab* plane. The crystal was rotated from the *a* to *b* direction in ten degree increments. At each increment an EPR spectrum was acquired and the magnetic field values of the spectra was recorded along with the microwave frequency. As the EPR lines split during rotation, only those increments where the middle of the lines splits could be determined were used as magnetic field input values in the fitting routine. The solid lines represent the calculated angular dependence and line splitting based on the least-squares fitting output of the g and A matrix parameters. The circles represent the magnetic field values recorded from the center of the four hyperfine lines and their splits as the crystal was rotated. The overlay of the experimental values and the calculated angular dependence show a good fit between the data and the model.

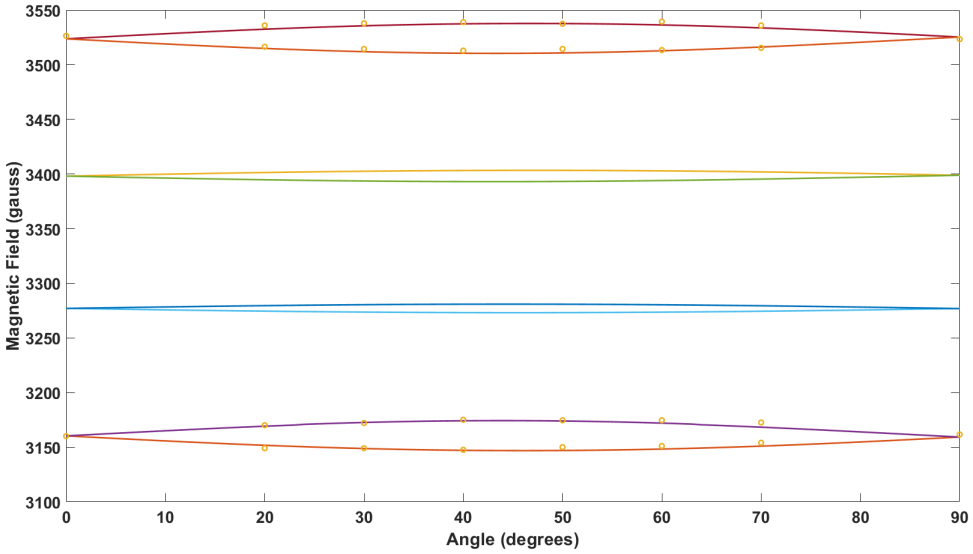

Figure E.2. Angular dependence fitting in the *bc* plane. The crystal was oriented in the spectrometer such that the a direction was up and the crystal could be rotated in the *bc* plane. The crystal was rotated from the *b* to *c* direction in ten degree increments. At each increment an EPR spectrum was acquired and the magnetic field values of the spectra was recorded along with the microwave frequency. As the EPR lines split during rotation, only those increments where the middle of the lines splits could be determined were used as magnetic field input values in the fitting routine. The solid lines represent the calculated angular dependence and line splitting based on the least-squares fitting output of the g and A matrix parameters. The circles represent the magnetic field values recorded from the center of the four hyperfine lines and their splits as the crystal was rotated. The overlay of the experimental values and the calculated angular dependence show a good fit between the data and the model.

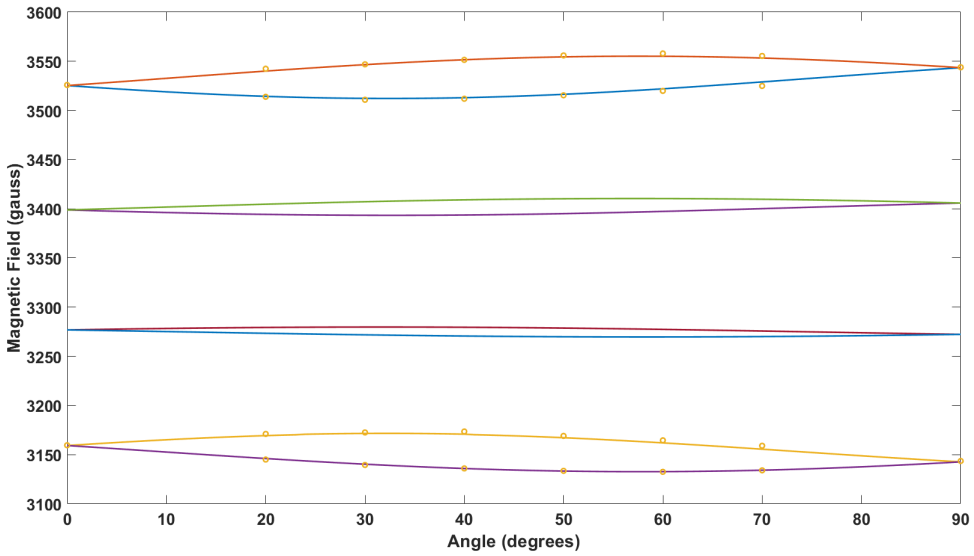

Figure E.3. Angular dependence fitting in the *ca* plane. The crystal was oriented in the spectrometer such that the b direction was up and the crystal could be rotated in the *ca* plane. The crystal was rotated from the *c* to *a* direction in ten degree increments. At each increment an EPR spectrum was acquired and the magnetic field values of the spectra was recorded along with the microwave frequency. As the EPR lines split during rotation, only those increments where the middle of the lines splits could be determined were used as magnetic field input values in the fitting routine. The solid lines represent the calculated angular dependence and line splitting based on the least-squares fitting output of the g and A matrix parameters. The circles represent the magnetic field values recorded from the center of the four hyperfine lines and their splits as the crystal was rotated. The overlay of the experimental values and the calculated angular dependence show a good fit between the data and the model.

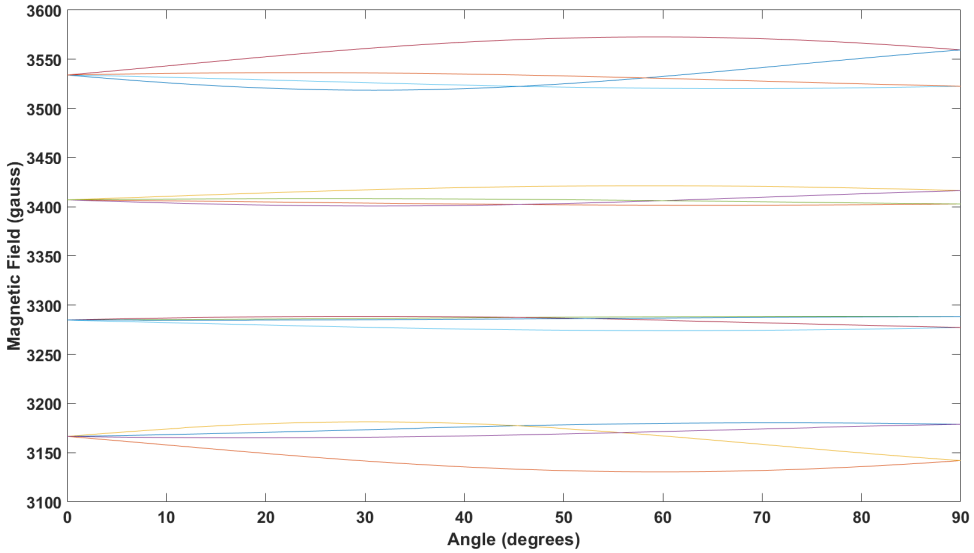

Figure E.4. Angular dependence predicted by choice 1 parameters. This proved to be the correct choice.

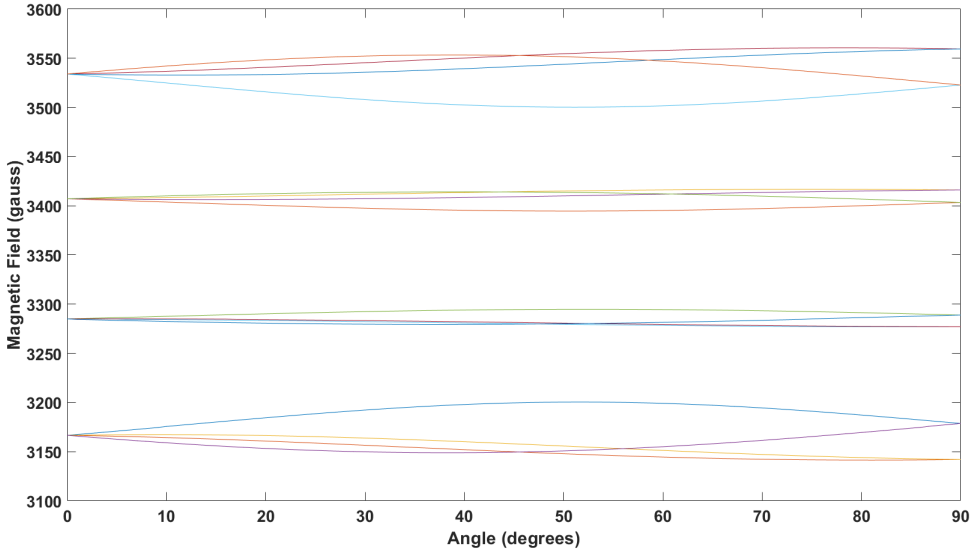

Figure E.5. Angular dependence predicted by choice 2 parameters

Bibliography

1. V. Petrov, "Frequency down-conversion of solid-state laser sources to the mid-infrared spectral range using non-oxide nonlinear crystals," *Progress in Quantum Electronics*, vol. 42, pp. 1–106, 2015.

2. X. Luo, Z. Li, Y. Guo, J. Yao, and Y. Wu, "Recent progress on new infrared nonlinear optical materials with application prospect," *Journal of Solid State Chemistry*, vol. 270, pp. 674–687, 2019.

3. "Nonlinear crystal technologies," BAE Systems. [Online]. Available: https://www.baesystems.com/en-us/product/nonlinear-crystal-technologies

4. Q. NIU, Z. HE, and S. DONG, "Ir radiation characteristics of rocket exhaust plumes under varying motor operating conditions," *Chinese Journal of Aeronautics*, vol. 30, pp. 1101–1114, 2017.

5. D. B. Kolker, N. Y. Kostyukova, A. A. Boyko, V. V. Badikov, D. V. Badikov, A. G. Shadrintseva, N. N. Tretyakova, K. G. Zenov, A. A. Karapuzikov, and J.-J. Zondy, "Widely tunable 2.6-10.4 μm $BaGa_4Se_7$ optical parametric oscillator pumped by a Q-switched Nd:$YLiF_4$ laser," *Journal of Physics Communications*, vol. 2, no. 035039, 2018.

6. F. K. Tittel, D. Richter, and A. Fried, *Mid-Infrared Laser Applications in Spectroscopy*. Springer Berlin Heidelberg, 2003.

7. P. E. Powers and J. W. Haus, *Fundamentals of Nonlinear Optics*, 2nd ed. CRC Press, 2019.

8. Y. Guo, Y. Zhou, , X. Lin, W. Chen, and N. Ye, "Growth and characterizations of $BaGa_4S_7$ crystal," *Optical Materials*, vol. 36, pp. 2007–2011, 2014.

9. J. Yao, D. Mei, L. Bai, W. Yin, P. Fu, and Y. Wu, "$BaGa_4Se_7$: A new congruent-melting ir nonlinear optical material," *Inorganic Chemistry*, vol. 49, pp. 9212–9216, 2010.

10. X. Lin, Y. Guo, and N. Ye, "$BaGa_2GeX_6$ (X = S, Se) : New mid-IR nonlinear optical crystals with large band gaps," *Journal of Solid State Chemistry*, vol. 195, pp. 172–177, 2012.

11. X. Zhang, J. Yao, W. Yin, Y. Zhu, Y. Wu, and C. Chen, "Determination of the nonlinear optical coefficients of the $BaGa_4Se_7$ crystal," *Optics Express*, vol. 23, pp. 552–558, 2015.

12. V. Petrov, V. V. Badikov, D. V. Badikov, K. Kato, G. S. Shevyrdyaeva, K. Miyata, M. Mero, L. Wang, Z. Heiner, and V. L. Panyutin, "Barium nonlinear optical crystals for the mid-IR: Characterization and some applications," *Journal of the Optical Society of America B*, vol. 38, pp. B46–B58, 2021.

13. J. Yao, W. Yin, K. Feng, X. Li, D. Mei, Q. Lu, Y. Ni, Z. Zhang, Z. Hu, and Y. Wu, "Growth and characterization of $BaGa_4Se_7$ crystal," *Journal of Crystal Growth*, vol. 346, pp. 1–4, 2012.

14. A. P. Yelisseyev, S. I. Lobanov, P. G. Krinitsin, and L. I. Isaenko, "The optical properties of the nonlinear crystal $BaGa_4Se_7$," *Optical Materials*, vol. 99, no. 109564, 2020.

15. M. S. Fox, *Optical Properties of Solids*, 2nd ed. Oxford University Press, 2010.

16. B. C. Ziegler and K. L. Schepler, "Transmission and damage-threshold measurements in AgGaSe2 at 2.1 μm," *Applied Optics*, vol. 30, pp. 5077–5080, 1991.

17. A. Gribenyukov, S. Podzyvalov, A. Soldatov, A. Shumeiko, N. Yudin, N. Yudin, and V. Yurin, "Defectoscopy of $ZnGeP_2$ single crystals by strontium vapour laser radiation," *Quantum Electronics*, vol. 48, pp. 491–494, 2018.

18. D. Xu, J. Zhang, Y. He, Y. Wang, J. Yao, Y. Guo, C. Yan, L. Tang, J. Li, K. Zhong, Y. Wu, and J. Yao, "High-energy, tunable, long-wave mid-infrared optical parametric oscillator based on $BaGa_4Se_7$ crystal," *Optics Letters*, vol. 45, pp. 5287–5290, 2021.

19. C. Chen, Y. Wu, A. Jian, B. Wu, G. You, R. Li, and S. Lin, "New nonlinear-optical crystal: LiB_3O_5," *Journal of the Optical Society of America B: Optical Physics*, vol. 6, pp. 616–626, 1989.

20. W. Hong, M. M. Chirila, N. Y. Garces, L. E. Halliburton, D. Lupinski, and P. Villeval, "Electron paramagnetic resonance and electron-nuclear double resonance study of trapped-hole centers in LiB_3O_5 crystals," *Physical Review B*, vol. 68, no. 094111, 2003.

21. S. Lin, Z. Sun, B. Wu, and C. Chen, "The nonlinear optical characteristics of a LiB_3O_5 crystal," *Journal of Applied Physics*, vol. 67, pp. 634–638, 1990.

22. J. D. Bierlein and C. B. Arweiler, "Electro-optic and dielectric properties of $TIiOPO_4$," *Applied Physics Letters*, vol. 49, pp. 917–919, 1986.

23. M. P. Scripsick, X. H. Fang, G. J. Edwards, L. E. Halliburton, and J. K. Tyminski, "Point defects in lithium triborate (LiB_3O_5) crystals," *Journal of Applied Physics*, vol. 73, pp. 1114–1118, 1993.

24. I. N. Ogorodnikov, A. Y. Kuznetsov, A. V. Kruzhalov, and V. A. Maslov, "Point defects and short-wavelength luminescence of LiB_3O_5 single crystals," *Radiation Effects and Defects in Solids*, vol. 136, pp. 233–237, 1995.

25. D. Redfield and R. Bube, *Photoinduced Defects in Semiconductors*. Cambridge University Press, 1996.

26. N. C. Giles and L. E. Halliburton, "8 - Electron Paramagnetic Resonance (EPR) from $\beta - Ga_2O_3$ crystals," in *Gallium Oxide: Technology, Devices and Applications*, S. Pearton, F. Ren, and M. Mastro, Eds. Elsevier, 2019, pp. 169–190.

27. B. C. Holloway, T. D. Gustafson, C. A. Lenyk, N. C. Giles, K. T. Zawilski, P. G. Schunemann, K. L. Averett, and L. E. Halliburton, "Optically active selenium vacancies in $BaGa_4Se_7$," *Journal of Applied Physics*, vol. 130, no. 173104, 2021.

28. I. N. Ogorodnikov, A. V. Porotnikov, S. V. Kudyakov, and A. V. Kruzhalov, "Stable and metastable optical absorption of LiB_3O_5 nonlinear crystals," *Physics of the Solid State*, vol. 39, pp. 1366–1368, 1997.

29. K. Kato, K. Miyata, and V. Petrov, "Phase-matching properties of $BaGa_4Se_7$ for SHG and SFG in the 0.901-10.5910 μm range," *Applied Optics*, vol. 56, pp. 2978–2981, 2017.

30. E. Boursier, P. Segonds, B. Menaert, V. Badikov, V. Panyutin, D. Badikov, V. Petrov, and B. Boulanger, "Phase-matching directions and refined sellmeier equations of the monoclinic acentric crystal $BaGa_4Se_7$," *Optics Letters*, vol. 41, pp. 2731–2734, 2016.

31. M. D. McCluskey, "Point defects in Ga_2O_3," *Journal of Applied Physics*, vol. 127, no. 101101, 2020.

32. J. A. Weil and J. R. Bolton, *Electron Paramagnetic Resonance: Elementary Theory and Practical Applications*, 2nd ed. John Wiley and Sons, Inc, 2007.

33. J.-M. Spaeth, J. Niklas, and R. Bartman, *Structural Analysis of Point Defects in Solids*. Spinger-Verlag, 1982.

34. A. Abragam and B. Bleaney, *Electron Paramagnetic Resonance of Transition Metal Ions*, 1st ed. Clarendon Press, 1970.

35. N. W. Ashcroft and N. D. Mermin, *Solid State Physics*. Cengage Learning, 1976.

36. R. T. Weber, J. Jiang, and D. P. Barr, *EMX User's Manual*. Bruker Biospin Corporation, 1998.

37. S. M. Scherrer, "Optical electron paramagnetic resonance characterization of point defect in semiconductors," Ph.D. dissertation, Air Force Institute of Technology, 2017.

38. M. Brustolon and E. Giamello, *Electron Paramagnetic Resonance: A Practitioner's Toolkit*. John Wiley and Sons, Inc.

39. J. W. Orton, *Electron Paramagnetic Resonance: An Introduction to Transition Group Ions in Crystals*. Iliffe, London, U.K., 1968.

40. "Cary 100/300/4000/5000/6000i/7000 spectrophotometers user's guide," Agilent Technologies Inc. [Online]. Available: https://www.agilent.com/cs/library/usermanuals/public/1972_7000.pdf

41. "User guide for cary 5000 spectrometer with external dra 1800..." Molecular Materials Resource Center at Caltech. [Online]. Available: https://mmrc.caltech.edu/Cary20UV-Vis20Int.Sphere/manuals/Cary5000_User_Guide.pdf

42. X. Luo, Z. Li, Y. Guo, J. Yao, and Y. Wu, "Recent progress on new infrared nonlinear optical materials with application prospect," *Journal of Solid State Chemistry*, vol. 270, pp. 674–687, 2019.

43. A. Abudurusuli, J. Li, and S. Pan, "A review on the recently developed promising infrared nonlinear optical materials," *Dalton Transactions*, vol. 50, pp. 3155–3160, 2021.

44. S. Slussarenko and G. J. Pryde, "Photonic quantum information processing: A concise review," *Applied Physics Reviews*, vol. 6, no. 041303, 2019.

45. S. Krastanov, M. Heuck, J. H. Shapiro, P. Narang, D. R. Englund, and K. Jacobs, "Room-temperature photonic logical qubits via second-order nonlinearities," *Nature Communications*, vol. 12, p. 191, 2021.

46. J. Yao, D. Mei, L. Bai, Z. Lin, W. Yin, P. Fu, and Y. Wu, "$BaGa_4Se_7$: A new congruent-melting IR nonlinear optical material," *Inorganic Chemistry*, vol. 49, pp. 9212–9216, 2010.

47. V. Badikov, D. Badikov, G. Shevyrdyaeva, A. Tyazhev, G. Marchev, V. Panyutin, V. Petrov, and A. Kwasniewski, "Phase-matching properties of $BaGa_4S_7$ and $BaGa_4Se_7$: Wide-bandgap nonlinear crystals for the mid-infrared," *Physica Status Solidi RRL*, vol. 5, pp. 31–33, 2011.

48. F. Yang, J. Yao, H. Xu, K. Feng, W. Yin, F. Li, J. Yang, S. Du, Q. Peng, J. Zhang, D. Cui, Y. Wu, C. Chen, and Z. Xu, "High efficiency and high peak power picosecond mid-infrared optical parametric amplifier based on $BaGa_4Se_7$ crystal," *Optics Letters*, vol. 38, pp. 3903–3905, 2013.

49. N. Y. Kostyukova, A. A. Boyko, V. Badikov, D. Badikov, G. Shevyrdyaeva, V. Panyutin, G. M. Marchev, D. B. Kolker, and V. Petrov, "Widely tunable in the mid-ir $BaGa_4Se_7$ optical parametric oscillator pumped at 1064 nm," *Optics Letters*, vol. 41, pp. 3667–3670, 2016.

50. G. Liu, Y. Chen, Z. Li, K. Yang, B. Yao, J. Yao, R. Wang, C. Yang, S. Mi, T. Dai, and X. Duan, "High-beam-quality 2.1 m pumped mid-infrared type-ii phase-matching $BaGa_4Se_7$ optical parametric oscillator with a $ZnGeP_2$ amplifier," *Optics Letters*, vol. 45, pp. 3805–3808, 2020.

51. D. Xu, J. Zhang, Y. He, Y. Wang, J. Yao, Y. Guo, C. Yan, L. Tang, J. Li, K. Zhong, Y. Wu, and J. Yao, "High-energy, tunable, long-wave mid-infrared optical parametric oscillator based on $BaGa_4Se_7$ crystal," *Optics Letters*, vol. 45, pp. 5287–5290, 2020.

52. F. Yang, J.-Y. Yao, Y.-W. Guo, L. Yuan, Y. Bo, Q.-J. Peng, D.-F. Cui, Y.-C. Wu, and Z.-Y. Xu, "High-energy continuously tunable 8–14 picosecond coherent radiation generation from $BaGa_4Se_7$-OPA pumped by 1064 laser," *Optics and Laser Technology*, vol. 125, no. 106040, 2020.

53. K. Yang, G. Liu, C. Li, B. Yao, J. Yao, Y. Chen, S. Mi, X. Duan, and T. Dai, "Research on performance improvement technology of a $BaGa_4Se_7$ mid-infrared optical parametric oscillator," *Chinese Optics Letters*, vol. 45, pp. 6418–6421, 2020.

54. Y. Zhang, Y. Zuo, Z. Li, B. Wu, J. Yao, and Y. Shen, "High energy mid-infrared laser pulse output from a $BaGa_4Se_7$ crystal-based optical parametric oscillator," *Optics Letters*, vol. 45, pp. 4595–4598, 2020.

55. B. N. Carnio, E. Hopmann, K. T. Zawilski, P. G. Schunemann, and A. Y. Elezzabi, "Dependence on excitation polarization and crystal orientation for terahertz radiation generation in a $BaGa_4Se_7$ crystal," *Optics Express*, vol. 28, pp. 15 016–15 022, 2020.

56. B. N. Carnio, K. T. Zawilski, P. G. Schunemann, and A. Y. Elezzabi, "Generation of narrowband terahertz radiation via phonon mode enhanced nonlinearities in a $BaGa_4Se_7$ crystal," *Optics Letters*, vol. 45, pp. 4722–4725, 2020.

57. Y. Yin, B. Wang, E. J. Yiwen, L. Yao, X. Wang, W. Bai, and W. Liu, "Raman spectra and phonon structures of $BaGa_4Se_7$ crystal," *Communications Physics*, vol. 3, p. 34, 2020.

58. E. Yiwen, J. Yao, and L. Wang, "Propagation of terahertz waves in a monoclinic crystal $BaGa_4Se_7$," *Scientific Reports*, vol. 8, p. 16229, 2018.

59. Y. Guo, Z. Li, Z. Lei, X. Luo, J. Yao, C. Yang, and Y. Wu, "Synthesis, growth of crack-free large-size $BaGa_4Se_7$ crystal, and annealing studies," *Crystal Growth and Design*, vol. 19, pp. 1282–1287, 2019.

60. N. Y. Kostyukova, A. A. Boyko, E. Y. Erushin, A. I. Kostyukov, V. V. Badikov, D. V. Badikov, and D. B. Kolker, "Laser-induced damage threshold of $BaGa_4Se_7$ and $BaGa_2GeSe_6$ nonlinear crystals at 1.053 μm," *Journal of the Optical Society of America B: Optical Physics*, vol. 36, pp. 2260–2265, 2019.

61. N. Y. Kostyukova, A. A. Boyko, I. D. Eranov, O. L. Antipov, D. B. Kolker, A. I. Kostyukov, E. Y. Erushin, I. B. Miroshnichenko, D. V. Badikov, and V. V. Badikov, "Laser-induced damage threshold of the nonlinear crystals $BaGa_4Se_7$

and $BaGa_2GeSe_6$ at 2091 μm in the nanosecond regime," *Journal of the Optical Society of America B: Optical Physics*, vol. 37, pp. 2655–2659, 2020.

62. J.-M. Spaeth and H. Overhof, *Point Defects in Semiconductors and Insulators: Determination of Atomic and Electronic Structure From Paramagnetic Hyperfine Interactions*. Spinger-Verlag, 2003.

63. D. Goldfarb and S. Stoll, Eds., *EPR Spectroscopy: Fundamentals and Methods*. John Wiley and Sons, Inc, 2018.

64. A. P. Yelisseyev, S. I. Lobanov, P. G. Krinitsin, and L. I. Isaenko, "The optical properties of the nonlinear crystal $BaGa_4Se_7$," *Optical Materials*, vol. 99, no. 109564, 2020.

65. P. G. Schunemann and K. T. Zawilski, "Horizontal gradient freeze growth of wide band gap mid-infrared nlo crystals $BaGa_4S_7$ and $BaGa_4Se_7$," in *Nonlinear Frequency Generation and Conversion: Materials and Devices XVII*, K. L. Vodopyanov and K. L. Schepler, Eds., vol. 10516, International Society for Optics and Photonics. SPIE, 2018.

66. R. D. Shannon, "Revised effective ionic radii and systematic studies of interatomic distances in halides and chalcogenides," *Acta Crystallographica Section A*, vol. 32, pp. 751–767, 1976.

67. N. J. Stone, "Table of nuclear magnetic dipole and electric quadrupole moments," *Atomic Data and Nuclear Data Tables*, vol. 90, pp. 75–176, 2005.

68. S. Stoll and A. Schweiger, "Easyspin, a comprehensive software package for spectral simulation and analysis in EPR," *Journal Magnetic Resonance*, vol. 178, pp. 42–55, 2006.

69. G. Breit and I. I. Rabi, "Measurement of nuclear spin," *Physical Review*, vol. 38, pp. 2082–2083, 1931.

70. I. I. Rabi, "On the process of space quantization," *Physical Review*, vol. 49, pp. 324–328, 1936.

71. J. A. Weil, "The analysis of large hyperfine splitting in paramagnetic resonance spectroscopy," *Journal of Magnetic Resonance*, vol. 4, pp. 394–399, 1971.

72. A. Räuber and J. Schneider, "Electron spin resonance of a photosensitive 2s1/2-state gallium center in zns," *Physical Review Letters*, vol. 16, pp. 1075–1076, 1966.

73. G. E. Holmberg, K. H. Lee, and J. H. Crawford, "EPR and optical studies of γ-irradiated MgO:Ga," *Physical Review B*, vol. 19, pp. 2436–2439, 1979.

74. S. V. Nistor, D. Schoemaker, and I. Ursu, "Spectroscopy of the ns^1-centers in ionic crystals," *Physica Status Solidi B*, vol. 185, pp. 9–75, 1994.

75. D. V. Azamat, A. Dejneka, J. Lancok, V. A. Trepakov, L. Jastrabik, and A. G. Badalyan, "Electron paramagnetic resonance studies of manganese centers in $SrTiO_3$: Non-Kramers Mn^{3+} ions and spin-spin coupled Mn^{4+} dimers," *Journal of Applied Physics*, vol. 111, no. 104119, 2012.

76. R. A. Serway, W. Berlinger, K. A. Müller, and R. W. Collins, "Electron paramagnetic resonance of three manganese centers in reduced $SrTiO_3$," *Physical Review B*, vol. 16, pp. 4761–4768, 1977.

77. H. J. Gerritsen and E. S. Sabisky, "Paramagnetic resonance of trivalent manganese in rutile (TiO_2)," *Physical Review*, vol. 132, pp. 1507–1512, 1963.

78. O. F. Schirmer, "O^- bound small polarons in oxide materials," *Journal of Physics Condensed Matter*, vol. 18, pp. R667–R704, 2006.

79. C. A. Lenyk, M. S. Holston, B. E. Kananen, L. E. Halliburton, and N. C. Giles, "Lithium and gallium vacancies in $LiGaO_2$ crystals," *Journal of Applied Physics*, vol. 124, no. 135702, 2018.

80. B. E. Kananen, L. E. Halliburton, K. T. Stevens, G. K. Foundos, and N. C. Giles, "Gallium vacancies in β-Ga_2O_2 crystals," *Applied Physics Letters*, vol. 110, no. 202104, 2017.

81. M. S. Holston, J. W. McClory, N. C. Giles, and L. E. Halliburton, "Radiation-induced defects in $LiAlO_2$ crystals: Holes trapped by lithium vacancies and their role in thermoluminescence," *Journal of Luminescence*, vol. 160, pp. 43–49, 2015.

82. M. W. Swinney, J. W. McClory, J. C. Petrosky, S. Yang, A. T. Brant, V. T. Adamiv, Y. V. Burak, P. A. Dowben, and L. E. Halliburton, "Identification of electron and hole traps in lithium tetraborate ($Li_2B_4O_7$) crystals: Oxygen vacancies and lithium vacancies," *Journal of Applied Physics*, vol. 107, no. 113715, 2010.

83. I. N. Ogorodnikov, A. V. Porotnikov, S. V. Kudyakov, A. V. Kruzhalov, and V. Y. Yakovlev, "Stable and metastable optical absorption of LiB_3O_5 nonlinear crystals," *Physics of the Solid State*, vol. 39, pp. 1366–1368, 1997.

84. I. Ogorodnikov, A. Kruzhalov, A. Porotnikov, and V. Y. Yakovlev, "Dynamics of electronic excitations and localized states in LiB_3O_5," *Journal of Luminescence*, vol. 76-77, pp. 464–466, 1998.

85. I. N. Ogorodnikov, A. V. Porotnikov, S. V. Kudyakov, A. V. Kruzhalov, and V. Y. Yakovlev, "Recombination kinetics in nonlinear defective LiB_3O_5 crystals," *Physics of the Solid State*, vol. 40, pp. 1817–1822, 1998.

86. I. Ogorodnikov, S. K. Maria, and V. Yakovlev, "A pulsed optical characterization of nonlinear lithium borate crystals," *Journal of the Optical Society of America B*, vol. 29, pp. 370–376, 2012.

87. I. N. Ogorodnikov, V. Y. Yakovlev, and L. I. Isaenko, "Transient optical absorption and luminescence of lithium triborate LiB_3O_5," *Physics of the Solid State*, vol. 45, pp. 845–853, 2003.

88. C. Röcker, P. Weinert, P. Villeval, D. Lupinski, M. Delaigue, C. Hönninger, R. Weber, T. Graf, and M. A. Ahmed, "Nonlinear absorption in lithium triborate frequency converters for high-power ultrafast lasers," *Optics Express*, vol. 30, no. 4, pp. 5423–5438, 2022.

89. C. Mühlig and B. Simon, "Characterization of nonlinear optical crystal absorption," *Optical Engineering*, vol. 57, pp. 1–6, 2018.

90. O. I. Vershinin, A. V. Konyashkin, and O. A. Ryabushkin, "Anisotropy of nonlinear optical absorption of LBO crystals at 355 nm," *Optics Letters*, vol. 43, pp. 58–61, 2018.

91. D. G. Nikitin, O. A. Byalkovskiy, O. I. Vershinin, P. V. Puyu, and V. A. Tyrtyshnyy, "Sum frequency generation of uv laser radiation at 266 nm in LBO crystal," *Optics Letters*, vol. 41, pp. 1660–1663, 2016.

92. M. Takahashi, G. Masada, I. Sekine, M. Cadatal, T. Shimizu, N. Sarukura, C. Byeon, V. Fedorov, S. Mirov, A. Dergachev, and P. F. Moulton, "Reduction of nonlinear absorption in $Li_2B_4O_7$ by controlling temperature and repetition rate," *Japanese Journal of Applied Physics*, vol. 48, no. 112502, 2009.

93. I. Nikolov, D. Perlov, S. Livneh, E. Sanchez, P. Czechowicz, V. Kondilenko, and D. Loiacono, "Growth and morphology of large LiB_3O_5 single crystals," *Journal of Crystal Growth*, vol. 331, pp. 1–3, 2011.

94. A. V. Porotnikov, I. N. Ogorodnikov, S. V. Kudyakov, A. V. Kruzhalov, and S. L. Votyakov, "EPR of hole centers in nonlinear $LiBO_3$ crystals," *Physics of the Solid State*, vol. 39, pp. 1224–1227, 1997.

95. N. Pylneva, N. Kononova, A. Yurkin, G. Bazarova, and V. Danilov, "Growth and non-linear optical properties of lithium triborate crystals," *Journal of Crystal Growth*, vol. 198-199, pp. 546–550, 1999.

96. H. Kima, J. Kang, S. Lee, and S. Chung, "Growth of lithium triborate crystals by the TSSG technique," *Journal of Crystal Growth*, vol. 187, pp. 455–462, 1998.

97. S. F. Radaev, B. A. Maximov, V. I. Simonov, B. V. Andreev, and V. A. D'yakov, "Deformation density in lithium triborate, LiB_3O_5," *Acta Crystallographica Section B*, vol. 48, pp. 154–160, 1992.

98. C. Le Hénaff, N. K. Hansen, J. Protas, and G. Marnier, "Electron Density Distribution in LiB_3O_5 at 293 K," *Acta Crystallographica Section B*, vol. 53, pp. 870–879, 1997.

99. Y. Shepelev, R. Bubnova, S. Filatov, N. Sennova, and N. Pilneva, "LiB_3O_5 crystal structure at 20, 227 and 377°c," *Journal of Solid State Chemistry*, vol. 178, pp. 2987–2997, 2005.

100. H. Goldstein, C. Poole, and J. Safko, *Classical Mechanics*, 3rd ed. Addison Wesley, 2002.

101. "Atomic parameters for paramagnetic resonance data," *Journal of Magnetic Resonance (1969)*, vol. 30, pp. 577–582, 1978.

102. B. E. Kananen, M. J. W., N. C. Giles, and L. E. Halliburton, "Copper-doped lithium triborate (LiB_3O_5) crystals: A photoluminescense, thermoluminescence, and electron paramagnetic resonance study," *Journal of Luminescence*, vol. 194, pp. 700–705, 2018.

103. R. W. Boyd, *Nonlinear Optics*, 4th ed. Academic Press, 2020.

104. P. N. Butcher and D. Cotter, *The Elements of Nonlinear Optics*. Cambridge University Press, 1990.

105. W. Shakespeare, *Romeo and Juliet*. Dover Publications, 1993.

106. R. Shankar, *Principles of Quantum Mechanics*, 2nd ed. Springer, 1994.

107. C. P. Poole and F. A. Horacio, *The Theory of Magnetic Resonance*. Wiley-Interscience, 1972.

108. S. Setzler, "Electron paramagnetic resonance studies of electron and hole traps related to optical damage in $KTiO(PO_4)$," Ph.D. dissertation, West Virginia University, 1998.

REPORT DOCUMENTATION PAGE

Form Approved
OMB No. 0704–0188

1. REPORT DATE *(DD–MM–YYYY)*	2. REPORT TYPE	3. DATES COVERED *(From — To)*
15–05–2022	Dissertation	Sept 2019 — May 2022

4. TITLE AND SUBTITLE

IDENTIFICATION AND CHARACTERIZATION OF POINT DEFECTS IN NONLINEAR OPTICAL CRYSTALS: BARIUM GALLIUM SELENIDE AND LITHIUM TRIBORATE

5a. CONTRACT NUMBER

5b. GRANT NUMBER

5c. PROGRAM ELEMENT NUMBER

6. AUTHOR(S)

Holloway, Brian C., Lieutenant Colonel, USA

5d. PROJECT NUMBER

5e. TASK NUMBER

5f. WORK UNIT NUMBER

7. PERFORMING ORGANIZATION NAME(S) AND ADDRESS(ES)

Air Force Institute of Technology
Graduate School of Engineering and Management (AFIT/EN)
2950 Hobson Way
WPAFB OH 45433-7765

8. PERFORMING ORGANIZATION REPORT NUMBER

AFIT/GAP/ENP/11-S01

9. SPONSORING / MONITORING AGENCY NAME(S) AND ADDRESS(ES)

Department of Engineering Physics
2950 Hobson Way
WPAFB OH 45433-7765
DSN 271-0690, COMM 937-255-3636
Email: christopher.lenyk@afit.edu

10. SPONSOR/MONITOR'S ACRONYM(S)

AFWA

11. SPONSOR/MONITOR'S REPORT NUMBER(S)

12. DISTRIBUTION / AVAILABILITY STATEMENT

DISTRIBUTION STATEMENT A:
APPROVED FOR PUBLIC RELEASE; DISTRIBUTION IS UNLIMITED.

13. SUPPLEMENTARY NOTES

14. ABSTRACT

Increased interest in developing new nonlinear optical materials has led to 3rd generation materials, such as $BaGa_4Se_7$ and LiB_3O_5. These two nonlinear optical crystals have the potential to enable development of tunable lasers operating across the mid-wave infrared and the ultraviolet regions, respectively. Coherent light sources are used in the development of enhanced technologies with commercial and defense-based applications such as: health and environmental monitoring devices, next-generation infrared countermeasures, and ballistic missile booster exhaust plume characterization. The performance of optical materials in high-powered military applications is largely limited by the presence of defects. These defects adversely affect performance through unwanted optical absorption, resulting in the buildup of excess heat, causing material deterioration or complete failure. High-sensitivity and high-resolution experimental techniques, such as electron paramagnetic resonance, enable identification and characterization of defects in materials. In partnership and cooperation with U.S. industrial crystal growth companies, this information is shared, improving material quality and performance.

15. SUBJECT TERMS

electron paramagnetic resonance, optical absorption, single crystals, point defects, barium gallium selenide, lithium triborate, selenium vacancies, oxygen vacancies

16. SECURITY CLASSIFICATION OF:			17. LIMITATION OF ABSTRACT	18. NUMBER OF PAGES	19a. NAME OF RESPONSIBLE PERSON
a. REPORT	b. ABSTRACT	c. THIS PAGE			Lt Col Christopher A. Lenyk (Ph.D.)
U	U	U	U	204	19b. TELEPHONE NUMBER *(include area code)* (937)255-3636,x4558; christopher.lenyk@afit.edu